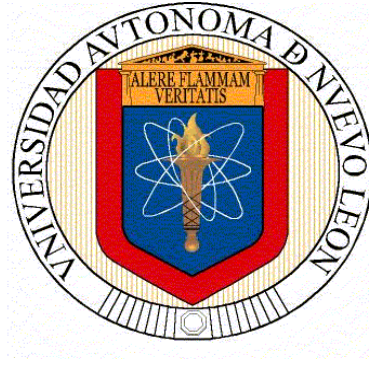


**UNIVERSIDAD AUTÓNOMA DE NUEVO LEÓN
FACULTAD DE INGENIERÍA MECÁNICA Y ELÉCTRICA**



TESIS

**A NOVEL EXPERIMENTAL METHOD TO CALCULATE
THE FRACTURE SURFACE ENERGY OF GEOTHERMAL
BEDROCKS IN REALISTIC TEMPERATURE CONDITIONS,
AS A CONTRIBUTION TO CLIMATE CHANGE MITIGATION**

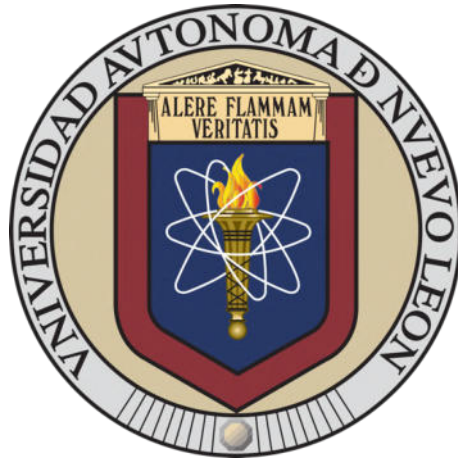
POR

OMAR RODRIGUEZ VILLARREAL

**COMO REQUISITO PARCIAL PARA OBTENER EL GRADO DE
DOCTORADO EN INGENIERÍA DE MATERIALES**

NOVIEMBRE 2023

UNIVERSIDAD AUTÓNOMA DE NUEVO LEÓN
FACULTAD DE INGENIERÍA MECÁNICA Y ELÉCTRICA



A Novel Experimental Method to Calculate the Fracture Surface Energy
of Geothermal Bedrocks in Realistic Temperature Conditions, As A
Contribution to Climate Change Mitigation

Presented by:
Omar Rodriguez Villarreal

To obtain the academic degree of Ph.D. in Materials Engineering

THÈSE
UNIVERSITE DE PAU ET DES PAYS DE L'ADOUR
UNIVERSIDAD AUTÓNOMA DE NUEVO LEÓN
École doctorale:

Sciences Exactes & leurs applications (ED211)

par
Omar Rodriguez Villarreal

Pour obtenir le grade de docteur
de l'Université de Pau et des Pays de l'Adour et Universidad Autónoma de Nuevo
León

Spécialité : Génie Civil et Ingénierie des Matériaux

**NEW EXPERIMENTAL METHOD FOR ESTIMATING
FRACTURE ENERGY FROM HYDRAULIC FRACTURING
TESTS IN MORTAR AND ROCK AT GEOTHERMAL
RESERVOIR TEMPERATURES.**

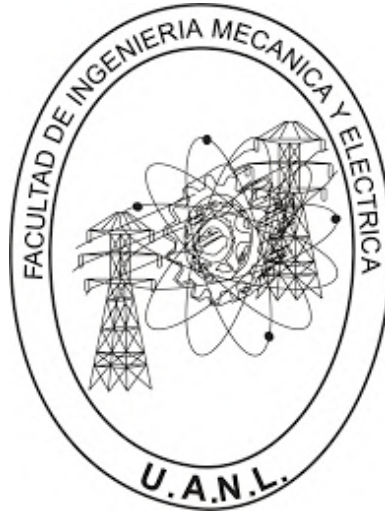
Soutenance prévue le 15 Décembre 2023 devant la Commission d'examen formée de:

MEMBRES DU JURY

Nicolas BURLION	Université de Lille	Rapporteur
Syed Yasir ALAM	Université de Nantes	Rapporteur
Ana Maria GUZMAN	Universidad Autónoma de Nuevo León	Rapporteur
Lauren GOMEZ	Universidad Autónoma de Nuevo León	Examineur
Christophe PETIT	Université de Limoges	Examineur
Jorge ALDACO	Universidad Autónoma de Nuevo León	Examineur
Gilles PIJAUDIER-CABOT	Université de Pau et des Pays de L'Adour	Directeur de thèse
Christian LA BORDERIE	Université de Pau et des Pays de L'Adour	Directeur de thèse
Moisés HINOJOSA	Universidad Autónoma de Nuevo León	Directeur de thèse



FACULTAD DE INGENIERÍA MECÁNICA Y ELÉCTRICA
SUBDIRECCION DE ESTUDIOS DE POSGRADO



A Novel Experimental Method to Calculate the Fracture Surface Energy
of Geothermal Bedrocks in Realistic Temperature Conditions, As A
Contribution to Climate Change Mitigation

Presented by:
Omar Rodriguez Villarreal

In option to the degree of:
Ph.D. in Materials Engineering

Monterrey, Nuevo León, México

November 2023

UNIVERSIDAD AUTÓNOMA DE NUEVO LEÓN
Facultad de Ingeniería Mecánica y Eléctrica
Posgrado

Los miembros del Comité de Evaluación de Tesis recomendamos que la Tesis "A novel experimental method to calculate the fracture surface energy of geothermal bedrocks in realistic temperature conditions, as a contribution to climate change mitigation", realizada por el estudiante Omar Rodríguez Villarreal, con número de matrícula 1352720, sea aceptada para su defensa como requisito parcial para obtener el grado de Doctor en Ingeniería de Materiales.

El Comité de Evaluación de Tesis

Dr. Moisés Hinojosa Rivera
Director

Dra. Ana Maria Guzmán Hernández
Revisor


Dr. Jorge Adrián Aldaco Castañeda
Revisor

Dra. Lauren Yolanda Gómez Zamorano
Revisor

Dr. Gilles Pijaudier-Cabot
Revisor

Dr. Christian La Borderie
Revisor

Vo.Bo.


Dr. Simon Martínez Martínez
Subdirector de Estudios de Posgrado

Institución 190001

Programa 1226 08

Acta Núm. 335

Ciudad Universitaria, a 22 de noviembre de 2023.

Declaración de autenticidad:

Declaro solemnemente que he preparado este documento siguiendo las mejores prácticas nacionales e internacionales. Contiene material original generado y redactado por mí. También contiene material parafraseado o entre-comillado, que por ser de otras personas se incluye dando el debido reconocimiento, citando las fuentes documentales correspondientes.

San Nicolás de los Garza abril de 2022

M.C. Omar Rodríguez Villarreal

La vie est une guerre

La vie est un combat

La vie est une lutte

María Félix

Abstract

Geothermal energy remains an underutilized form of renewable energy, with the optimization of geothermal reservoirs relying on hydraulic fracturing to enhance permeability. To effectively carry out hydraulic fracturing, a thorough understanding of the fracture energy of the bedrock is essential. While experimental methods exist to measure fracture energy, the literature highlights certain limitations that have not been adequately addressed. **An Enhanced Geothermal System (EGS)** can be thought of as an underground heat exchanger designed to extract geothermal energy. The performance of these systems can be improved by increasing its permeability by hydraulic fracturing, following the same technique used for hydrocarbon reservoirs. In order to understand hydraulic fracturing, whether it is implemented in an EGS or in a hydrocarbon reservoir, it is important to know the fracture parameters of the rock at stake, e.g. the fracture energy. In quasi-brittle materials such as rocks, concrete and mortar, fracture energy is usually measured by three-point bend tests, acoustic emission, and other techniques. We report here the use of an alternative method based on an energy balance during hydraulic fracture tests. A set of specimens of synthetic rocks made from mortar and limestone was prepared and they have been mechanically and hydromechanically characterized to determine their elastic properties, uniaxial tensile and compressive strength, and permeability. The fracture energy was obtained from a balance of kinetic, potential and pressure energies involved in the hydraulic fracture tests. Fracture energies for mortar and rocks at 20°C and 100°C are obtained in an analogic model of a laboratory-scale "EGS" created to emulate a real geothermal reservoir. The fracture energy estimate, applied to the present laboratory set-up, provides fracture energies of mortar at ambient temperature that are consistent with the literature data on similar materials, for example, on average, we obtained a fracture energy of 92.97 J/m² with a standard deviation of 4.03 J/m² for synthetic rocks. For natural rock we got on average 213.5 J/m² for the fracture energy. Temperature is found to have an influence on the fracture energy as it increases for both limestone and mortar of 20–30%. Then, using the same formulation, mortar specimens with three different diameters were manufactured and with a known method, such as the size effect or bending test, the fracture energy at room temperature was calculated again to corroborate the values obtained with the energy balance during hydraulic fracture. This original contribution in the field of fracture mechanics applied to geothermal reservoirs is based on laboratory tests and has potential application to real reservoirs; the proposed methods yield results validated by strict international scrutiny and constitute an additional tool to improve the permeability and, therefore, the extraction efficiency of geothermal energy, which is a green, renewable, and still scarcely exploited source in our country and the world. Therefore, the authors consider that contributions such as the present one, as modest as it may seem, will contribute to the mitigation of the already significant effects of climate change caused by human activity.

Keywords: Enhanced Geothermal Systems, Permeability, Hydraulic Fracture Test, Surface Fracture Energy, Energy balance, Mortar, Rocks.

Acknowledgements

First, I want to thank God, the Angels, and my family for having been a support and a driving force in my life and this project.

To the National Council of Science and Technology "CONACYT", Investissement d'Avenir French programme (ANR-16-IDEX-0002) and to the Association pour le Développement des Energies Renouvelables et Alternatives "ANDERA" and CAMPUS FRANCE México for having financed this project.

To the Universidad Autónoma de Nuevo León (UANL) and the Université de Pau et Pays de l'Adour (UPPA) for opening the doors during my doctoral training in the double degree modality.

To my thesis director in Mexico, to Dr. Moisés Hinojosa Rivera for his time, his valuable advice, moral and financial support during the completion of this thesis project. Also, to my Co-Director of thesis in Mexico, Dr. Alberto Varela Valdez, for his time and support at all times. To my Thesis Directors in France, Prof. Gilles Pijaudier-Cabot and Prof. Christian La Borderie, for their time, academic and financial support in this project. **¡Thanks a lot!**

To Guillermo Boccara and Sophie Leban from Campus France México, for their support of my doctoral project.

I also thank the research, technical and administrative staff of the Mexican Center for Innovation in Geothermal Energy (CeMIEGeo) in Ensenada, Mexico. Especially to Dr. Juan Manuel Romo Jones, Lic. Claudia Cárdenas, Lic. Belinda Sandoval, M.C Margarita Martínez, Dr. Rene Guzman, and M.C Omar Pérez Valdovinos.

Also, I would like to thank my colleagues from the Laboratoire des Fluides Complexes et leurs Réservoirs "LFCR" of the Institut Supérieur Aquitain du Bâtiment et des Travaux Publics "ISA-BTP in Anglet, France for their help during my 3 years stay in France. Specially to Amaia Matanza Corro, Olivier Nouailletas, Youssef Fawaz, Islam Lebouachera, Rafik Abdallah, Hui Wang, Victor Okumko, Mohammed Rachedi, Mohamed Said, Hafid Nouali and Caroline Hain. **¡Thanks for everything!**

Finally, to my boss, Prof. Olivier Deck, chief of the Department of Georesources and Civil Engineering at the École des Mines de Nancy of the University of Lorraine for giving me my first job opportunity in France. **¡Thanks a lot!**. Also, special thanks to my colleagues: Yamina Arnone, Prof. Rassol Mehdizadeh and Prof. Audrey Bonnelye.

Table of Contents

Abstract	2
Chapter I: Introduction	10
1.1 Generalities	10
1.2 Mitigation of climate change	11
1.3 Renewable energies	12
1.3.1 Geothermal energy.....	12
1.3.1.1 Enhanced geothermal systems (EGS).....	13
1.3.2 Geothermal energy in Mexico and France	14
1.3.3 Challenges and the future of geothermal energy	16
1.4 Potential areas for improve in an EGS	16
Chapter II: Literature review	19
2.1 Generalities	19
2.2 Hydraulic fracturing.....	19
2.3 Hydraulic fracture in geothermal energy	20
2.4 Mechanics of hydraulic fracture	23
2.5 Fluid notion inside the fracture.....	24
2.6 Fracture models	29
2.6.1 Generalities	29
2.6.2 Patterns and fracture mechanisms in rocks and other quasi-brittle materials.....	32
2.6.3 Griffith fracture toughness.....	33
2.6.4 Energy release rate and fracture energy.....	35
2.7 Obtention of fracture energy	38
2.7.1 Generalities	38
2.7.2 Traditional methods to obtain fracture energy.....	40
2.7.2.1 Uniaxial tensile test (UTT)	41
2.7.2.2 Three-point bending test (3PBT)	42
2.7.2.3 Four-point bending test (4PBT).....	44
2.7.2.4 Compact tension test (CTT).....	45
2.7.2.5 Wedge splitting test (WST)	46
2.7.2.6 Size effect method	47
2.7.3 Comparison between different methods to obtain the fracture energy.....	48
2.7.4 Effect of temperature on the fracture energy.....	49
2.8 Stresses intensity factor	52
2.8.1 Dynamic fracture	55
2.8.2 Crack growth based on energy balance	56
2.8.3 Graphical representation of energy balance equation	58
2.8.4 Basic load-displacement relationship	59
2.9 Numerical finite simulations and compliance method	60
2.9.1 Spatial and temporal discretization of boundary value problems	61
2.9.2 Energy Principles of continuum Mechanics	63
2.9.3 Variation of Displacement Field	64
Contribution.....	65
Star point.....	67
General objective	67
Objectives	67
References	69

Chapter III: Methodology	4
3.0 Generalities	76
3.1 Study area	77
3.2 Summary of methodology	78
3.3 Preparation of synthetic and natural rock samples	80
3.4 Open porosity and drying of rocks and synthetic rock samples	81
3.5 Mechanical characterization of rocks and synthetic rock samples.....	81
3.6 Hydro-mechanical characterization of rocks and synthetic rock samples.....	82
3.6.1 Permeability test at room and high temperature.....	83
3.6.2 Hydraulic fracture test at room and at high temperature	84
3.7 Verification of the method for estimating the fracture energy	88
3.7.1 Mortar sample for bending test.....	88
3.7.2 Cutting of mortar samples	90
3.7.3 Three-point bending test.....	91
3.7.4 Obtaining the Young's modulus of new mortar samples	93
3.7.5 Finite element	94
3.7.5.1 Estimation of fracture energy	96
References	103
Appendix	104
Chapter IV: Result and Discussion	111
4.1 Porosity test	111
4.2 Mechanical characterization	111
4.3 Permeability test.....	113
4.4 Hydraulic fracture test	118
4.4.1 Synthetic rock and natural rocks.....	118
4.5 Verification of the method for estimating fracture energy	125
4.5.1 Three-point bending test in synthetic rock	132
4.5.1.1 Determination of fracture energy in mortar samples from 2021 with size effect.....	132
4.5.1.2 Determination of fracture energy in mortar samples from 2022 with size effect.....	133
4.6 Determination of fracture energy with numerical simulation.....	137
References	141
Chapter V: Conclusions and Perspectives	143
5.1 Conclusions.....	143
5.2 Perspectives	145
5.3 Contributions	146

Index of figures

Figure	Title	Page
1	Diagram of a geothermal energy.....	12
2	Basic layout of an “EGS” type geothermal plant purposes for being used.....	13
3	Heat flow and geothermal resources in México.....	14
4	Heat flow and geothermal resources in Europe.....	15
5	Horizontal section of a vertical wellbore under the action of in situ stresses and borehole pressure.....	21
6	A down-hole pressure record. Mechanics of hydraulic Fracturing.....	22
7	Hydraulic fracture in 3D.....	24
8	Conservation of flow in a control volume.....	26
9	Boundary of the flow domain.....	27
10	Fracture mechanics structure.....	30
11	Load modes that promote crack advance.....	32
12	Image obtained by backscattered electrons (BE) from a concrete surface	32
13	Fracture pattern "mirror", "mist" and "hackle" in a tensile glass specimen.....	33
14	a) Semi-infinite plate with the central cavity of length two a (double crack tip), subjected to tension, b) half plate with a single crack of length a, subjected to tension.....	34
15	a) Plate with fixed ends, b) Energy reduction by crack extension.....	36
16	a) Plate with free ends subjected to uniform tension, b) Plate with free ends subjected to load, c) Energy reduction by crack extension.	37
17	(a) In true LEFM, crack growth must take place under constant \mathcal{G} . (b) A loading- cracking-unloading process in a LEFM specimen.....	39
18	P-u plot of a loading-cracking-unloading in LEFM: (a) For a typical structure where iso-5 curves display downwards slope; (b) for more exotic structures or loadings the slope of the iso-5 curves may be positive.....	40
19	Direct uniaxial tension.....	41
20	Bending test – three points.....	43
21	Four point bending test (4PBT).....	44
22	Compact tension test (CTT).....	45
23	Wedge splitting test (WST).....	47
24	Stress field near the crack tip.....	53
25	Load-displacement response of a cracked plate for propagation of a crack from length a_1 to a_2 under "fixed grips" conditions along AB	58
26	Potential energy	60
27	Finite element discretization: a tension strap.....	62
28	Detailed view of a finite element, b) transition conditions to the neighboring element..	62
29	Location of the collection area of rocks representative of a geothermal reservoir.....	77
30	Area of the collection of rocks representative of a geothermal reservoir.....	77
31	Analog model of an “EGS” at the laboratory scale.....	79
32	Stratigraphic profile of the study area.....	79
33	Rock collection and obtaining cores.....	80
34	Preparation of synthetic rock specimens.....	80
35	Drying and open porosity test on synthetic and limestone specimens.....	81
36	Mechanical characterization of synthetic rocks.....	81
37	Mechanical characterization of rocks.....	82
38	Cross-section of a typical test specimen.....	82
39	Injection system for permeability tests.....	83
40	Hydro-mechanical characterization of the synthetic rock specimens.....	83
41	Hydro-mechanical characterization of rock representative in geothermal reservoir.....	84

42	Hydraulic fracture test system for specimens.....	85
43	Methods used to obtain fracture energy.....	88
44	Preparation of mortar specimens.....	89
45	Mortar specimens cut in half circle and with notch.....	90
46	Sensors to measure displacement during the test.....	91
47	Machine ZWICK 250.....	92
48	Mortar sample of 20 cm of diameter.....	92
49	Mortar sample of 10 cm of diameter.....	92
50	Mortar sample of 5 cm of diameter.....	93
51	Mortar specimen during the test to calculate the modulus of young.....	84
52	Choosing the cracking zone.....	96
53	Principle for calculating work between A and B.....	97
54	Process method.....	98
55	Complacency curve.....	99
56	Complacency experimental of the mortar sample.....	100
57	Relative displacement.....	101
58	Fracture energy average over the central zone.....	102
59	Evolution of injected fluid flow rate in mortar sample 14.....	114
60	Permeability testing on some mortar and rock samples.....	115
61	Permeability test at room temperature of mortar samples.....	116
62	Permeability test at high temperature of mortar samples.....	116
63	Permeability test at room temperature of rock samples.....	117
64	Permeability test at high temperature of rock samples.....	117
65	Comparison of pore pressure evolution in mortar and rock samples.....	118
66	Mortar samples after hydraulic fracture test at room temperature.....	119
67	Set-up for high temperature tests in limestone samples.	121
68	Hydraulic fracture test in mortar samples at room temperature.....	122
69	Hydraulic fracture test in mortar samples at high temperature.....	122
70	Hydraulic test at room temperature of rock samples.....	123
71	Hydraulic test at high temperatures of rock samples.....	123
72	Fracture energy values of mortar samples	124
73	Fracture energy values of rock samples.....	124
74	Mortar samples of 2.5 cm of diameter from 2021.....	126
75	Mortar samples of 5.2 cm of diameter from 2021.....	126
76	Mortar samples of 10.20 cm of diameter from 2021.....	127
77	Mortar samples of 20 cm of diameter from 2022.....	127
78	Mortar samples of 10.20 cm of diameter from 2022.....	127
79	Mortar samples of 5.20 cm of diameter from 2022.....	128
80	Determination of the slope and intercept of the regression line for mortar samples.....	132
81	Size effect law for mortar samples from 2021.....	133
82	Determination of the slope and intercept of the regression line for mortar samples.....	133
83	Size effect law for mortar samples from 2022.....	134
84	Size effect law for 4 mortar samples.....	135
85	Last fracture energy for sample of 10.20 cm of diameter	137
86	Last fracture energy for sample of 5.20 cm of diameter.....	137
87	Last fracture energy for sample of 20 cm of diameter.....	138
88	Last fracture energy for sample of 10.20 cm of diameter.....	138
89	Last fracture energy for sample of 5.20 cm of diameter.....	138
90	Determination of real fracture energy.....	139

List of Tables

Table	Title	Page
1	Conceptual table about fractures processes.....	30
2	Mortar mixes.....	89
3	Dimensions in mortar specimens.....	91
4	Results in mechanical characterization for mortar samples.....	111
5	Estimation of elastic properties and fracture properties for rocks samples.....	112
6	Estimation of fracture toughness for rocks samples.....	112
7	Permeability test in mortar samples	113
8	Permeability test in rock samples.....	113
9	Permeability coefficient of the mortar and rocks specimens.....	114
10	Fracture energy values of specimens reported in figure 62.....	120
11	Fracture energy values at room temperature in mortar specimens.....	120
12	Summary of results obtained from limestone rock specimens.....	122
13	Results of the bending test for mortar samples from 2021.....	125
14	Results of the bending test for mortar samples from 2022.....	125
15	Calculations of mortar samples from 2021.....	132
16	Calculations of mortar samples from 2021.....	132
17	Parameters obtained.....	132
18	Obtaining fracture energy.....	132
19	Calculations of mortar samples from 2022.....	133
20	Calculations of mortar samples from 2022.....	134
21	Parameters obtained.....	134
22	Obtaining fracture energy.....	134
23	Fracture toughness for mortar samples from 2022.....	136
24	Fracture toughness for mortar samples from 2022.....	136
25	Fracture energy average values obtained by several methods.....	140

Symbology

G_f	Fracture energy
E	Modulus of elasticity
ϕ	Open porosity
ν	Poisson ratio
σ_t	Tensile strength
κ	Coefficient of permeability
σ_c	Maximum compressive strength
E_{K1}	Kinetic energy
E_{z1}	Potential energy
E_{p1}	Pressure energy
P_{atm}	Atmospheric pressure
E_{μ}	The Energy dissipated by viscosity
C	Constant
D_o	Diameter outside
D_I	Diameter inside
AE	Acoustic emission

CHAPTER I INTRODUCTION

1. Introduction

1.1 Generalities

Fracture mechanics in geotechnical engineering is a discipline that focuses on the study of fracture propagation. Fracture mechanics in geotechnical engineering plays a crucial role in mitigating and adapting to the effects of climate change as research and applications in this field can help develop sustainable solutions and address current challenges related to climate change. According with the Paris agreement, one way to mitigate the effects of climate change is to reduce greenhouse gas emissions; because we are generating a lot of electricity, transportation, heating buildings, and many materials, like steel and cement causing a lot of pollution. In September 2021, the Intergovernmental Panel on Climate Change (IPCC) released its new report which states that climate change is generalized, rapid and intense. Therefore, we need to change our economy to green energy and to have new scientific contributions. One of the objectives is to present geothermal energy as a solution to the new global challenges caused by climate change, as it is a little known and studied energy. These challenges are complicated and finding a viable solution requires the participation of many disciplines. However, in each area there are difficulties that require advances or new knowledge to find solutions and apply them appropriately, as they are necessary to guarantee our sustainable future. Fracture mechanics applied to a geothermal reservoir can help us describe the mechanisms and patterns that are generated during the fracture process in rocks, that is, the propagation of cracks, as well as the distribution of stresses and deformations that occur in a cracked or discontinuous material.

There are a few broad themes on which climate scientists may agree regarding the anticipated size of the effects of climate change. For instance, a rise in average sea level; an increase in average global temperatures; modifications to precipitation patterns and amounts; ocean acidification; and an increase in the frequency, density, and intensity of extreme events like hurricanes, floods, and droughts, among other things. Water supplies, infrastructure, the food supply, ecosystems, and ultimately human health and wellbeing will all be impacted by these effects. All these changes will result in several geotechnical difficulties, such as the requirement for fresh approaches to safeguard coastal towns against sea level rise and the effects of the melting of the north and south poles. Existing dams will also be under danger if weather disasters like droughts and floods become more frequent. As was already established, the United Nations lists two alternatives for addressing climate change: mitigating it by lowering greenhouse gas emissions and adapting to its effects. Future research in the subject of geology, such as geotechnics and rock fracture mechanics, will be heavily influenced by the transition to a low-carbon economy, which will necessitate significant modifications in the infrastructure of energy distribution networks [35-37].

Soon, with the advent of new energy resources, such as geothermal energy, it will be necessary to manage these resources by optimizing the use of energy for rational and efficient use management of these resources, which will consist of the optimization in the use of energy, looking for a rational and efficient use. Therefore, through energy management it is possible to detect opportunities for improvement in aspects related to the quality and safety of the energy system, achieving high levels of energy efficiency. For instance, the global energy demand is currently projected to increase by about 30% during the following 25 years, according to estimates [38].

1.2 Mitigation of climate change

Research, innovation, or development of fundamental geotechnical engineering knowledge, including fracture mechanics, can solve some of today's most significant societal problems, e.g., climate change, urban sustainability, and resilience, energy, and water resource management. Experts have called these problems the global challenges of the "new world" whose solutions require geotechnical solutions. These challenges are broad and complex, so identifying viable application solutions for each will require many disciplines, for example, fracture mechanics. This is strongly related to geotechnical engineering [37]. In the Anthropocene epoch [1], the human activities speed up the process of climate change, mainly with the generation of greenhouse gases emissions that generate many problems on the environment, due to future greenhouse gas emissions. Some scenarios that may occur in this century are a rise in sea level of about two meters (6.6 feet), while the temperature may increase by up to 4°C (39°F). However, although the magnitude of the effects or consequences of climate change is unknown, there are several general hypotheses. There will also be new engineering and geotechnical challenges, for example, the need for new strategies to protect coastal cities against rising sea levels and increased intensity of meteorological phenomena, which will endanger dams and dikes and lead to excessive erosion and local scour [2-5]. According to the United Nations Framework Convention on Climate Change (UNFCCC), some options to deal with climate change include reducing greenhouse gas emissions, adapting to its effects, and enhancing greenhouse gas sinks [7]. The main types of renewable energy are hydroelectric, solar, wind and geothermal. However, there is a need for research in development and innovation on all types of renewable energy and the best strategies to mitigate climate change through the Paris Agreement [8]. China is the world's largest energy consumer, with energy consumption expected to increase by 60% by 2030 [9]. One way to mitigate climate change is through the 2015 Paris Agreement developed by the United Nations (UN), which aims to control long-term temperature increases by regulating greenhouse gas production. The objectives of the agreement will only be met if developed countries move towards low-carbon economies by investing in energy efficiency technologies, renewable energy resources, and methods to reduce the effects associated with the current use of fossil fuels, such as carbon capture and storage. Currently, renewable energy sources such as geothermal, solar, hydroelectric, and wind are only used to generate electricity for residential use.

Fuels derived from fossil fuels are used for transportation and industrial processes (especially in the production of building materials like Portland cement), which contribute substantially to greenhouse gas emissions. [33]. A significant shift to a low-carbon economy in the world will require major changes in the supporting infrastructure of the energy distribution and transportation systems. Among other things, research in geology will be driven by a low-carbon economy, such as wind energy, hydropower, carbon capture and storage, and geothermal energy. As a basis for designing and understanding stimulated reservoirs for enhanced geothermal systems, which are sometimes referred to as universal heat mining, this research project focuses on the characterization of fracture systems produced by hydraulic fracturing (permeability enhancement) [34-35].

1.3 Renewable energies

In the world of energy, renewable energies are considered clean, inexhaustible, and more competitive than ever before. They possess distinct characteristics that set them apart from fossil fuels, such as their diversity, abundance, and potential for utilization across any region of the globe. However, their most significant advantage lies in the fact that they do not emit greenhouse gases, which are known to contribute to climate change. Renewable energies are mainly divided into solar, wind, hydro, geothermal, biomass and ocean energy.

1.3.1 Geothermal energy

An Earth's geothermal system uses heat from the Earth's interior, which is transmitted through hot rock bodies, conduction, and convection processes, where groundwater and rock interact, producing renewable energy (See figure 1). The deep layers are at high temperatures, and often at that depth there are water tables (upper surface of the zone of saturation) where water is heated: as it rises, the hot water or steam produces manifestations on the surface, such as geysers or hot springs, used for bathing since ancient times [10-11].

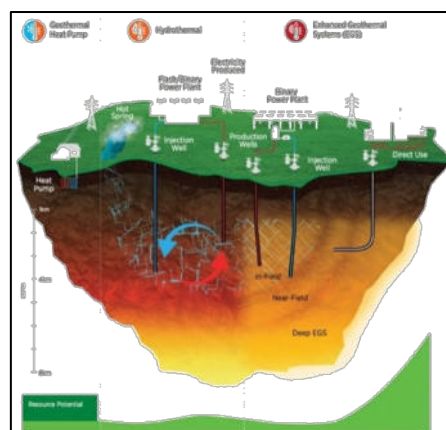


Figure 1. Diagram of a geothermal energy [11].

Types of geothermal reservoirs, there are three types of geothermal reservoirs, which could be called:

- Hot water
- Dry
- Geysers

In 2010, the United States had a worldwide geothermal electricity production of 3,086 MW through 77 power plants [12]. In addition, the country with the highest geothermal potential in the world is Indonesia. It is estimated to have the largest geothermal reserves and resources, with a potential capacity of over 28,000 megawatts (MW). Other countries with significant geothermal potential include the United States, Philippines, Mexico, Italy, and Turkey [13-15].

1.3.1.1 Enhanced geothermal systems (EGS)

EGS (Enhanced Geothermal Systems) concept, originated in the United States. The patent filed in 1974 for an "EGS" describes the formation of an all-natural reservoir designed to obtain geothermal energy. This reservoir consists of a block of hot rock located 4 to 5 km below the earth's surface [16].

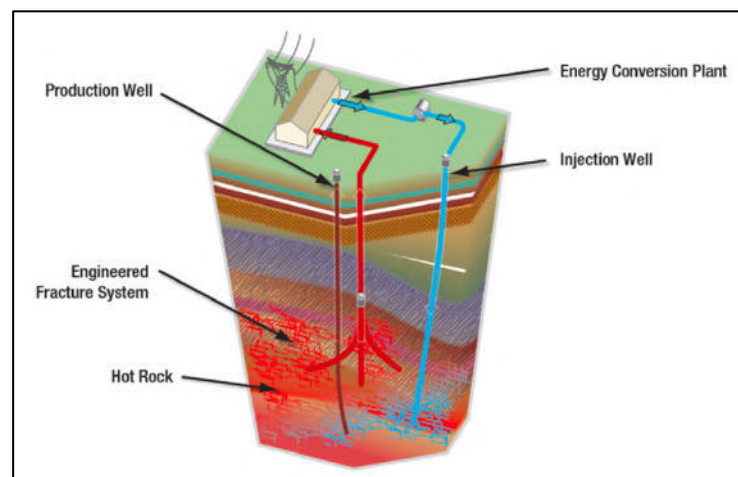


Figure 2. Basic layout of an “EGS” type geothermal plant purposes for being used [17].

Enhanced geothermal systems (EGS) actively pump and heat water by injecting it into wells. High pressure water is injected into the rock to cause it to expand, crack open, and allow water to flow freely in and out. The method was modified from methods for extracting oil and gas (See Figure 2). There is less chance of environmental harm because the geological formations are deeper and harmful chemicals are not used. To increase the reservoir's size, drillers can utilize directional drilling [18].

Less than 1% of the world's energy comes from geothermal sources, and it is only used to generate power and district heating from high-grade hydrothermal resources (fluids that are above 200 °C). Understanding hydraulic fracturing in a "EGS" or a hydrocarbon reservoir requires knowledge of the fracturing parameters of the target rock, such as fracture energy [19]. An "EGS" is a subway heat exchanger designed to extract geothermal energy, and its performance can be improved by increasing its permeability through hydraulic fracturing [19].

1.3.2 Geothermal energy in Mexico and France

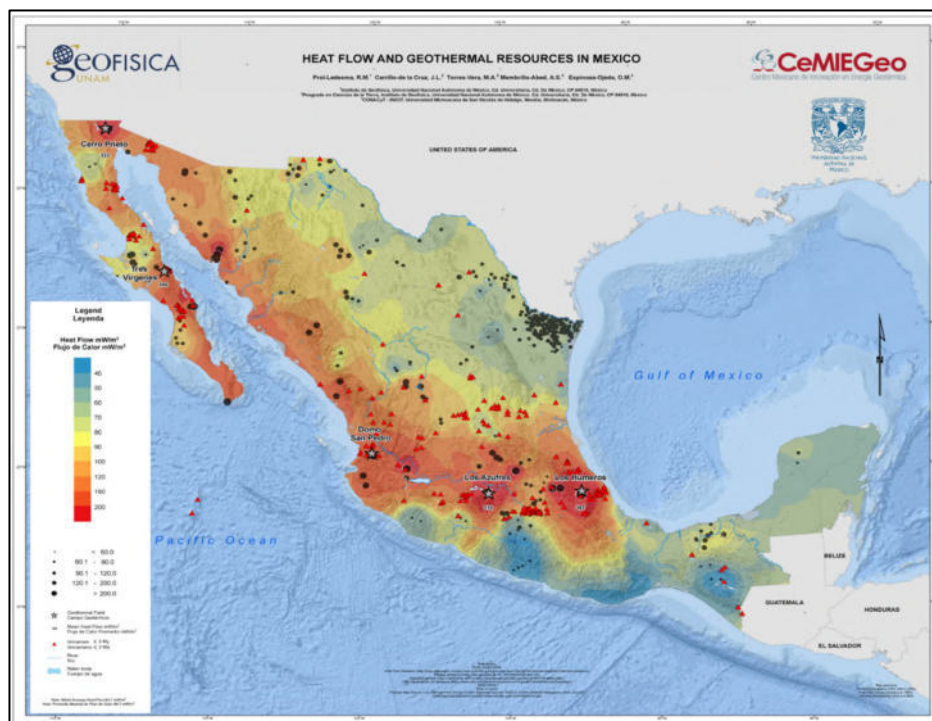


Figure 3. Heat flow and geothermal resources in México [20].

Mexico is the fourth country in the world with the highest geothermal energy production, with an installed capacity of 1005,8 megawatts (MW) that contribute 7 % of all geothermal energy production worldwide [21]. Figure 3 shows heat flux values that show that a large part of Mexico contains promising areas for direct exploitation and geothermal energy utilization. The average heat flux for the continents is 64.7 mW/m² [21], and much of Mexico presents heat flux values above 100 mW/m². This suggests that Mexico's geothermal potential has not yet been exhausted and that exploration in new areas and new research could be pursued to take advantage of this green energy to increase its development sustainably [20]. Cerro Prieto, Los Azufres, Los Hornos, Las Tres Virgenes, and Domo de San Pedro are the five geothermal fields that produce most

of the installed capacity in Mexico. With 570 MWe in operation, Cerro Prieto continues to be the largest field in Mexico and the second largest in the world [23]. In Mexico in 2018, 18.9% of the electricity produced came from renewable sources (hydro, wind, geothermal, solar, and biofuels). The percentage of power produced in Mexico using green energy sources in 2018 was 23.2%, falling short of the 35% mark set by the Energy Transition Law for the country by the year 2024 [24-25]. Just 12% more geothermal energy is expected to be produced in 2025 than there will be in December 2019 [26]. In México, geothermal resources have been little exploited, being used mainly in bathing and swimming facilities for recreational purposes, despite the great thermal potential identified at the surface [27]. With this reference, in this project, a temperature of 100° C was used at high-temperature tests and to estimate the permeability coefficient and fracture energy. On the island of Guadalupe in France, the first geothermal drilling-based power plants were built. France aims to play a significant role in the energy transition following the One Planet conference in 2017 and the 2015 climate pact. France produces a variety of renewable energy sources, including hydropower (61%), wind energy (23.8%), and photovoltaic energy (8.1%). Less than 1% of all renewable energy is produced using deep geothermal energy [28]. In addition, after the 1980 oil crisis, using low-temperature geothermal energy became an affordable choice. The "calorific" potential of geothermal energy was the primary driver of its growth in continental France; thirty low-energy geothermal power plants were constructed in France between 1980 and 1985. Numerous initiatives have been started since 2000 because of the Ministry of Mines issued twelve permits for high-temperature geothermal energy research in southwest France [29]. The geothermal resources of Europe are depicted in Figure 4.

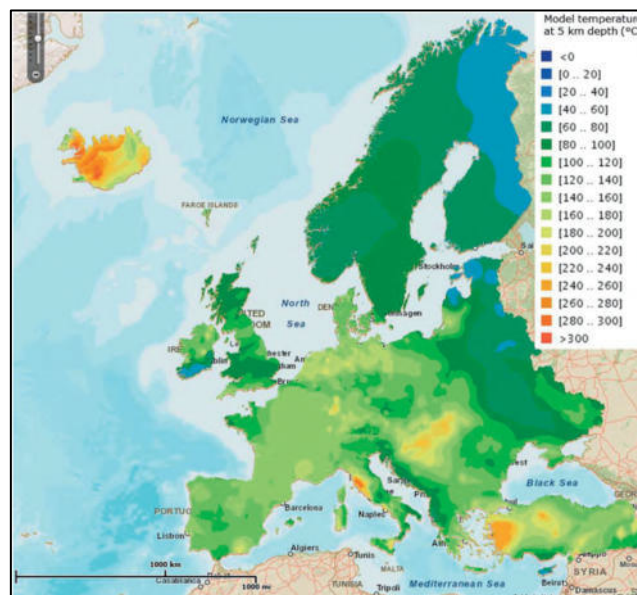


Figure 4. Heat flow and geothermal resources in Europe [30].

1.3.3 Challenges and the future of geothermal energy

According to the Massachusetts Institute of Technology (MIT) research "The Future of Geothermal Energy," Enhanced Geothermal Systems, or "EGS," are the method of using geothermal energy in the future since the temperatures are high enough to produce electricity (130-200°C). Fracture networks are built or enlarged in an "EGS" to operate as additional paths for the fluid (water) and as a heat exchanger. The extracted heat is subsequently used for district heating and/or the production of electricity. Some ideas for increasing access to and recovering deep heat in a "EGS" include the following: (a) stimulating and investigating low permeability reservoirs and expanding the extent of geothermal fields through permeability stimulation, (b) improving thermodynamic cycles to ensure energy production from medium temperature (80°C and above) water resources, (c) improving exploration techniques for deep geothermal resources, and (d) improving drilling, reservoir evaluation and stimulation technology "EGS" systems, which have been improved, have demonstrated considerable promise. The future of geothermal energy will rely on how quickly new investments and the development of geothermal power plants can go because EGS is still in the "proof of concept" stage [31–32].

1.4 Potential areas for improvement in an EGS

Numerous studies have shown the technical feasibility of Enhanced Geothermal Systems (EGS), substantiating the existence of a readily accessible resource base. Furthermore, it has been established that achieving optimal outcomes necessitates the augmentation of permeability. The present study has directed its attention on this area of investigation. The hydraulic fracturing method governs the regulation of four key characteristics, namely flow rate, short circuit, connection between wells, and generated seismicity. Enhancing the quantity of conductive cracks existing between wells would result in heightened fluid flow and mitigate the occurrence of short circuits. Enhancing comprehension of the fracturing process would enhance endeavors aimed at ensuring the interconnection between two wells and mitigating the impacts of generated seismicity. There are two potential processes for hydraulic fracturing. Hydraulic fracturing involves the creation of a novel fracture that initiates and extends in a direction away from the wellbore. In the presence of preexisting fractures, which may have been sealed by hydrothermal changes, the occurrence of slip is facilitated when the fluid pressure rises, leading to a reduction in the frictional resistance of the fractures to shear. There are two primary criteria that govern the stimulation of shear in preexisting fractures: (1) the characteristics of the preexisting fracture network and (2) the mechanism via which hydraulic stimulation propagates through the network and enhances conductivity [39]. In contrast to the hydrothermal system, the Enhanced Geothermal System "EGS" has the capacity to extract a greater amount of heat via the use of artificial cracks.

The primary procedures involved in the construction are as follows: (1) the examination of hot dry rock; (2) the assessment of fracture distribution; (3) the establishment of an injection and production well; (4) the utilization of hydraulic fracturing technology to extract geothermal energy from a reservoir [40–43]. A tool for the study of EGS is the numerical simulation due to its low cost [44], where several parameters must be considered, for example: temperature, but the simulation approaches, such as numerical and analytical models, have shown their use and efficacy in examining various processes within the geothermal system [45,46]. Numerical approaches have been used to investigate the impacts of crucial elements in an Enhanced Geothermal System (EGS), including subsurface water flow, reservoir characteristics, and heat exchanger architecture [47-51]. Moreover, many analytical models, including the helical line source model [52], annular coil source model [53], and cylindrical heat source model [54], among others, have been extensively used for the purpose of optimizing and designing heat exchangers. There are two techniques that may be used to depict the fracture system: the discrete fracture network model and the equivalent continuous porous media model [55–57]. For a numerical model for fracture networks in an any reservoir. At now, there exist two prevailing theories about induced fractures in the petroleum, gas, and geothermal sectors: the traditional fracture theory, which relies on linear elastic mechanics, and the volume fracturing approach. According to the standard fracture theory, it is believed that the rock is a homogenous medium [58]. The occurrence of an induced fracture is attributed to the tensile failure of a crack, which is oriented perpendicular to the minimal horizontal stress present in the natural rock formation [59-60]. Nevertheless, the theory just considers the physical size and the direction of hydraulic fracture caused by fractures. Despite the existence of many expansions to this approach within the framework of this theory, accurately characterizing the extent and geometry of the hydraulic fracture remains challenging. In contrast, the volume-fracturing theory diverges from the underlying premise of traditional fracture theory.

The Volume Fracturing theory is defined in two distinct manners according to sources. In a general sense, the term "Volume Fracturing technique" encompasses both the separate-layer fracturing technique, which aims to enhance the productivity of vertical wells in reservoirs, and the horizontal well staged fracturing technique, which aims to improve reservoir seepage and drainage capabilities. In a more specific context, the fracturing procedures employed to create fracture networks in reservoirs, known as fracturing measures, might be referred to as the Volume Fracturing methodology. The application of the Volume Fracturing theory enables the fragmentation of reservoirs, the generation of fractures within intricate fracture networks, and the subsequent establishment of artificial permeability. The fracture initiation model employed in Volume Fracturing technique challenges the conventional classical model by include not only the initiation and extension of individual open fractures, but also the initiation and extension of a complex fracture network [153].

There are two conventional fracture theories that characterize the primary fracture, based on varying assumptions on the direction and height of fracture extension. The PKN (Perkins–Kern–Nordgren) model was developed by a group of researchers consisting of Perkin, Kerns, and Nordgren. At present, the PKN model is extensively used as a hydraulic fracture model in the context of oil and gas reservoirs [61]. The PKN model, sometimes known as the blade-shaped or finger-like model, assumes a significant disparity between the fracture length and height. The calculation of fracture width in this model involves the use of a plane strain elasticity equation and a viscous fluid flow equation. An additional model that might be considered is the KGD (Khristianovic–Geertsma–De Klerk) model, which was first proposed by Khristianovich and Zheltov in 1955 [62-63]. The underlying assumption of this model is that the height of the fracture is equivalent to the height of the reservoir. The flow of fracturing fluid was seen only in the direction of the fracture length, assuming a one-dimensional scenario. The use of viscous flow theory was applied in this model to establish a connection between the mathematical representation of fracture extension. In other case for a numerical model of hydraulic fracturing, the theory regarding fracture development and fluid flow encompasses a range of numerical simulation solution techniques that are used to solve the nonlinear partial differential equations associated with this phenomenon. These approaches include the finite element method (FEM), discrete element method (DEM), and the boundary element method (BEM) [64-65]. The techniques used in oil or gas reservoirs may be applied to hot dry rock reservoirs to strengthen the geothermal system. The numerical simulation approach may also be used to address analogous nonlinear partial differential problems in improved geothermal systems.

CHAPTER 2

LITERATURE REVIEW

2.1 Generalities

Geothermal energy remains an underutilized form of renewable energy, with the optimization of geothermal reservoirs relying on hydraulic fracturing to enhance permeability. To effectively carry out hydraulic fracturing, a thorough understanding of the fracture energy of the bedrock is essential. Traditional experimental methods do exist to measure fracture energy, but the available literature highlights certain limitations that have yet to be fully addressed. One glaring gap in the current knowledge is the absence of a reliable method to measure fracture energy in situ, within the actual geothermal reservoirs. This limitation poses a significant challenge in the development and operation of geothermal energy projects, as accurate data on fracture energy is crucial for optimizing geothermal reservoirs.

Hence, this project embarks on a quest to address this gap by exploring an alternative approach. The proposed method hinges on an energy balance concept during hydraulic fracturing tests to calculate the fracture energy. This approach employs an analogous model of a laboratory-scale geothermal system to simulate real-world conditions. This choice is especially relevant since enhanced geothermal systems (EGS) are akin to a kind of subterranean heat exchanger designed to harness geothermal energy. EGS operates by increasing the permeability of the subsurface through hydraulic fracturing, making it an ideal analog for our research. In addition to this innovative approach, this chapter provides valuable insights into the background and context of the research, offering readers a comprehensive understanding of the motivations and objectives of the thesis.

2.2 Hydraulic fracturing

The process of rock fracturing has emerged as a crucial concern within the fields of geomechanics and hydrocarbon production. Hydraulic fracturing has gained significant traction as a technique for enhancing the extraction of gas, oil, and geothermal energy. This method involves creating fractures in rocks to facilitate the circulation of fluids, thereby promoting efficient heat exchange, and enabling the flow of gas or oil. For example, to increase the permeability of the formation and, consequently, the flow of fluids from the reservoir towards a production well or from an injection well to the reservoir, a fracturing fluid is injected into a low permeable material to create fractures (flow channels). The expansion and extension of the fracture network is made possible by the injection of this fluid, which also increases the reservoir's permeability. The impact of enhanced fluid drainage diminishes over time quickly without proppant injection. This occurs because of the fractures healing and the well virtually reaching its initial state [66].

The use of Linear Elastic Fracture Mechanics (LEFM) has been utilized to examine the initiation and propagation of fractures in a range of solid mechanics [67-68] and rock mechanics scenarios [69,70,71]. The fundamental fracture propagation concept in Linear Elastic Fracture Mechanics (LEFM) posits that fracture propagation occurs when the stress intensity factor surpasses the fracture toughness, which represents the material's resistance to fracture. In the context of numerical simulation of hydraulic fracturing, the commonly employed approach is to assume a constant rock fracture toughness. This parameter is often determined by normal unconfined laboratory measurements [72-73]. Nevertheless, it has been demonstrated in published experimental findings that the fracture toughness is dependent on the level of confining stress [74-77]. Furthermore, it is worth noting that the presence of a fluid lag zone, which refers to the area behind the fracture tip that remains unpenetrated by the fracturing fluid, has been consistently found in many hydraulic fracturing experiments [78-79] as well as mine-back studies [80]. Therefore, it is imperative to incorporate the influence of fluid lag and confining stress into the calculation of fracture toughness to obtain precise estimations of the stress conditions near the fracture tip, fracture net pressure, and hydraulic fracture geometries.

2.3 Hydraulic fracture in geothermal energy

In the oil and gas industry, hydraulic fracturing has proven effective in creating fracture networks in deposits with limited permeability [81]. This is also true in the geothermal energy sector. A geothermal system is an underground heat exchanger, and surfaces where heat is exchanged with a circulating fluid should be as large as possible. This is the purpose of enhancement procedures based on hydraulic fracturing, yielding to an Enhanced Geothermal System (EGS). Furthermore, geothermal energy is a renewable source of energy that can be found in abundance on our planet, especially in Mexico and France, which are on the list of the 15 countries with the greatest geothermal capacity for electricity generation. Due to the great potential that exists in geothermal energy as green energy, estimates have been made of how much energy could be available on the planet. With 1% of this energy, it would be possible to meet the energy needs of the planet for 2800 years [1]. But to achieve a better optimization in an Enhanced Geothermal System (EGS), maximizing the surfaces where heat is exchanged means that the hydraulic fracturing process should be controlled as much as possible. Ideally, the induced fractures should be numerous, diffuse and well connected to each other. Obviously, such a goal is difficult to achieve as rock properties, in situ stresses, heterogeneities can neither be controlled nor changed, but a prerequisite for a better control, e.g. for hydraulic fracturing with multiple stages, is the knowledge of the fracture parameters of the rocks at stake in this process [10]. Hydraulic fracturing is used to enhance oil, gas, and geothermal energy production and the way to study this process on the wellbore. During the process, fracturing fluid is pumped into a selected wellbore section at high pressure. One or more cracks that extend into the rock medium are produced by this fluid pressure.

The minimal in situ compressive stress is often in the horizontal direction because fracturing takes place at considerable depths, whereas the hydraulically produced fracture is vertical. For a particular pumping rate and time, a forecast of the size (width, length, and height of the aperture) of the hydraulically induced fracture may be made using the reservoir rock parameters, the fracturing fluid, the magnitude, and the direction of in-situ stresses. For this, fracture models have been created. For example, a horizontal open hole without a casing can be considered under the action of in situ horizontal stresses (σ_{min} y σ_{max}) as shown in Figure 5. We can assume that the rock is an elastic medium and has a tensile failure stress σ_T . Applying the elasticity hypothesis, one may determine the breakdown pressure p_b for creating a crack at the borehole's surface to arrive at the following results [82]:

$$P_b = 3\sigma_{min} - \sigma_{max} + \sigma_T \tag{1}$$

Where σ_{min} is the minimum in situ stress, σ_{max} the maximum in situ stress, and σ_T the tensile failure stress of the rock. Figure 5 illustrates a hydraulically induced fracture as a vertical fracture with the fracture plane parallel to the minimum horizontal in situ stress (σ_{min}).

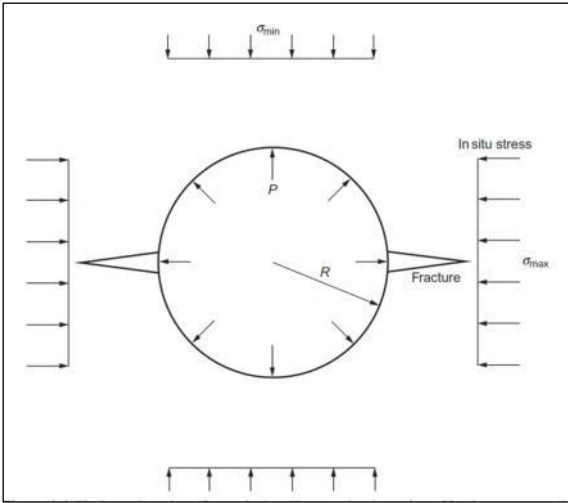


Figure 5. Horizontal section of a vertical wellbore under the action of in situ stresses and borehole pressure. Mechanics of hydraulic Fracturing (p.1-1), for Ching H. Yew and Xiaowei Weng, 2015, Oxford, UK. Elsevier, Second edition.

According to Equation 1, the borehole burst pressure is mostly used to relieve the compressive circumferential hoop stress caused by in situ stresses, with little or no influence from the rock rupture stress σ_T . In a wellbore, for instance, the applied pressure balances the reservoir pressure (pore pressure) before it surpasses the compressive circumferential hoop stress and creates tensile stress at the wellbore surface.

When this surface tension approaches the tensile stress of the rock medium, a fracture is therefore started. An illustration may be when, while pumping proceeds, a hydraulically induced crack spreads from the wellbore into the reservoir. Figure 6 shows an example of a typical downhole pressure log, the pressure measured inside the wellbore near the opening of the hydraulic fracture. A typical pressure log in cylindrical rock and mortar specimens, like the one presented in figure 6, will be shown later in the Results chapter.

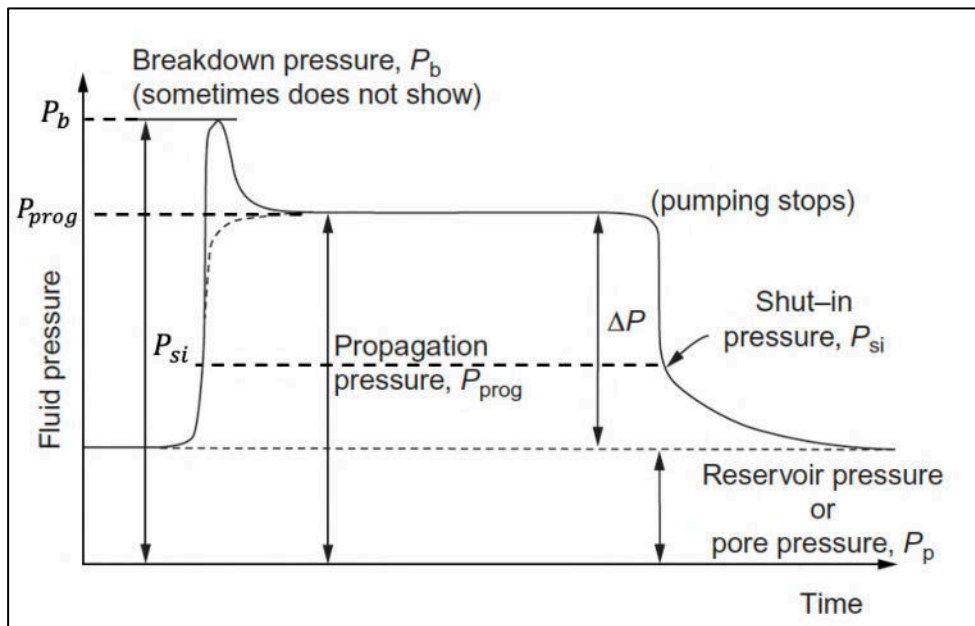


Figure 6. A down-hole pressure record. Mechanics of Hydraulic Fracturing (p.1-2), for Ching H. Yew and Xiaowei Weng, 2015, Oxford, UK. Elsevier, Second edition

As the pumping process proceeds, the hydraulically generated fracture spreads into the reservoir. The fracture opening is maintained by the net pressure (fluid pressure minus minimum in-situ stress), and the rate of fluid leak-off from the fracture surface. Fracturing fluid also simultaneously escapes from the fracture surface into the rock medium. The maximum pressure in figure 6 is the first burst pressure, or p_b . For instance, when a fracture starts at the wellbore's surface, the pressure decreases. The propagation pressure, or p_{prog} , is the almost constant portion of the pressure curve and is what causes the hydraulic fracture to spread throughout the reservoir.

Following an abrupt reduction in pressure caused by the disappearance of frictional pressure loss in the tubing, borehole entrance, and vicinity of the wellbore, the pressure gradually decreases to reservoir pressure because of fluid leakage from the fracture and wellbore, as depicted in Figure 6. The transition stage, also known as the closure pressure p_{si} (or instantaneous closure pressure, or "ISIP"), is a crucial part of the process. The fracture opening's width is thinning even though fluid is still dripping from the fracture surface.

The hydraulic fracture entirely closes when the fluid pressure inside the crack reaches equilibrium with the lowest in-situ stress. The hydraulic fracture closure pressure, which serves as a gauge for the minimum in situ stress, can be calculated by pressure drop analysis. The observed pressure-time curve makes it simple to identify the ISIP because it is a little higher than the hydraulic fracture closure pressure [83]. The fluid escapes from the fracture by flowing into the reservoir because of the pressure differential between the fracture and the reservoir. Porosity and pore fluid have been proven by experimental studies by Haimson and Fairhurst [84–85] and Medlin and Masse [86] to affect wellbore breakdown pressure.

2.4 Mechanics of hydraulic fracture

Hydraulic fracturing has been implemented for enhancing hydrocarbon production for more than 60 years. It is the subject today of a fast-growing scientific literature. The parameters to consider in the design of the hydraulic fracture process for hydrocarbon production are:

1. Young's modulus: could be related to the fracture width and the possibility of obtaining highly conductive fractures.
2. Critical stress intensity factor (or fracture energy): is the apparent resistance of the fracture, where it dominates the pressure required to propagate the fracture.
3. Fluid loss: related to the permeability of the formation and filtering characteristics of the fracture fluid.
4. Fluid viscosity: affects the net pressure in the fracture, fluid loss and transport.
5. Pump outflow: this can affect almost the entire process.

The values of all these parameters dominate the fracture process. Since the material is assumed to be isotropic, homogenous, and linearly elastic while the fracture fluid and fracture height are only ideal, the fracture energy calculation is essentially an approximation. The goal of a hydraulic fracture is to create the best possible fracture that will allow for the creation of high conductivity channels [87–89]:

1. As the length of fracture increases, accumulated production will increase, and revenues will also increase.
2. The number of resources produced by the foot reduces when the fracture lengthens relative to the length of an additional shored fracture.
3. The length of the fracture lengthens as treatment volume rises.
4. As the length of the fracture increases, the cost increases for each foot of fracture increases (cost/foot length of the shored fracture).

2.5 Fluid motion inside the fracture

The first three-dimensional (3D) fracture model, TerraFrac, was created by Clifton and Abou-Sayed and to include fluids, thermal effects, and formation with various elastic moduli [84-85]. Numerous authors have also used it to support other fracture models. For instance, a fluid can be thought of as flowing inside a very wide channel with a very narrow entrance in a hydraulic fracture. Half of a hydraulic fracture in a vertical well is visible because to the symmetrical distribution of in situ stress on the y-axis, as seen in figure 5 (See figure 7).

Next, a fluid that is Newtonian and incompressible and the assumption of a Newtonian fluid simplifies the formulation and gives a clear physical understanding of the flow phenomenon, even though the code adopted a non-Newtonian power-law fluid. For instance, the fracture opening is small, the fluid pressure fluctuation along the fracture width (in the z-direction) is minimal, and the velocity component's x-y plane derivatives with respect to Z are significantly bigger than the other derivatives. The Navier-Stokes equation for fluid motion can therefore be expressed as follows, neglecting inertia and body force:

$$\frac{\partial p}{\partial x} = \mu \frac{\partial}{\partial z} \left(\frac{\partial v_x}{\partial z} \right) \quad (2)$$

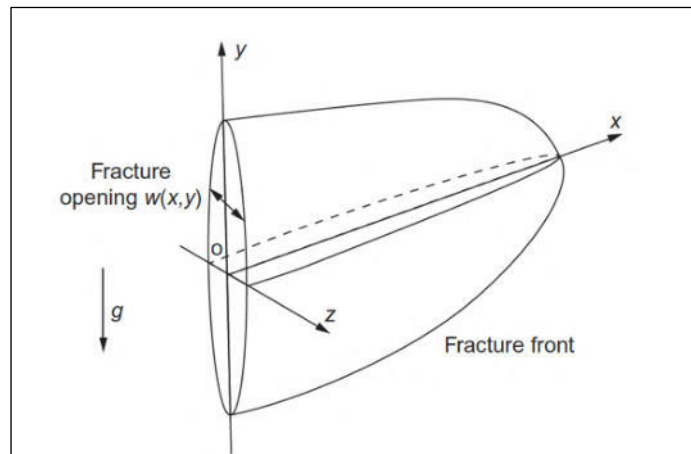


Figure 7. Hydraulic fracture in 3D. Mechanics of hydraulic Fracturing (p.2-1), for Ching H. Yew and Xiaowei Weng, 2015, Oxford, UK. Elsevier, Second edition.

$$\frac{\partial p}{\partial x} = \mu \frac{\partial}{\partial z} \left(\frac{\partial v_x}{\partial z} \right) \quad (3)$$

Now, knowing that there are no slip conditions on the fracture surfaces, we can now integrate the equations twice with respect to Z and obtain:

$$V_x = 0, \text{ at } z = \pm w/2 \quad (4)$$

$$V_y = 0, \text{ at } z = \pm \frac{w}{2} \quad (5)$$

The velocity profile along the fracture width can be represented as follows where w is the width of the fracture opening:

$$V_x = -\frac{1}{2\mu} \left[\left(\frac{w}{2}\right)^2 - z^2 \right] \frac{\partial p}{\partial x} \quad (6)$$

$$V_y = -\frac{1}{2\mu} \left[\left(\frac{w}{2}\right)^2 - z^2 \right] \frac{\partial p}{\partial x} \quad (7)$$

Then, consequently, the flow volume per unit fracture length is expressed as

$$\vec{q} = \int_{-\frac{w}{2}}^{\frac{w}{2}} \vec{v} dz \quad (8)$$

As seen in Figure 8, if we take a control volume with sides Dx and Dy , conservation of flow results in the equation.

$$-\frac{\partial q_x}{\partial x} - \frac{\partial q_y}{\partial y} - q_1 = \frac{\partial w}{\partial t} \quad (9)$$

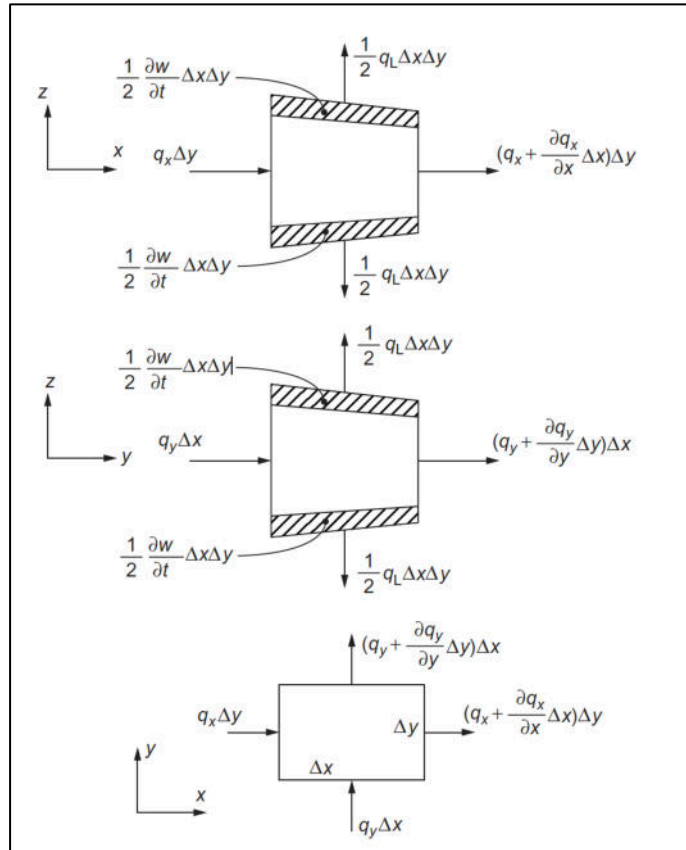


Figure 8. Representation of the conservation of flow in a control volume. Mechanics of hydraulic Fracturing (p.2-2), for Ching H. Yew and Xiaowei Weng, 2015, Oxford, UK. Elsevier, Second edition.

The term $\frac{\partial w}{\partial t}$ is the rate of volume increase and the term in the above equation.

$$q_1 = \frac{2C_1}{\sqrt{t-\tau(x,y)}} \tag{10}$$

And is the rate of fluid leakoff across fracture surfaces. In Equation 10, the constant $c\ell$ is an empirical fluid leakage coefficient, and $\tau(x, y)$ is the time fluid leakage begins at the fracture surface's location (x, y) .

$$\frac{\partial}{\partial x} \left(\frac{w^3 \partial p}{12\mu \partial x} \right) + \frac{\partial}{\partial y} \left(\frac{w^3 \partial p}{12\mu \partial y} \right) = \frac{\partial w}{\partial t} + \frac{2C_l}{\sqrt{t-\tau(x,y)}} \quad (11)$$

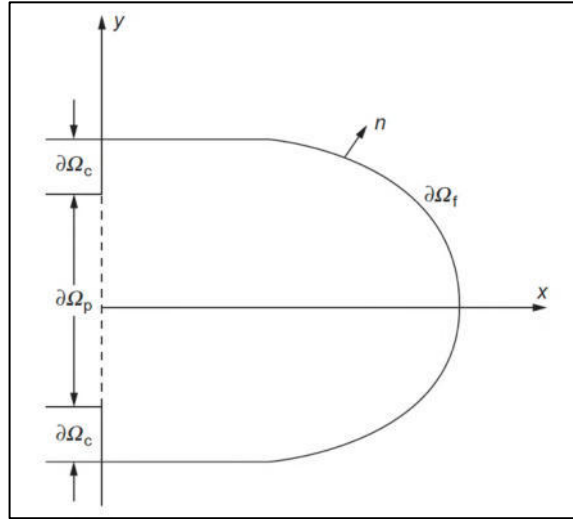


Figure 9. Boundary of the flow domain. Mechanics of hydraulic Fracturing (p.2-3), for Ching H. Yew and Xiaowei Weng, 2015, Oxford, UK. Elsevier, Second edition.

According to Figure 9, the boundary condition for the above equation can be written as follows:

1. Fracturing fluid is poured into the fracture through section $\partial\Omega_p$ (the fracture entrance); therefore:

$$-\frac{w^3}{12\mu} \left(\frac{\partial p}{\partial n} \right) = Q \quad (12)$$

If the micro fractures of the drilled wells have been linked, Q is the pumping rate per unit length in the inlet section, and n is the normal outward vector of the fracture line, as indicated.

2. The section $\partial\Omega_c$ is an axis of symmetry and the condition is.

$$-\frac{w^3}{12\mu} \left(\frac{\partial p}{\partial n} \right) = 0 \quad (13)$$

3. The section $\partial\Omega_f$ is the fracture front and the condition is.

$$-\frac{w^3}{12\mu} \left(\frac{\partial p}{\partial n} \right) = 0 \quad (14)$$

The border location and shape are unknown at the outset. Nevertheless. Applying the Galerkin finite element method, the flow equation is discretized [87]. The fluid pressure distribution in the domain can be approximated if O is the x - y flow field.

$$p(x, y) = \sum_{i=1}^N \Phi_{i(x,y)} p_i \quad (15)$$

The problem's basis function and finite element mesh creation, as well as the geometry of the fracture surface, will be covered in the following section. Adding the basis function ϕ_i to both sides of equation 13 and integrating across the domain O . After some algebraic adjustments, equation 13 becomes the following matrix equations.

$$[K]\{p\} = -\{f_L\} - \{f_w\} + \{f_p\} \quad (16)$$

Where:

$$K_{ij} = \int_{\Omega} \frac{w^3}{12\mu} \left(\frac{\partial \phi_i}{\partial x} \frac{\partial \phi_j}{\partial x} + \frac{\partial \phi_i}{\partial y} \frac{\partial \phi_j}{\partial y} \right) dx dy \quad (17)$$

$$f_{Li} = \int_{\Omega} \frac{2cl}{\sqrt{t-\tau}} \phi_i dx dy \quad (18)$$

$$f_{wi} = \int_{\Omega} \frac{\partial w}{\partial t} \phi_i dx dy \quad (19)$$

$$f_{pi} = \int_{\partial\Omega p} \phi_i ds \quad (20)$$

The conservation of global flow rate is a requirement for equation 13 to have a singular solution. This predicate can be expressed as:

$$-\int_{\Omega} q_L dx dy - \int_{\Omega} \frac{\partial w}{\partial t} dx dy + \int_{\partial\Omega p} Q ds = 0 \quad (21)$$

The above equation's discrete form is:

$$-\sum_i f_{Li} - \sum_i f_{wi} + \sum_i f_{pi} = 0 \quad (22)$$

The usage of the equation to calculate the time increment in the fracture growth calculation will be demonstrated later. In conclusion, equation 16, the equation of motion, equations 12 and 13 for the boundary conditions, and equation 22 for the constraint condition all govern the flow of fracturing fluid within a fracture. The equation also involves two unknowns: w and p . The fracture opening equation is therefore required to finish the problem.

2.6 Fracture models

2.6.1 Generalities

The study of rock fracture has emerged as a crucial area of focus within the field of geomechanics. This is particularly evident in industries such as hydrocarbon production and geothermal energy extraction, where the promotion of efficient heat exchange through fluid circulation in fractured rock formations is imperative. The application of fracture mechanics to geomaterials, including concrete and rock, has been extensively studied. As a result, various linear and nonlinear fracture theories have been developed. These theories either explicitly describe the crack or are based on continuum theories, such as those derived from damage mechanics. The utilization of fracture mechanics in rock engineering has been enhanced by the adoption of computational tools from other engineering disciplines, such as geo-thermal energy. This has led to the development of diverse computational algorithms that are capable of modeling tensile fracture in a rock mass [90].

Fracture is the separation of a solid into two parts, usually because of applying loads. The components that govern the fracture are the initiation of the crack and its propagation, the type of material in which the fracture occurs, the type of loading, the temperature of the material, the size of the sample, etc. Moreover, the fracture could be considered ductile or fragile. The fracture process always occurs in a tiny area around the tip of the crack, regardless of the size of the structure that fails during the fracture. Major stresses are present in this area, which is known as the Fracture Process Zone (FPZ) (See figure 10). Depending on the type of material, there are many dissipative processes that range from the formation of dislocations in crystalline materials, the creation of a network of micro-cracks in quasi-fragile materials, to the disentangling of molecular chains in polymers [91].

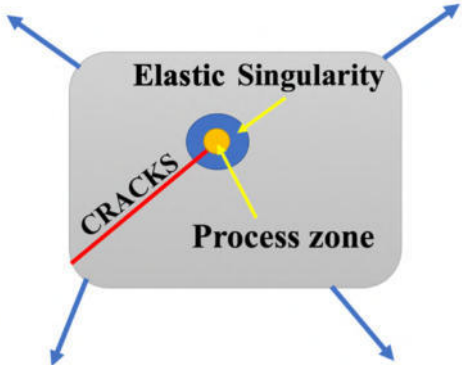


Figure 10. Fracture mechanics structure. The crack is surrounded by a region that is not physically known.

The categorization of structural materials into three groups, namely brittle, quasi-brittle, and elastic plastic, is based on the shape and dimensions of the fracture process zone (FPZ) that forms before the occurrence of fracture at the crack tip [91]. Concrete is classified as a quasi-brittle material. Cracking is a prevalent concern in this material, as the presence of microcracks occurs prior to the application of load due to the moisture loss in the concrete.

Table 1. Summarizes the fracture processes focused on the deformation properties of the materials:

Deformation behavior of material			
Elastic	Plastic	Viscoelastic/Viscoplastic	
Linear-elastic fracture mechanics	Elastic-plastic fracture mechanics	Creep fracture mechanics	
Failure behavior of material			
Brittle	Ductile	Creep	
Cleavage fracture rupture	Simple fracture/Shear fracture	Creep-fracture normal	
Type of loading			
Static	Dynamic	Cyclic	Chemical
Forced rupture	Fast fracture	Fatigue fracture	Stress and fatigue corrosion cracking
Crack behavior			
Stable		Unstable	
Subcritical crack growth local failure		Critical crack growth global failure	

Cracks in concrete are generated and extended under various circumstances, necessitating the application of fracture mechanics as the sole approach to enhance comprehension of crack development and expansion. The qualities of concrete, such as admixtures (such as pozzolanas and fibers), curing conditions, porosity, manufacturing method, water to cement ratio, and maximum aggregate size, contribute to its unique characteristics. As a result, the duration and magnitude of load necessary for crack propagation will vary. This phenomenon has resulted in the development of several computational fracture models, such as the Griffith model, fictitious crack model, crack band model, J-integral, smeared crack model, size effect model, two-parameter fracture model, cohesive crack band model, and Dugdale models. These models can be studied using experimental, numerical, and finite element methods [92]. These methods address the characteristics of fracture shape and propagation path, the way cracks extend, stress transfer mechanisms, and other related factors. One of the most valuable parameters that can be derived from these models includes the stress intensity factor (K), crack mouth opening displacement (CMOD), crack-tip opening displacement (CTOD), and the size-independent fracture energy (G_f), which holds significant importance in this study. In the field of fracture mechanics, it is commonly considered that the energy needed to propagate a crack is derived from the energy produced by the system during the process of crack propagation [93].

The phrase 'fracture mechanics' pertains to the relationship between the tensile strength of a material or structure and the critical defect size of the material under specific stress conditions [91]. When crack reaches its critical level, it initiates the process of propagation. The phenomenon of crack propagation can be classified into three distinct groups, sometimes referred to as the three modes of fracture. There are three modes of fracture propagation: Mode I, Mode II, and Mode III (see figure 11). In Mode I, the crack planes split apart. In Mode II, the crack planes glide over one other in a shear motion. In Mode III, the crack planes move against each other parallel to the crack plane, resulting in tearing and an example is shown in figure 15 because the study of the geological aspects of fracturing is significant due to the crucial role fractures play.

Therefore, the three types of fracture mode are:

- Fracture Mode I – The Opening mode (There is tensional stress parallel to the crack).
- Fracture Mode II - Shear Mode (Tangential forces act parallel to the faces in the crack but in opposite directions).
- Fracture Mode III - Rip mode (Tangential forces acting parallel, but perpendicular to the face of the plate and opposite each other).

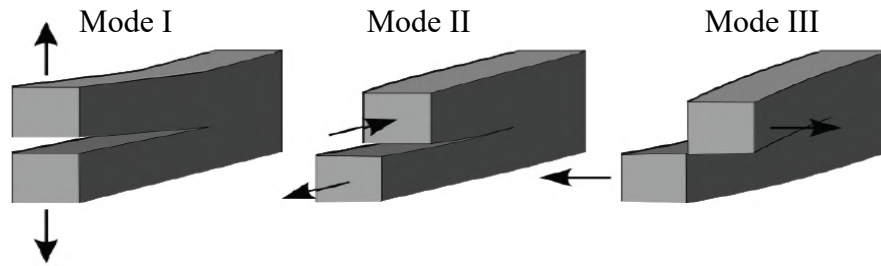


Figure 11. Load modes that promote crack advance. The left shows the aperture mode or I mode, which is the most common.

2.6.2 Patterns and fracture mechanisms in rocks and other quasi-brittle materials

Rocks can fracture in a ductile or brittle manner; ductile materials, for instance, readily deform under pressure and are easily stretched. Because brittle materials do not deform prior to breaking, they frequently fracture neatly and break instead of stretching, making them easy to reassemble. The test temperature, the rate at which the load is applied, the containment pressure, etc. all affect how ductile or brittle the material behaves. Even in their pristine, undistressed state, quasi-brittle materials have pores and microcracks. However, under low tensile loads, their impact on the material's mechanical response is not perceptible; as a result, the material is linear elastic [94]. At the microstructure level, rocks and concrete are heterogeneous, anisotropic, and porous materials, strongly influenced by pre-existing micro-cracking, deformation, pressure and temperature gradients, scale factor and cyclic loads (See figure 12). Then rupture is quasi-brittle in uniaxial compression and triaxial compression tests at low confinement pressures.

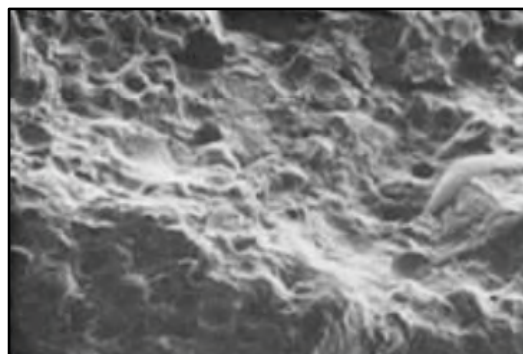


Figure 12. Image obtained by backscattered electrons (BE) from a concrete surface with non-interconnected voids [95].

Another tool used to study the fracture phenomena is the fractography of the fracture surface. An example of a typical fractographic morphology is the mirror, mist, and hackle patterns. Figure 13 shows this type of pattern on an inorganic glass fracture surface.

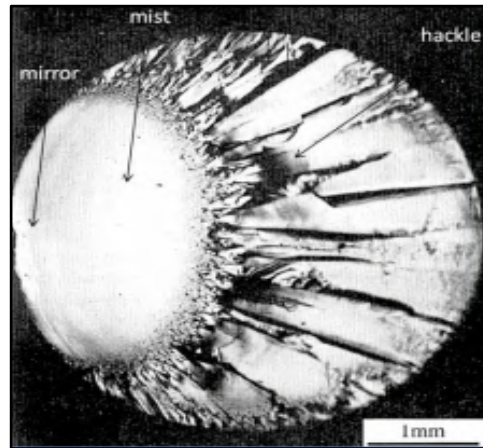


Figure 13. Fracture pattern "mirror", "mist" and "hackle" in a tensile glass specimen [96].

The following phenomena are identified in this type of fracture patterns:

1. Appearance changes in the fracture surface are associated with increased surface roughness.
2. The transitions from mirror to mist and from mist to hackle are not aligned, the phenomenon is related to progressive surface roughness changes.
3. Changes in roughness are sequential and are associated with changing the length of cracks.

2.6.3 Griffith fracture toughness

In fracture mechanics, it is possible to determine if a crack that already exists in a material used in a particular structure will be stable or whether it will spread because of stress. Two methods exist for forecasting this phenomenon: the one uses the concept of energy balance, while the second uses the concept of the stress field. This energy-based crack propagation criterion was developed by Griffith in 1921 because of his solution to the elastic issue of stresses at the vertex of an ellipsoidal cavity in a semi-infinite media [97]. It serves as the foundation for fracture mechanics [97]. To analyze Griffith's formulation, we consider a homogeneous and isotropic bar, of elastic modulus E , with a central crack of the elliptical shape of length $2a$, which is elastically deformed by tensile stresses σ as shown in Figure 14.

In this case, from Inglis' solution [98], Griffith found that the elastic energy (U) stored in the plate per unit thickness is:

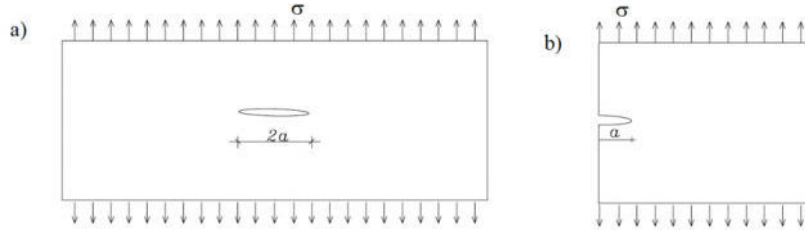


Figure 14. a) Semi-infinite plate with the central cavity of length two a (double crack tip), subjected to tension, b) half plate with a single crack of length a, subjected to tension.

$$U = \frac{\pi\sigma^2 a^2}{E} \quad (23)$$

And he defined surface energy (W) as:

$$W = 4a\gamma_s \quad (24)$$

Where $4a$ represents the size of the cracking surface and γ_s is the specific energy. When the crack lengthens, it enters a state of instability under the applied loads, and the mechanical system transfers energy from the non-fractured zone to the fracture by a process of converting elastic energy into surface energy. This process is mathematically represented as:

$$\frac{dU}{da} = \frac{dW}{da} \quad (25)$$

Using the energy balance, $\frac{dU}{da}$ means a reduction in the elastic energy stored by the plate due to the crack extension, then, derived equation 1 and 2 concerning the crack length is obtained:

$$\frac{dU}{da} = \frac{2\pi r^2 a}{E} \quad (26)$$

$$\frac{dW}{da} = 4\gamma_s \quad (27)$$

Replacing Equations 26 and 27 in Equation 25, the stress, which corresponds even to stress at which crack extension is initiated and is known as Griffith's fracture stress (σ_c), can be derived

$$\sigma_c = \sqrt{\frac{2\gamma_s E}{\pi a}} \quad (28)$$

When there is only one crack, only half of the plate is considered; therefore, equations 26 and 27 are as follows:

$$\frac{dU}{da} = \frac{\pi\sigma^2 a}{E} \quad (29)$$

$$\frac{dW}{da} = 2\gamma_s \quad (30)$$

The fracture stress of equation 28 is not affected due to the symmetry of the plate; it is the same to analyze the whole plate or half of it.

2.6.4 Rate of energy release and energy of fracture

Griffith's crack extension criterion can be broadly described as a balance between energy that is currently accessible and energy that is needed for the extension of the fracture. According to Griffith, the energy available for crack expansion is known as the energy release rate (G), and it is equal to dU/da , hence equation 29 can be written as:

$$\frac{dU}{da} = \frac{\pi\sigma^2 a}{E} = G \quad (31)$$

The critical energy release rate (G_{IC}), often referred to as the needed energy (dW/da), it has dimensions of force per unit fracture extension, which is why it is also known as crack resistant force (R). The G_{IC} condition occurs when the tensile stress σ acquires a critical value σ_c , for which $du/da = dW/da$ and therefore, from equation 31:

$$\frac{dW}{da} = R = G_{IC} = \frac{\pi\sigma_c a}{E} \longrightarrow \sigma_c = \sqrt{\frac{G_{IC} E}{\pi a}} \quad (32)$$

As can be observed, the energy released at constant deformation or constant load is equal, with the small infinitesimal area AECA being the exception.

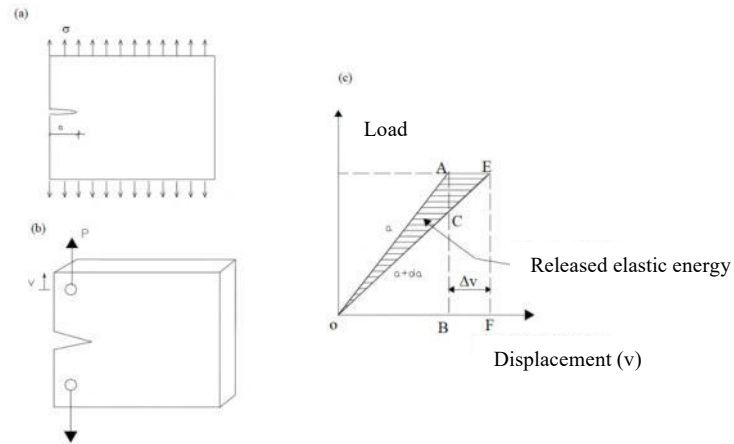


Figure 16. a) A plate with free ends that are under constant tension, b) a plate with free ends that is being loaded, c) energy savings from crack lengthening.

In this case the external loads do produce work, because they are displaced as the crack size increases by a given length, so that, unlike the fixed end plate, the energy stored by the plate increases as the crack extension increases and therefore the energy balance can be represented as:

$$\frac{d}{da} (U - F + W) = 0 \implies \frac{d}{da} (F - U) = \frac{dw}{da} \quad (33)$$

Where W is the energy needed to cause a crack to form, F is the work done by outside forces, and U is the energy stored in the plate. Keep in mind that the sign of dU/da in this instance is the opposite of that in equation 25, which was calculated for a plate with fixed ends. The load P causes a relative displacement v of the application sites in the plate shown in Figure 15b. As a result, when the crack size increases by one length (da), the displacement also rises (dv), and the work done by the load is $F = Pdv$, G can be written as follows:

$$G = \frac{d}{da} (F - U) = \frac{1}{B} \left(P \frac{dv}{da} - \frac{dU_t}{da} \right) \quad (34)$$

If there is no growth in crack size, the displacement is proportional to the load P , and the proportionality factor is the compliance C corresponding to the of the stiffness ($v = CP$). Where U_t is the total elastic energy in the plate of thickness B . As seen in Figure 15b, the elastic energy present in a broken plate is thus:

$$U_t = \frac{1}{2} P v = \frac{1}{2} C P^2 \quad (35)$$

Replacing equation 35 in equation 34 gives the following equation:

$$G = \frac{P^2}{2B} \frac{\partial C}{\partial a} \quad (36)$$

Finally, since the equation is one of the ways to derive LEFM parameters, it is feasible to compute G in terms of the variation of compliance using it. Additionally, the absence of the term dP/da in equation 36 suggests that G is independent of load fluctuation.

2.7 Obtention of fracture energy

2.7.1 Generalities

The fracture energy is a significant characteristic that directly indicates the crack resistance for any material, also the fracture energy refers to the amount of energy necessary for the propagation of a crack per unit area. Its expression is given by the following equation:

$$G_f = \frac{W_0}{A_{lig}} \left(\frac{J^2}{m} \right)$$

Where: A_{lig} is the area and W_0 is the area under the force-displacement curve of the point of application of the force at Jules. In practical applications, it is commonly assumed that the fracture energy of concrete remains constant. The fracture energy or fracture toughness is a crucial characteristic for computational methodologies employed in simulating tensile fracture. The estimation of fracture energy quality relies on three key components: experimental testing techniques, coherent interpretation models, and the utilization of samples for conducting the experiments. In our specific case, synthetic rocks are employed as a substitute for well cores due to the high cost associated with obtaining cores during the drilling procedure, as well as their limited availability for fracture testing, which is inherently destructive [99].

The fracture energy (G_f) is defined as the energy absorbed by the specimen, as indicated by the load-displacement ratio recorded [100] or the energy released by the separation of continuous material, and resultant generation of newly formed surfaces, by splitting, tearing, shearing, cracking and other similarly related phenomena. Since the material has no recollection of the prior load, a crack must expand statically under constant G , resulting in non-linear behavior and a fracture at the crack tip.

Therefore, the crack growth resistance is a constant: $\mathcal{R} = G_f$. Therefore, the quasi-static load path in a \mathcal{G} - a graph is a step function, as shown in Figure 17a below.

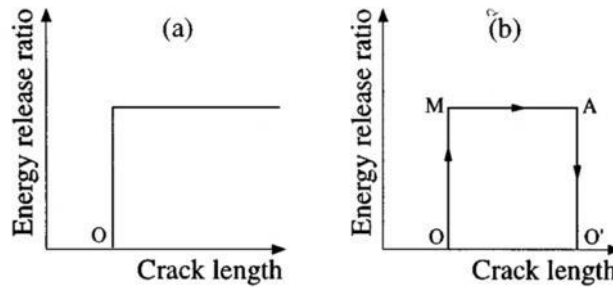


Figure 17. (a) In true LEFM, crack growth must take place under constant \mathcal{G} . (b) A loading- cracking-unloading process in a LEFM specimen.

In contrast, the graph \mathcal{G} - a (crack growth must take place under constant \mathcal{G}) is shown in Figure 17b. Along the segment OM , \mathcal{G} increases while the crack retains its initial length a_0 , along MA , the crack grows under the constant $\mathcal{G} = G_f$. But, if at point A the specimen is unloaded, the crack will not heal, and so the unloading AO' will take place at constant crack length $a = a_1$ down to zero load. The above process can also be represented in $P - u$, i.e., the segments of constant crack length OM y AO' become lines of constant compliance, i.e., straight lines passing through the origin (See figure 18). The MA segment is an iso- \mathcal{G} curve corresponding to $\mathcal{G} = G_f$.

$$u = C(a)P \tag{37}$$

$$G_f = \frac{P^2}{2b} C'(a) \quad (38)$$

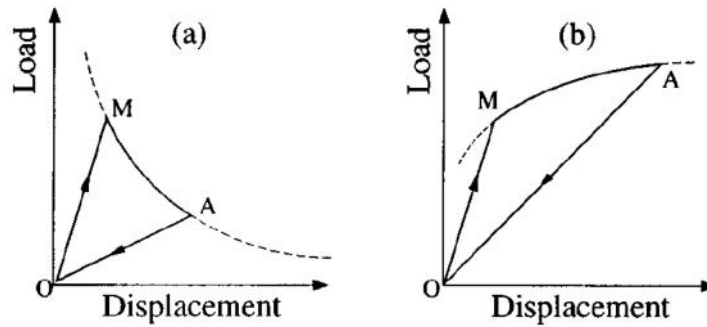


Figure 18. P-u plot of a loading-cracking-unloading in LEFM: (a) For a typical structure where iso-5 curves display downwards slope; (b) for more exotic structures or loadings the slope of the iso-5 curves may be positive.

2.7.2. Traditional methods to obtain the fracture energy

Since there are various ways to calculate the fracture energy, there has been much discussion on how to determine this parameter in both natural and manufactured rocks. The fracture energy value should, in principle, be independent of the measuring technique and the forms of the specimens, but because the findings are so varied, the fracture energy value might occasionally vary depending on the measurement method [101–102]. Traditional methods for obtaining fracture energy in concrete or rocks have been essential in understanding the behavior of these materials under stress and in designing structures that can withstand various loads and environmental conditions. Fracture energy is a critical parameter that characterizes the material's ability to resist cracking and propagating fractures. It plays a vital role in the structural integrity and safety of buildings, bridges, tunnels, and other infrastructure. The fracture energy of concrete and rocks is a measure of the energy required to initiate and propagate fractures within the material. It is a key factor in assessing the toughness and durability of these materials in real-world applications. Traditional methods for determining fracture energy are rooted in physical testing and empirical observations, which have been refined and standardized over the years. These methods typically involve subjecting concrete or rock specimens to controlled mechanical loading conditions and carefully measuring the associated mechanical and geometric parameters. By analyzing the load-deformation response of the material during testing, engineers and researchers can estimate the fracture energy, allowing for a more comprehensive understanding of how these materials behave when subjected to stress. In this context, several well-established traditional methods have been developed, such as the use of standard test specimens like the compact tension (CT) or three-point bending test (TPB) specimens for fracture testing.

These tests provide valuable data on the critical stress intensity factor (KIC) and critical crack tip opening displacement (CMOD), which are used to calculate the fracture energy. Moreover, the Brazilian test and direct tension test are also commonly employed for rocks.

These traditional methods for fracture energy determination have been widely utilized in material characterization, structural design, and failure analysis. They serve as foundational tools for engineers and researchers to ensure the safe and efficient use of concrete and rocks in construction projects, as well as for geological applications where understanding the fracture behavior of rocks is essential for resource exploration and stability assessments. Because the area of the fracture process at the boundary becomes minor in comparison to the dimensions of the sample, it is crucial to keep in mind that the fracture energy acquired must be distinct and unrelated to the type, size, and shape of the specimen [103].

2.7.2.1 Uniaxial tensile test (UTT)

The uniaxial tensile test is one of the most used techniques for determining the fracture energy directly (See figure 19). The factors that should be considered and implemented in this procedure are still up for dispute, and this test is challenging to do and needs specialized equipment. For instance, it's important to manage distortion during the rupture process during testing. Since spinning platens and clamping circumstances might alter the strain-curve, the value of the fracture energy G_f will be off, additional criteria, such as a certain specimen length or test apparatus, are required. If the technology is available, this test is still the "ideal test" to evaluate the uniaxial characteristics of concrete despite the drawbacks it has [104].



Figure 19. Direct uniaxial tension

Over the course of several years, there have been significant modifications in the size, shape, and application of force to the direct uniaxial tension set-up. These changes warrant more examination. One of the initial needs of this technique is to ensure the proper maintenance of the performance of the alignment force line. This is necessary to prevent eccentric loading and ensure appropriate support conditions. Failure to meet these requirements may lead to extremely dispersed outcomes. In accordance with the RILEM 2001 [105] guidelines, it is recommended to employ cylindrical specimens of 150×150mm, featuring a notch size of 15 ± 1 mm positioned at the center of the specimen. Additionally, a 150×150mm cube specimen with a notch size ranging from 2 to 5mm at the center is also suggested for use. The determination of fracture energy in this particular methodology is derived by calculating the integral of the stress-crack width curve (σ - w) [105]. The above-mentioned approach is considered the most straightforward technique for acquiring a stress-deformation correlation and offers a more accurate representation of uniaxial mechanical characteristics when contrasted with the bending test [106].

2.7.2.2 Three-point bending test (3PBT)

A material's bending modulus of elasticity (E_f), flexural stress, flexural strain, and flexural stress-strain response are all assessed using the three-point bending flexural test. A three-point or four-point bend fixture is used in this test, which is carried out using a universal testing machine (sometimes referred to as a tensile testing machine or tensile tester). The three-point flexural test's ease of specimen preparation and testing is one of its main benefits. It is crucial to remember that this approach does have certain drawbacks. The specimen and loading geometry, as well as the applied strain rate, can all have an impact on the test results. To calculate the fracture energy (G_f) from the load-deflection curve produced during a three-point bending test using this approach, a process was devised in the 1980s and 1990s (see figure 20). If we remember, the fracture energy (G_f) was defined as the energy absorbed by the specimen, as indicated by the load-displacement ratio recorded [100]. The following energy-related factors must be considered to calculate the fracture energy from this test.

1. Energy absorbed outside the mode I failure zone must be discarded.
2. To obtain a realistic fracture energy estimate, the compressive strength must be much greater than the tensile strength. If not, too much energy is absorbed in the compression zone.

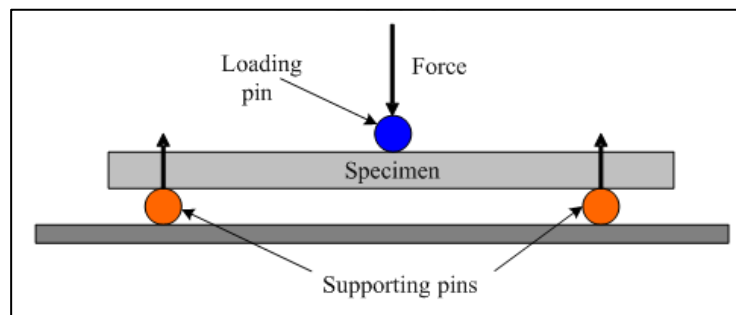


Figure 20. Bending test – three points

The key is to examine the impact of size, a crucial element in fracture mechanics, to respond to the question from the preceding section. The fracture energy G_f , for instance, should be distinct and unaffected by the type and size of the specimens used since the area of the fracture process at the boundary becomes insignificant in comparison to the specimen dimensions if geometrically equal specimens are considered and the ultimate load is correctly extrapolated to a specimen of infinite size. It is imperative to show that roughly the same values of fracture energy are obtained when the value of the fracture energy is optimized to achieve the best fit of the fracture test data with a finite element program, given that the fracture energy is of great interest for finite element programs and that this project validates the obtained values of the fracture energy with finite elements. An essential aspect to contemplate is that during the execution of the three-point bending test (3PBT) to determine the fracture energy, the energy dissipated is attributable to both the applied loading force and the weight of the beam. The weight of the beam may be disregarded in cases where the length of the beam is double the distance between two points of support [107]. Alternative approaches exist for quantifying 3PBT, such as the one provided by Malvar and Warren [108], which involves testing beams with a notch positioned on the upper surface. The weight of the beam is upheld by four springs that are arranged in alignment with the response rollers. The rollers are positioned on bearing pads to limit the dissipation of energy at the bearing points, as referenced in [108]. A regularly employed method for examining fracture parameters is the three-point semi-circle bending test (SCBT) [109–111]. For example, in this project we use this technique considering the technical needs of an Enhanced Geothermal Systems (EGS) and this test is frequently utilized in conjunction with the cohesive crack model. The size of the specimens for the 3PBT are outlined by many standards and individuals.

2.7.2.3 Four-point bending test (4PBT)

The four-point bending test is employed as an additional method for examining fracture in materials. This test closely resembles the three-point bending test (3PBT) in terms of beam configuration. However, in the 4PBT, two halved forces ($F/2$) are applied at specific distances on either side of the notch, rather than being directly applied to the notch at the center of the beam (see figure 21). Consequently, the number of linear variable differential transformer (LVDTs) required for measuring displacement will increase proportionally. It is important to acknowledge that this test adheres to the standards set by the Italian Code UNI (Ente Nazionale Italiano di Unificazione) for the FRC. These standards encompass the evaluation of many parameters such as initial fracture strength, nominal stresses, flexural peak stresses, ductility indexes, CMOD, and CTOD [112]. Moreover, the fracture energy can be determined by calculating the integral of the load-displacement, CMOD curve, a method that is not widely employed in this test. In the context of the 4-Point Bending Test (4PBT), it is seen that the region located between the two loading points experiences pure bending, with the shear stress not playing a significant role in the failure mechanism.

In contrast, it has been shown that the bending moment necessary for the advancement of the fracture under conditions of pure bending is higher than that required for shear failure [113]. Additionally, it has been observed that the impact of span differences is significantly more pronounced in the four-point bending method as compared to the three-point bending method [114]. Previous research conducted on high performance fiber reinforcement concrete has indicated that the flexural peak stresses and fracture energy in 4PBT were found to be greater in comparison to 3PBT, as reported by [115].

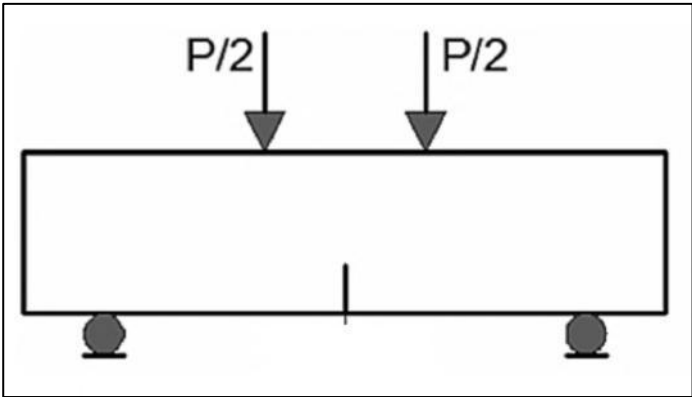


Figure 21. Four-point bending test (4PBT)

2.7.2.4 Compact tension test (CTT)

In their study, Wittmann et al. [116] conducted an evaluation of the fracture energy of concrete using the novel approach of compact tension specimens with an initial notch. It is worth noting that this approach was employed in previous years to analyze the trajectory of fractures [117] and to assess the fracture characteristics in different materials [118]. The present methodology is employed for the evaluation of fracture characteristics in asphalt and concrete pavements, which are more prevalent than beams (See figure 22). In this context, it is worth noting that the disc-shaped compacted tension test (DCTT) is referenced in literature sources [119–122]. Therefore, Holuřová et al. [123] have introduced a novel approach known as the modified compact tension test (MCTT) to determine fracture parameters on cylindrical cross-sectional specimens. The significance of this approach lies in its applicability to both laboratory molds and core drilling in buildings. This procedure involves increasing the maximum depth of the notch in the concrete specimen up to its center and designing holes with diameters of 8 or 10 mm for the installation of rebar. Subsequently, by employing the apparatus to extract the reinforcing bars from either or both sides, an analysis of the fracture parameters can be conducted.

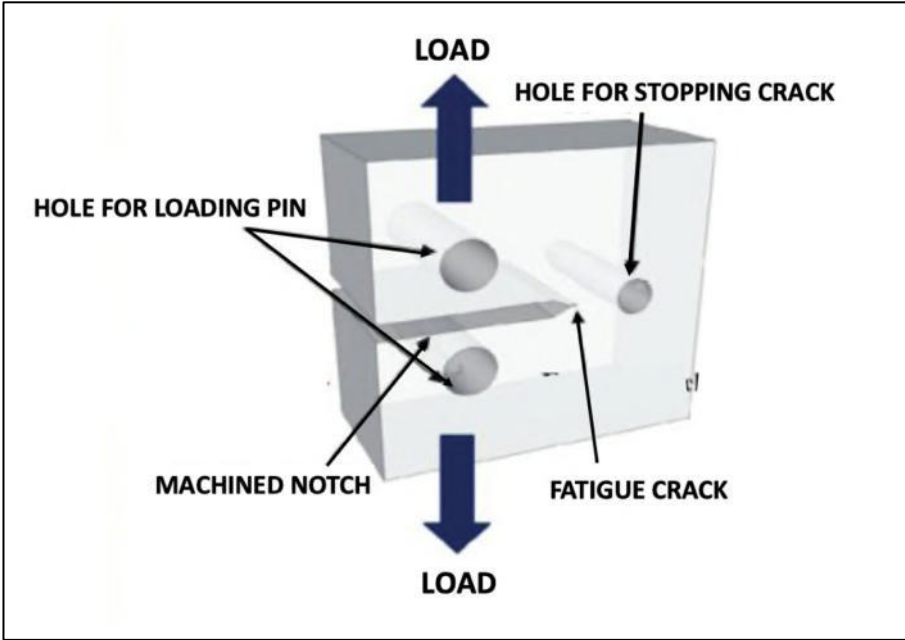


Figure 22. Compact tension test (CTT)

2.7.2.5 Wedge splitting test (WST)

In 1986, Linsbauer and Tschegg [124] published an article with the objective of determining the fracture energy in cubic specimens. The authors Brühwiler and Wittmann [125] devised a novel methodology called the wedge splitting test, which addresses the limitations of the three-point bending test (3PBT) and the compact tension test (CTT). This new approach enables the measurement of fracture characteristics in concrete and related materials. In this particular methodology, the initial step involves the creation of a wedge and a notch within the specimen, which can be accomplished through the utilization of either a saw or a specialized mold. In order to secure the specimen onto the apparatus, it is positioned on a linear support (see figure 23). Two components equipped with rollers are affixed to the specimen in order to facilitate the transmission of load. Next, a rigid steel profile equipped with two identical wedges is securely attached to the apparatus. In this procedure, the load is delivered in a vertical direction, resulting in the division of the specimen into two portions. This division allows for the measurement of the crack mouth opening displacement (CMOD) and the vertical load (P_v). Similarly, the splitting force (P_s) is determined by measuring the horizontal force exerted on the rollers that extend in two directions. The measurement of fracture energy in this method is achieved by calculating the area under the P_s -CMOD curve. Alternatively, the P_v -U curve can also be utilized, however the P_s -CMOD curve is considered to provide more accurate results.

The primary advantage of this methodology is in its ability to mitigate the influence of weight on fracture energy, in contrast to alternative systems where weight can account for 40-60% of the total fracture energy [107]. Furthermore, the utilization of cubic and cylinder specimens is applicable in this methodology, with the cubic specimen being suitable for evaluating the properties of freshly poured concrete, while the cylinder specimen offers advantages in the context of core drilling existing structures. Another notable characteristic of this approach is the convenient management of specimens. Furthermore, it has been indicated that the fracture energy is influenced by both the length of the ligament and the kind of concrete. However, the impact of the specimen shape and the test method on fracture energy was found to be insignificant. According to Flansbjer et al. [126], it was recommended that the dimensions of the specimen should be a minimum of three times the length of the fiber, and ideally four times the maximum length of the fiber. This recommendation was made based on their experimental investigation using the Wedge Splitting Test (WST) on Fiber Reinforced Concrete (FRC) with the indicated dimensions. The authors indicated that the data derived from the WST method exhibited lower variability when compared to those obtained from the 3PBT method. Additionally, they established a correlation between the CMOD and CTOD parameters.

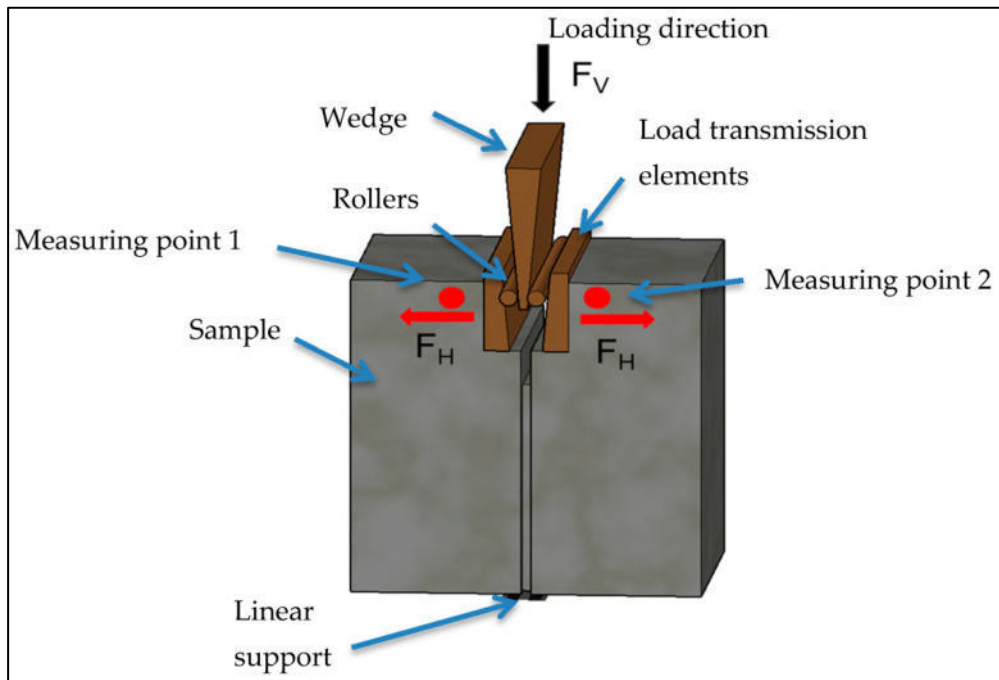


Figure 23. Wedge splitting test (WST)

2.7.2.6 Size effect method

The size effect method approach involves conducting tests on multiple specimens of different sizes that are geometrically similar and contain notches, with the aim of determining the maximum load. For statistical reasons, at least three identical specimens should be tested for each specimen size then the nominal resistance is calculated, its plot versus size is considered, and the parameter values Bf'_t and D_0 are obtained by a least-squares optimal fit of the size effect law for the experimental results. Finally, K_{IC} , G_f and c_f are obtained by the following equations:

$$K_{IC} = Bf_t \sqrt{D_0 K_0} \quad (39)$$

$$G_f = \frac{(Bf_t)^2 D_0 K_0^2}{E'} \quad (40)$$

Where: E' : Young modulus, G_f : Fracture energy, D_0 : depends on the geometry of the sample,

K_{IC} : fracture toughness

This method is applicable only for specimens of positive geometry, i.e., those for which $k'(\alpha_0)$ is positive (and not very small). When $k'(\alpha_0)$ is approximately zero or negative, the method is not applicable. This happens, for example, during initial crack growth in a specimen with central crack loaded over the crack. RILEM recommends determining the fracture characteristics of the material from the size effect law (RILEM 1990b). The idea of this method is that first the size effect law parameters are determined by linear regression I and then the fracture parameters of the material, as this method works equally well for various geometries, but beams with three-point bending are recommended for standardization purposes. For example, during the tests, the loads and reactions are applied through one hinge and two rollers with a minimum possible rolling friction, and through stiff bearing plates (of such a thickness that they could be considered as rigid). The bearing plates are either glued with epoxy. The distance from the end of the beam to the end support must be sufficient to prevent spalling and cracking at beam ends. The span-to-depth ratio of the specimen, S/D , should be at least 2.5 (this has been set only for the purpose of standardization; the theory does not prevent smaller values). The ratio of the notch depth to the beam depth, a_0/D , should be between 0.15 and 0.5. The notch width at the tip should be as small as possible and must not exceed $0.5d_a$ where d_a = maximum aggregate size. The width b of the beam and the depth d should not be less than $3d_a$ and in very important that the specimens should be loaded at constant (or almost constant) displacement rates.

2.7.3 Comparison between different methods to obtain the fracture energy

Fracture energy is recognized as a fundamental characteristic of materials, enabling the estimation of their behavior, including the energy necessary for crack development and subsequent failure. In previous studies, researchers have examined various methods for determining fracture energy, including the Wedge Splitting Test (WST) and three-point bending test (3PBT). These methods have gained popularity due to their ease of use in investigations and their widespread recognition compared to alternative approaches. Fracture energy (G_f) is an inherent property of materials. In the techniques mentioned above, certain material characteristics need to be considered, such as specimen dimensions, notch size, various specimen shapes, support positions, loading rates, and so on. It is important to ensure that these factors do not have an impact on the fracture energy. Indeed, these elements are responsible for the differences observed in mix design. These factors encompass the incorporation of fibers, alterations in the water-to-cement ratio, inclusion of pozzolans, adjustments in the ratio of fine aggregate to coarse aggregate, modifications in the maximum aggregate size, and variations in the curing conditions, among others [107]. The size effect method is capable of yielding fracture energy values that are deemed acceptable by utilizing the equation $\frac{G_F}{G_f} = x$.

However, it is important to note that this method solely considers the maximum load and does not consider the displacement of the specimens. This requirement poses a challenge when there are limitations on the availability of specimens. However, it should be noted that certain techniques, including the compact tension test (CTT) and the uniaxial tensile test (UT), do possess certain drawbacks. These include a heightened susceptibility to external influences, the possibility of energy consumption beyond the fracture process zone (FPZ), limited research and analysis, as well as challenges associated with their practical implementation [127-129]. The material parameter, rather than a number depending on sample size, is the appropriate input for computational analyses such as the cohesive fracture model employed by Li et al. or a damage-based model [130-131]. However, the specimens examined by Li et al. consisted of prismatic beams featuring curved notches, necessitating the presence of a substantial rock block from which samples could be fabricated. Hence, the utilization of a methodology that disregards the specific characteristics and arrangements of specimens in traditional approaches for calculating fracture energy would prove advantageous in unique scenarios, such as those encountered in geothermal reservoirs or oil fields. In these contexts, the cost-intensive extraction of rock specimens, their incompatibility with most methods, and the impracticality of conducting on-site tests necessitate the transportation of samples to a laboratory for testing purposes. The research introduces an alternative approach for determining fracture energy. This method relies on an energy balance analysis of hydraulic fracture tests conducted on a laboratory-scale analog model of an "EGS" system, designed to simulate a real geothermal reservoir. By considering kinetic, potential, and pressure energy during the fracture test, an approximate estimation of fracture energy can be obtained, eliminating the requirement for specific geometrical characteristics in the test specimens.

2.7.4 Effect of temperature on the fracture energy

Given the significance of temperature as a crucial variable in this study, it is noteworthy that both permeability and hydraulic fracture tests were conducted at a temperature of 100° C but in a different setup than the tests previously reported, but in general, it can be observed that the fracture energy tends to decrease with increasing temperature for the types of tests, according with some authors. However, the extent of this energy reduction is contingent upon the water-to-cement ratio. Specifically, when the temperature rises from +25 °C to +800 °C with a water-to-cement ratio of 0.23, the fracture energy experiences a decrease of approximately 37%. Similarly, for a water-to-cement ratio of 0.31, the fracture energy decreases by approximately 21% [132]. According to Nielsen's experiment [133], when the temperature is raised from 3 °C to 400 °C, there is an observed rise of approximately 50% in fracture energy. This can be attributed to the thermal degradation that causes the failure zone to become more convoluted.

The findings of Zhang and Bicanic's experiment [134] demonstrate that when the temperature increases from 20 °C to 105 °C and 150 °C, there is a drop in fracture energy. However, as the temperature continues to rise to 450 °C, the fracture energy exhibits an upward trend, surpassing that of concrete at 20 °C. According to certain scholars, the reduction in temperature has been seen to enhance fracture energy. However, there exists a divergence of opinions on the effect of temperature elevation. The mechanical properties of concrete, particularly its compressive strength, experience a significant decrease when exposed to elevated temperatures. Consequently, it is anticipated that the fracture energy will exhibit a linear reduction [107]. The prevailing consensus in the scientific community is that fracture is a rate process that is activated by thermal factors. This implies that the atomic bonds that lead to fracture are initiated by the energy from thermal vibrations [135]. The energies in question exhibit a statistical distribution, specifically characterized by the Maxwell distribution. An increase in temperature leads to a corresponding increase in the likelihood or frequency of an atom's energy surpassing the activation energy barrier associated with the bond. As the dimensions of the coarse aggregate rise, cracks are required to traverse a longer distance to propagate around the coarse aggregate. In addition, it should be noted that the presence of coarse aggregate contributes to the establishment of interlocking mechanisms within the aggregates, hence resulting in an elevation of the energy required for crack propagation. The findings indicate that an increase in the maximum size of aggregate leads to an increase in ductility, a decrease in the slope of the post-peak section, and a rise in the tail of the load-displacement curve.

According to a study [136], it has been shown that the fracture energy exhibits an upward trend as the volume content of aggregates increases, reaching its peak at a fraction of 0.60. However, beyond this point, there is a notable decline in the fracture energy. A study was conducted by multiple researchers to investigate the relationship between fracture energy and aggregate size. The experiment involved varying the aggregate size, with a minimum size of 9.5 mm. The results showed that the fracture energy was increase exhibited a logarithmic increase as the aggregate size increased [137-140]. In another study conducted by Kallel et al. [141], it was observed that the fracture energy of concrete exhibits an upward trend as the temperature increases. The investigation focused on evaluating the mechanical characteristics of concrete, including fracture energy, tensile strength, and elastic modulus, while controlling relative humidity, temperature, and pressure variables. The researchers reached the conclusion that the fracture energy is influenced by both the level of water saturation and the temperature of the specimens, which were subjected to testing at temperatures of 110° C, 140° C, and 160° C. The fracture energy demonstrates an upward trend in response to both elevated temperature and increased degree of water saturation. The fracture energy has a positive correlation with both temperature and the extent of water saturation. In addition, the investigation involved the assessment of the variations in fracture energy (G_f), modulus of elasticity (E), and tensile strength (F_t) across varied degrees of water saturation, specifically at temperatures of 110, 140, and 160 °C.

The experimental findings unambiguously demonstrate a positive correlation between fracture energy and both temperature and degree of water saturation. Additionally, the results indicate a negative relationship between temperature and both modulus of elasticity and tensile strength. Moreover, the relationship between the degree of water saturation and both modulus of elasticity and tensile strength follows a U-shaped curve. During the fracture process, the material undergoes changes that result in increased flexibility, as indicated by a reduced modulus of elasticity. Additionally, the material experiences a decrease in tensile strength, rendering it weaker. Furthermore, the fracture process leads to an enlargement of the Fracture Process Zone (FPZ), indicating a larger fracture energy [141].

In summary, concrete is typically characterized as a material with low tensile strength and high compressive strength when subjected to ambient temperatures. The material exhibits an asymmetrical response under tension and compression, wherein its tensile strength is significantly lower in comparison to its compressive strength. Experiments using multiple compression cycles beyond the "elastic" region reveal a decline in mechanical characteristics (damage), alongside consistent deformations resulting from material cracking. Concrete exhibits a certain behavior, as evidenced by a cyclic tensile-compression test. This test involves the restoration of the material's stiffness as it transitions from a state of tension (cracks opening) to a state of compression (cracks re-closing) [142]. The mechanical characteristics of a material undergo significant changes due to numerous physicochemical transformations, microcracks, and moisture migrations that occur when the temperature rises. The behavior of concrete under elevated temperatures is influenced by various factors, including the specific conditions of the testing process (such as the rates of heating and cooling, the presence of mechanical load, and the prior application history), as well as the condition of the specimens during the testing phase (whether they were tested while still hot, after cooling, or after a certain period following cooling). Based on the findings reported in the existing literature, it can be inferred that the fracture energy is influenced by various factors, including the composition of the concrete, the temperature at which the concrete is subjected to testing, and the level of water saturation inside the concrete. The findings regarding the relationship between fracture energy and temperature exhibit conflicting outcomes, which can be attributed to variations in concrete composition and the initial moisture content of the specimens.

The fracture energy of rocks is known to be temperature-dependent. As the temperature increases, the fracture energy generally decreases. This is primarily due to the thermally induced weakening of the rock matrix. Elevated temperatures can lead to thermal expansion and microstructural changes, reducing the material's strength and resistance to crack propagation. Therefore, understanding how temperature affects the brittle behavior of rocks is a key topic of concern in many subsurface engineering sectors (such as coal mining, geothermal energy, nuclear waste disposal, and rock drilling).

The mechanical properties of rocks can change considerably with a slight rise in temperature up to around 250° C, which is an expected range for conventional or hot fracture rock geothermal energy systems and for the disposal of conventional high-level radioactive waste. Projects including the Enhanced Geothermal System (EGS) technology, for instance, have been extensively developed and disseminated since the 1970s. Massive rock blocks are encountered at temperatures of 250° C in conventional geothermal resources in EGSs, and hydraulic fracturing is employed to increase well productivity and injectivity [152]. The physical and mechanical qualities of rocks will change over time as a result of high temperatures. For instance, rock strength, fracture characteristics, elastic modulus, and porosity all change. By examining some basic mechanical properties of rocks under the influence of temperature, such as Young modulus, Poisson's ratio, uniaxial compressive strength, and uniaxial tensile strength, Oda [150] was able to arrive at the change law of the basic mechanical properties of rocks with temperature and the failure criterion. Investigation by Hong et al. [151] revealed that the physical characteristics of sandstone treated at high temperatures change significantly from those at low temperatures, with the difference being most pronounced when the treatment temperature exceeds 500 C.

2.8 Stresses intensity factor

To avoid the singularity problem at the tip, where, according to the answer, the stresses go to infinity upon application of any external load, Griffith suggested the crack extension criteria based on an energy balance analysis. He also established that this technique is fundamentally the same as the energy approach and that there is a link between them by expressing the crack extension problem in terms of the stress state of the material at the tip. This is one of the most significant advancements in LEFM. The fracture process, as proposed by the elastic theory, could not be concentrated at a single point, according to his subsequent

publication. Instead, it occurs in a small region near the tip that he designated the plastic zone or fracture process zone (FPZ), which, due to deformation, absorbs a significant amount of energy and keeps stresses within a finite range [143]. Irwin used the Airy stress function (ψ), a particular function that in this case must simultaneously satisfy the specific conditions of stresses, strains, and stress-strain compatibility that occur in that sector, to determine the stress distribution around the crack tip in a plate, as shown in Figure 17a. Different complex functions can be used to solve the Airy stress function (ψ). The Westergaard solution can be used if the cracking is of mode I, in which case the stress field around the fracture tip in Figure 24 is provided by:

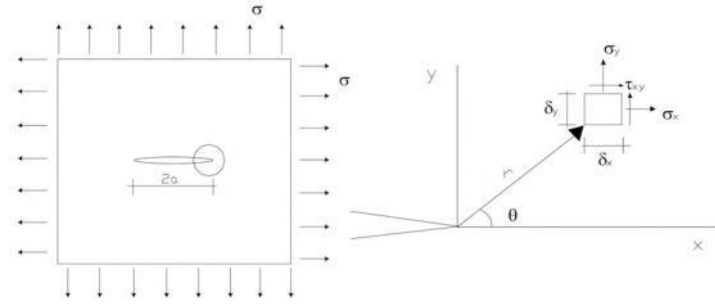


Figure 24. Stress field near the crack tip

$$\sigma_x = \sigma \sqrt{\frac{a}{2r}} \cos \frac{\theta}{2} \left[1 - \text{sen} \frac{\theta}{2} \text{sen} \frac{3\theta}{2} \right] \quad (41)$$

$$\sigma_x = \sigma \sqrt{\frac{a}{2r}} \cos \frac{\theta}{2} \left[1 + \text{sen} \frac{\theta}{2} \text{sen} \frac{3\theta}{2} \right] \quad (42)$$

$$\sigma_x = \sigma \sqrt{\frac{a}{2r}} \text{sen} \frac{\theta}{2} \cos \frac{\theta}{2} \cos \frac{3\theta}{2} \quad (43)$$

Or generally by::

$$\sigma_{ij} = \frac{K_I}{\sqrt{2\pi r}} f_{ij}(\theta) \quad (44)$$

Where $f_{ij}(\theta)$ is a function of θ and K_I is the stress intensity factor (TIF) for mode I cracking and can be expressed as:

$$K_I = \beta \sigma \sqrt{a} \quad (45)$$

Where a is the length of the initial crack or burst initiates and β is a dimensionless factor, which corresponds to $\sqrt{\pi}$ and in such a case for an infinite plate.

$$K_I = \sigma\sqrt{\pi a} \quad (46)$$

For an element of finite size, β depends on the the geometry of the stressed body, which is generally expressed as the length (L) of one of its dimensions. Usually, the FITs of these elements are described in terms of the FIT of the infinite plate, such that the factor $\sqrt{\pi}$ is taken out of β and the equation is expressed as:

$$K_I = B\left(\frac{a}{L}\right)\sigma\sqrt{\pi a} \quad (47)$$

The significance of the stress intensity factor thus rests in the ability to fully identify the stress field surrounding a fracture by knowing K_I . The principle behind K_I suggests that if two cracks in different structures have the same KI and are subjected to the same cracking mode, similar behavior in terms of crack advance or stability should be anticipated because the stress field is the same in both cases. As a result, K_I constitutes a useful similarity parameter to compare the cracking characteristics of elements of the same material but with different geometry and crack length. Therefore, when the critical stress intensity factor (K_{IC}) sometimes referred to as fracture toughness, is reached, a crack will begin to spread. The value of K_{IC} , which is a property of the material and according to equation 47 is given by: may be derived via fracture testing for a situation in which the stress is the critical one ($\sigma = \sigma_{cr}$):

$$K_{IC} = B\left(\frac{a}{L}\right)\sigma_c\sqrt{\pi a} \quad (48)$$

The conditions listed below provide the crack progress criterion in terms of the stress intensity factor similarly to the energy release rate approach:

- If $K_I < K_{IC}$, then there is no crack extension (49)

- If $K_I = K_{IC}$, then possible quasi-static crack extension (50)

- If $K_I > K_{IC}$, then dynamic crack growth (51)

From equation 31 and 46, the relationship between energy release rate and stress intensity factor under plane stress condition can be expressed as:

$$G_{IC} = \frac{K_{IC}^2}{E} \quad (52)$$

And for the case of plane deformation the relation is:

$$G_{IC} = (1 - \nu^2) \frac{K_{IC}^2}{E} \quad (53)$$

Where ν is the Poisson's ratio, equations 52 and 53 are known as Irwin's equations, which are fulfilled not only for the critical condition but also for any other condition below the critical one, i.e., general relations between G_I and K_I .

2.8.1 Dynamic fracture

Fast motions are produced during the fracture process, making the effects of inertia significant. They must thus be considered. The stresses and displacements brought on by dynamic loading might be very different from those linked to the equivalent static loading, according to elastodynamic analysis of cracking issues. The dynamic stresses are more substantial than the comparable static stresses at places in the body. The interaction of elastic waves with fracture faces and other distinctive body boundaries can be used to explain this outcome. Additionally, how long the applied load is kept inside the solid affects the material's mechanical characteristics. For instance, in most metals, yield strength and fracture toughness rise with loading rate. High stress levels are caused by dynamic loading, and fracture happens so quickly that there isn't enough time for creep to form. As a result, energy is released quickly, which causes rapid crack propagation; this may help to explain why dynamic loads tend to favor brittle fractures.

In summary, dynamic fracture mechanics problems fall into two categories.

- The first is concerned with a situation when a crack reaches a point of instability and advances quickly while being subjected to a slowly changing applied load, so that an abrupt unloading along the fracture path results.
- The second is concerned with the dynamic issues that occur when a body with a stationary crack is exposed to a quickly fluctuating load, such as an impact or impulsive load or crack development start, velocity, branching, or arrest.

Consequently, the following is a definition of the dynamic crack problem: It is important to understand the circumstances surrounding fracture initiation, crack development, and crack arrest because a solid body with an initial crack is exposed to a time-dependent stress. The three components, such as crack displacement and crack length, must be calculated as a function of time to find a solution to the issue. Four equations may be used to calculate these four unknown values using the three equations of motion and a fracture criterion [144]. Mott advanced Griffith's theory by include kinetic energy in the formulation of the system's total energy. He then looked for the configuration that maintains this total energy constant and produced a hypothesis [equation 54] that quantitatively predicts the velocity of a fast-moving crack. For instance, Mott considered the issue of the spread of a central fracture in an infinite plate when it was subjected to a uniform, time-independent uniaxial force that was perpendicular to the crack's plane.

Along with the foregoing, he also made the following crucial assumptions:

- The static problem's stress and displacement fields and the dynamic problem's stress and displacement fields both have the same fracture length.
- The crack moves at a constant velocity.
- The fracture velocity is low in comparison to the body's shear wave velocity.

Therefore, the kinetic energy term K , is given by:

$$K = \int_V \frac{1}{2} \rho u_k \dot{u}_k dV \quad (54)$$

where V stands for body volume, u_k for displacement component, and ρ for mass density. A dot above a letter indicates a typical temporal differential.

2.8.2 Crack growth based on energy balance

New surfaces are produced when a solid is shattered. Due to the tremendous stresses produced, atomic bonds break, resulting in the separation of the material. According to numerous scholars, the scale of observation of a solid affects the phenomena of fracture. The interesting processes in the material take place at centimeter-scale distances from an atomic perspective. The continuum method considers how a material behaves at lengths longer than a few centimeters. The continuum method uses theories of continuum mechanics and classical thermodynamics, whereas the atomistic approach uses quantum mechanical principles to study the issue.

Understanding how these two techniques interact is one of the fundamental goals of fracture mechanics. In contrast to the size and properties of the microstructure, the continuum mechanics approach to a fracture ignores the occurrence of major flaws and views a material as a homogeneous continuum. A stress analysis and a theory that predicts when a fracture will happen are required to analyze the phenomena of crack development, voids, or other existing flaws. Several criteria that involve a quantity with a critical value that gauges the material's resistance to separation and a quantity that must be connected to the loss of continuity have been put forth. Consider a crack of area A in a continuum that is deformable and is being loaded arbitrarily. According to the rule of conservation of energy, we have:

$$\dot{W} = \dot{E} + \dot{K} + \dot{\Gamma} \quad (55)$$

where \dot{W} is the work done by the applied loads per unit of time, \dot{E} and \dot{K} are the body's internal and kinetic energy change rates, and $\dot{\Gamma}$ is the energy used to widen the fracture over time. A dot above a letter indicates a difference in relation to time.

The internal energy E can be put in the next form:

$$E = U^e + U^p \quad (56)$$

Where U^e represents the elastic strain energy and U^p the plastic work.

If the applied loads are time-independent and the fracture propagates slowly, the kinetic factor \dot{K} is small and may be excluded from the energy balance equation (55). We may claim that changes in crack size are the cause of all changes about time.

$$\frac{\partial}{\partial t} = \frac{\partial A}{\partial t} \frac{\partial}{\partial A} = A \frac{\partial}{\partial A}, A \geq 0 \quad (57)$$

and Equation 55 becomes,

$$\frac{\partial W}{\partial A} = \left(\frac{\partial U^e}{\partial A} + \frac{\partial U^p}{\partial A} \right) + \frac{\partial \Gamma}{\partial A} \quad (58)$$

The rate of work given to the continuum by the applied loads, which is equal to the rate of the elastic strain energy and the plastic strain work plus the energy lost during fracture propagation, is represented by the energy balance during crack growth in Equation 58. Equation 58 may thus be written as:

$$-\frac{\partial \Pi}{\partial A} = \frac{\partial U^p}{\partial A} + \frac{\partial \Pi}{\partial A} \quad (59)$$

Where:

$$\Pi = U^e - W \quad (60)$$

is the potential energy of the system. Equation 58 shows that the rate of potential energy decrease during crack growth is equal to the rate of energy dissipated in plastic deformation and crack growth.

2.8.3 Graphical representation of energy balance equation

Figure 22 illustrates the elements of the energy balance equation graphically and sheds light on the variance that occurs during crack formation. Therefore, in Figure 25, the straight-line OA represents the load-displacement response of a body of constant thickness with an initial fracture of length a_1 . For instance, during loading up to point A, the body stores elastic strain energy represented by the area (OAC), which is later released during unloading.

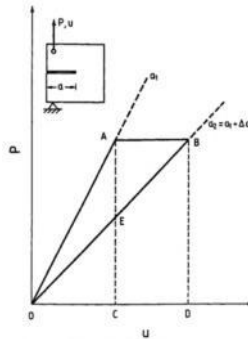


Figure 25. Load-displacement response of a cracked plate for propagation of a crack from length a_1 to a_2 under "fixed grips" conditions along AB.

Assume that the crack starts to spread at point A and moves consistently to a new length, $a_2 = a_1 + \Delta a$. The load-displacement response of the body with a fracture greater than the length a_2 is represented by the straight-line OB. Since the stiffness of the body significantly reduces as fracture length increases, the line OB must be below the line OA as the load lowers from point A to point B during crack propagation. The area (OBC) is a representation of the elastic strain energy that is stored in the body at point B. The unloading path will follow line BO if the load imposed at point B is removed. Since the point of stress, application, and crack development are fixed, the body does not require any extra labor.

The area (OAB) symbolizes the decrease in strain energy experienced during fracture development. It is the rate of elastic energy release that is determined and is balanced by the material's resistance to crack expansion (2γ).

$$G = \frac{(OAB)}{\Delta a} = 2\gamma \quad (61)$$

2.8.4 Basic load-displacement relationship

During fracture growth, load and displacement alter. The specimen's form and the kind of testing device have a significant impact on the load-displacement response. The critical load for fracture formation with Griffith energy balance results from the body's ability to save energy. When the system's energy is at its maximum and smallest points during equilibrium, crack formation is regarded as unstable. As a necessary requirement for crack stability,

$$\frac{\partial^2(\Pi + \Gamma)}{\partial A^2} \begin{cases} < 0 \\ > 0 \\ = 0 \end{cases} \text{ unstable fracture, stable fracture, and neutral equilibrium.} \quad (62)$$

where equation 60 defines the system's potential energy Π . In the following, two example problems with respect to crack stability will be considered. The first concerns a linear crack in an infinite plate subjected to a uniform stress perpendicular to the crack axis. The potential energy of the system $\Pi = -U^e$, where U^e and $\Gamma = 4\gamma a$. The terms Π , Γ and $(\Pi + \Gamma)$ are plotted against half crack length a (see figure 26). Observe that the total potential energy of the system $(\Pi + \Gamma)$ at the critical crack length presents a maximum, which corresponds to unstable equilibrium.

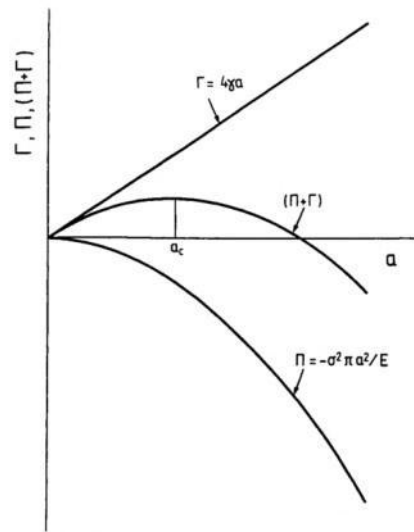


Figure 26. Potential energy, Π , surface energy, Γ , and the sum of potential and surface energy, $(\Pi + \Gamma)$, for a line crack in an infinite media exposed to a homogeneous force perpendicular to the crack axis, against crack length a .

2.9 Numerical finite element simulations and compliance method

In fracture mechanics, the finite element method (FEM) is a technique for crack issue solving. Swedlow, Williams, and Yang's paper from 1960 contained the first use of the finite element approach [145]. The quarter point element was then put out by Henshell, Shaw, and Barsoum in 1975 to get an exact solution at the fracture tip. The extended finite element technique (XFEM), which enables the crack propagation to be estimated without remeshing the finite elements, was recently presented. Blenzley created the enriched elements in 1974 [146]. The fact that the generic isoparametric element and the finite element have a 5–10% inaccuracy is crucial to consider. Additionally, they cannot guarantee solutions close to the fracture tip when using a high mesh number. The singularity of the stress or strain field surrounding the fracture tip, as seen below, is what causes this.

The fracture energy is determined through an alternative methodology that involves an energy balance analysis during hydraulic fracture experiments. This methodology is subsequently applied to mortar and rocks using a laboratory-scale analog model known as the "EGS" model, which is designed to replicate the behavior of a genuine geothermal reservoir. To calculate the extent of the fractured surface, numerical finite element simulations are employed. Nonlinear fracture mechanics theories are widely acknowledged to provide a more precise representation of cracking phenomena in quasi-brittle materials, such as concrete [147], when examined from a numerical perspective. Nevertheless, the linear fracture mechanics theory (LFTM) has been modified to yield significant findings, as demonstrated by Bazant and Kazemi in 1990 [148] In our case, the complacency method was used.

The reciprocal of the stiffness coefficient K , shown by the symbol λ , represents the state of complacency. The determination of the quantity is accomplished through the division of the displacement, symbolized as u , by the corresponding force, designated as F . The relative complacency, denoted as λ , is a measure that quantifies the ratio between the complacency, λ , and the initial elastic complacency, λ_0 . The experimental protocol entails conducting partial loading and unloading cycles at predefined intervals during the study. The estimation of fracture lengths at each unloading event can be achieved by utilizing the slopes at unloading, which are obtained from analytical elastic compliance relationships. The evaluation of crack propagation is deduced from compliance measurements performed using an extensometer positioned at the notch lip's entrance. The J-integral value pertaining to the propagation of this crack is calculated by considering the maximum force observed during each cycle. The objective is to achieve consistent and regulated transmission (i.e., along a specified distance) that can be assessed after the specimen's demise, as opposed to erratic transmission (which may result in specimen fracture and hinder the observation and measurement of prior consistent transmission). After conducting the test, the specimen is subjected to fatigue-induced fracture, which exposes the fracture surfaces and allows for the identification of stable crack propagation. This differentiation between the test procedure and the fatigue stages (pre-cracking and post-cracking) is facilitated by the contrasting textures observed. To conclude. The complacent method entails the deliberate initiation of partial discharges at predetermined times throughout the testing process. Crack propagation is approximated by utilizing analytical elastic compliance relationships, considering the linear and independent nature of the slopes of each discharge, which are unaffected by plastic deformation. The level of compliance exhibits an upward trend as the crack advances during the test.

2.9.1 Spatial and temporal discretization of boundary value problems

A approach known as the finite element method is based on the numerical application of energetic mechanical principles that are discretized in space and time. It's also employed to roughly solve an Initial Boundary Value Problem (IBVP). As a result, many finite subdomains V_e , finite elements, and simplified formulations are created for the considered body or item to be researched (See figure 27). The finite elements are numbered with index $e=1, \dots, n_E$ and in the next figure show the example of a spatial discretization of the boundary value problem of a tension strap [149].

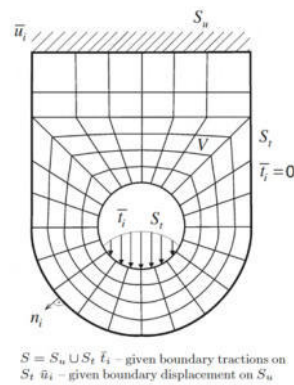


Figure 27. Finite element discretization: a tension strap [149].

In the case of initial boundary value problems or non-linear problems, the transient temporal progression $[t_0 \leq t \leq t_{\text{end}}]$ is generally discretized with a sequence of time steps or load increments Δt_i .

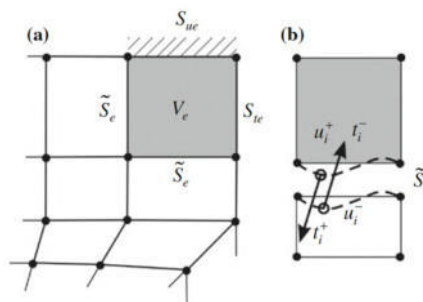


Figure 28. a) Detailed view of a finite element, b) transition conditions to the neighboring element [149].

In the figure 28 show with more detail the figure 31, in which the element e has been highlighted. Belonging to element e are its volume V_e and its boundary $S_e = S_{ue} \cup S_{te} \cup \check{S}_e$. S_{ue} and S_{te} represent the intersections of S_e with the displacement or traction boundaries S_u or S_t of the IBVP. Every element also borders other elements on the section of its boundary marked by the underscore (\check{S}_e). These interelement boundaries' total value is denoted by the symbol \check{S} . An overbar serves as a representation of all external, provided field quantities. Quantities that are only specified on the border are denoted by a tilde. These interelement boundaries' total value is denoted by the symbol \check{S} . An overbar serves as a representation of all external, provided field quantities. Quantities that are only specified on the border are denoted by a tilde.

The following fundamental relations must be met by the field quantities in the finite elements to solve a BVP:

- The displacement field u_i is a continuous function of location.
- The displacement field u_i must take on prescribed values u_i on section S_{ue} of the boundary
- Balance of the stress state with the body forces b_i inside the element
- Tractions on boundary section S_{te} correspond to the external given values \bar{t}_i
- Continuity of displacements at the interelement boundaries \check{S}_e , i.e. the value must be the same if approached from both elements
- Reciprocity of the traction vectors (actio = reactio) on the interelement boundaries
- The stress-strain law and we will first assume linear-elastic material properties.

2.9.2 Energy Principles of continuum Mechanics

The starting point of our examination will be the generalized principle of work. It states that the internal work W_{int} of a statically admissible stress field σ_{ij}^{sta} performed with a kinematically admissible displacement field u_i^{kin} is equal to the work W_{ext} done by external stresses t_i^{-sta} and b_i^{-sta} with associated displacement field u_i^{kin} :

$$\mathcal{W}_{int} \hat{=} \int_V \sigma_{ij}^{sta} \varepsilon_{ij}^{kin} dV = \int_{S_t} \bar{t}_i^{-sta} u_i^{kin} dS + \int_V \bar{b}_i^{-sta} u_i^{kin} dV + \int_{S_u} t_i^{-sta} u_i^{kin} dS \hat{=} \mathcal{W}_{ext}. \quad (54)$$

We can also apply to the true stresses $\sigma_{ij}^{sta} := \sigma_{ij}$ of the BVP and the true increments of the kinematic quantities $u_i^{kin} := du_i$ and $\varepsilon_{ij}^{kin} = d\varepsilon_{ij}$ of a non-linear analysis. Integration over all load steps from the undeformed initial state to the final state then results—for any material law—in the identity of internal work (work of deformation) and the work of external forces:

$$\mathcal{W}_{int} \hat{=} \int_V \int_0^{\varepsilon_{ij}} \sigma_{ij} d\varepsilon_{ij} dV = \int_S \int_0^{u_i} \bar{t}_i du_i dS + \int_V \int_0^{u_i} \bar{b}_i du_i dV \hat{=} \mathcal{W}_{ext}. \quad (55)$$

2.9.3 Variation of Displacement Field

We assume that the body is under a condition of stress that is in equilibrium with the external system of forces. A virtual displacement is now performed in addition to the real displacements u_i . It is described as a continuous function of x with the qualities listed below [149]:

- (a) infinitesimal (compared to u_i),
- (b) imagined, i. e. not existing,
- (c) kinematically admissible, i. e. $\delta u_i = 0$ on S_u , so that the boundary condition $u_i = \acute{u}_i$ is not violated.

The virtual displacements principle:

If the work of applied external forces equals the deformation work of internal forces with an arbitrary kinematically acceptable virtual displacement field δu_i , or if the total virtual work is equal to zero, a deformable body is precisely in the condition of equilibrium. For every material law, this is true.

$$\delta W = \delta W_{int} - \delta W_{ext} = 0. \quad (56)$$

CONTRIBUTION

The thesis work has made several contributions. First, in the experimental part is the development of a new method to calculate the fracture energy based on a mechanical experiment of hydraulic fracturing and considering the continuity and Bernoulli equation and an energy balance. This method helps to estimate the fracture energy in situ, in other words, what occurs at typical temperatures of geothermal reservoirs, which is not possible with traditional methods. In the numerical part, a code was written to obtain finite element simulations and calculate the fracture energy and corroborate the values obtained in the first and second stages of the project. With this method we can calculate the energy required to create a unitary surface discontinuity without the need of specimen fabrication or in case we have a limited number of specimens. Also, this contribution can increase the efficiency of permeability in geothermal reservoirs for more efficient use of energy, which in turn can modestly mitigate the effects of climate change by replacing fossil energy with geothermal energy because at present, it is an energy that is little known and researched.

The scientific contribution of the offered text to a PhD thesis can be succinctly described as follows:

- The present analysis draws attention to the insufficient exploitation of geothermal energy and the prevalent dependence on hydraulic fracturing for the purpose of reservoir optimization. The identification of a research gap is achieved by placing emphasis on the necessity for a comprehensive comprehension of fracture energy inside bedrock.
- Introduction of an Alternative Measurement Method: This work presents a novel approach to quantify fracture energy in quasi-brittle materials by employing an energy balance during hydraulic fracture experiments. This methodology offers a viable alternative to current experimental methodologies.
- This study provides an analysis of experimental data pertaining to synthetic rocks composed of mortar and limestone. The data encompasses both mechanical and hydromechanical properties, allowing for a comprehensive characterization of these materials. The provided data presents fracture energy values under varying temperatures and circumstances, hence illustrating the effectiveness of the proposed measurement technique.

- The study investigates the impact of temperature on fracture energy, observing a substantial rise in fracture energy with increasing temperature for both limestone and mortar. These findings offer vital insights into the optimization of geothermal reservoirs.
- The text highlights that the fracture energy estimates underwent rigorous inspection to validate the suggested measurement method, hence demonstrating its dependability and credibility. The outcomes of this study highlight the potential practical implications for the implementation of geothermal reservoirs.

In general, this Ph.D. thesis makes a significant addition to the study of geothermal energy and fracture mechanics, providing a basis for future research. It introduces a novel approach to evaluating rock attributes and enhancing the performance of geothermal reservoirs.

START POINT

Through the balance of energies involved in a hydraulic fracture process by applying a constant fluid rate to a material, it will be possible to estimate the fracture energy and the increase in temperature will influence the estimation of this parameter.

GENERAL OBJECTIVES

Develop a new method to estimate fracture energy G_f by hydraulic fracture testing applying a constant fluid rate under conditions of a geothermal reservoir in synthetic rock and rocks samples.

OBJECTIVES

1. Generate new basic scientific knowledge on the phenomenon of fracture in materials such as mortar and rock in a geothermal reservoir condition.
2. Explain the effect of temperature on fracture energy under conditions of a geothermal reservoir.
3. Check the fracture energy values obtained with the proposed method with a method reported in the literature.
4. Calculate the fracture energy with numerical simulation through the parameters obtained from the mortar specimens.
5. Explain the difference of fracture energy values obtained with the different methods used.
6. Demonstrate the contribution of this research to climate change mitigation

References

- 1] Zalasiewicz, J., Williams, M., Steffen, W., Crutzen, P. (2010). The new world of the Anthropocene. *Environ. Sci. Technol.* 44 (7), pp. 2228–2231.
- 2] Kanji, M.A. (2014), Critical issues in soft rocks. *J. Rock Mech. Geotech. Eng.* 6 (3), pp.186–195
- 3] Maurel, O., Rees, T., Matallah, M., De Ferron, A., Chen, W., Laborderie, C., Pijaudier-Cabot, G., Jacques, A., Rey-Bethbeder, F. (2010). Electrohydraulic Shock Wave Generation as a Mean to Increase Intrinsic Permeability of Mortar, Cement and Concrete Research, Vol. 40, pp. 1631-1638.
- 4] USGCRP Melillo, J.M., Richmond, T.C., Yohe, G.W., (Eds.): *Climate Change Impacts in the United States: The Third National Climate Assessment*. U.S. Global Change Research Program
- 5] IPCC.: *Climate Change 2013: The physical science basis contribution of working group I to the fifth assessment report of the intergovernmental panel on climate change*. In: Stocker, T.F., Qin, D., Plattner, D., Tignor, M., Allen, S.K., Boschung, J., Nauels, A., Xia, Y., Bex, V. and Midgley, P.M. (Eds.). Cambridge University Press, Cambridge, United Kingdom and New York, NY, USA (2013)
- 6] Omer, A. M. (2008). Green energies and the environment. *Renewable and sustainable energy reviews*, 12(7), 1789-1821.
- 7] Hasan, R., Mekhilef, S., Seyedmahmoudian, M., Horan, B., & Jana, J. *REN 21*.(2017). *Renewables 2017: Global status report*. *Renewable and Sustainable Energy Reviews*, 72, 1065-1080.
- 8] McCrone, A., Moslener, U., d’Estais, F., Usher, E., & Grüning, C. (2017). *Global trends in renewable energy investment 2017*. Bloomberg New Energy Finance.
- 9] He, Y., Xu, Y., Pang, Y., Tian, H., & Wu, R. (2016). A regulatory policy to promote renewable energy consumption in China: Review and future evolutionary path. *Renewable Energy*, 89, 695-705
- 10] Tester, J. W., Anderson, B. J., Batchelor, A. S., Blackwell, D. D., DiPippo, R., Drake, E. M., ... & Veatch, R. J. (2006). *The future of geothermal energy*. Massachusetts Institute of Technology, 358.
- 11] Geothermal Technologies Office, US DOE. *GeoVision (2019). Harnessing the Heat Beneath Our Feet - Analysis Inputs and Results*. United States. <https://doi.org/10.15121/1572361>
- 12] Holm, A., Blodgett, L., Jennejohn, D., & Gawell, K. (2010). *Geothermal energy: international market update*. Geothermal energy association, 7.
- 13] Khan, M. A., & Truschel, J. (2010). The Geysers geothermal field, an injection success story. *GRC Trans*, 34, pp. 1239-1242.
- 14] Agaton, C. B. (2019). *A Real Options Approach to Renewable and Nuclear Energy Investments in the Philippine (Vol. 71)*. Logos Verlag Berlin GmbH.
- 15] *Installed geothermal energy capacity. (2020, 10 mayo). Our world in Data.* <https://ourworldindata.org/grapher/installed-geothermal-capacity?time=2019>
- 16] Olasolo, P., Juárez, M. C., Morales, M. P., & Liarte, I. A. (2016). Enhanced geothermal systems (EGS): A review. *Renewable and Sustainable Energy Reviews*, 56, pp. 133-144.
- 17] Heidinger, P. (2010). Integral modeling and financial impact of the geothermal situation and power plant at Soultz-sous-Forêts. *Comptes Rendus Geoscience*, 342(7-8), 626-635.
- 18] Lund, J. W. (2008). Development and utilization of geothermal resources. In *Proceedings of ISES World Congress 2007 (Vol. I–Vol. V)* (pp. 87-95). Springer, Berlin, Heidelberg.
- 19] Gutiérrez-Negrin, L., Maya-González, R., & Quijano-León, J. L. (2015). Present situation and perspectives of geothermal in Mexico. In *Proceedings, world geothermal congress* (p. 10).
- 20] Prol-Ledesma, R. M., Carrillo-de la Cruz, J. L., Torres-Verab, M. A., Membrillo-Abadb, A. S., & Espinoza-Ojedac, O. M. (2018). Heat flow map and geothermal resources in Mexico \$ Mapa de flujo de calor y recursos geotérmicos de México. *Terra Digitalis*, 2(2), pp.1-38.
- 21] Davies, J. H., & Davies, D. R. (2010). Earth's surface heat flux. *Solid Earth*, 1(1), pp. 5-24.
- 22] Jones, J. M. R., & Kretschmar, T. G. (2017). The Mexican Center of Innovation in Geothermal Energy, CeMIE-Geo: Challenges and Opportunities. *Procedia Earth and Planetary Science*, 17, pp. 905-908.

- 23] Gutiérrez-Negrín, L. C., Canchola Félix, I., Romo-Jones, J. M., & Quijano-León, J. L. (2020). Geothermal energy in Mexico: update and perspectives. In Proceedings, Proceedings World Geothermal Congress.
- 24] Gutiérrez-Negrín, L., Maya-González, R., & Quijano-León, J. L. (2015). Present situation and perspectives of geothermal in Mexico. In Proceedings World Geothermal Congress 2015 (pp. 19-24).
- 25] Sener (Secretaría de Energía) (2019): PRODESEN 2019-2033, Programa de Desarrollo del Sistema Eléctrico Nacional, 153 p. Available at: <https://www.gob.mx/sener/documentos/prodesen-2019-2033>.
- 26] Sener (Secretaría de Energía) (2018): Mapa de Ruta Tecnológica Usos Directos del Calor Geotérmico, 75 p. Available. https://www.gob.mx/cms/uploads/attachment/file/416191/MRT_UDCG_Final.pdf
- 27] Iglesias, E. R., Torres, R. J., Martínez-Estrella, J. I., & Reyes-Picasso, N. (2010). Summary of the 2010 Assessment of Medium-to Low-Temperature Mexican Geothermal Resources. GRC Transactions, 34, pp. 1155-1159.
- 28] Ministère de l'environnement, Chiffres clés des énergies renouvelables (2016), <http://reseau-chaaleur.cerema.fr/wp-content/uploads/CC-des-energies-renouvelables-edition-2016.pdf> (accessed on 02/26/2018).
- 29] Manzella, A., Allansdottir, A., & Pellizzone, A. (Eds.). (2019). Geothermal energy and society. Springer International Publishing.
- 30] Thermo GIS (2014). GeoELEC Geographical Information System. (www.thermogis.nl/geoelec/ThermoGIS_GEOELEC.html). Accessed at: 11 September 2014
- 31] Bertani, R., & Green, E. (2009, March). Long-term projections of geothermal-electric development in the world. In Proceedings, GeoTHERM Congress, Offenburg/Germany (pp. 5-6).
- 32] Renewables – Global Status Report (2009): REN21 (Renewable Energy Policy Network for the 21st Century). Available at: www.ren21.net
- 33] Change, U. C. (2015). The paris agreement. In United Nations. Available from: <https://unfccc.int/process/conferences/pastconferences/paris-climate-change-conference-november-2015/paris-agreement> [Accessed 5 July 2021]
- 34] World Energy Council: World Energy Resources, Geothermal (2016). www.worldenergy.org/wp-content/uploads/2017/03/WEResources_Geothermal_2016.pdf
- 35] Culligan, P. J., Whittle, A. J., & Mitchell, J. K. (2019). The Role of Geotechnics in Addressing New World Problems. In Geotechnical Fundamentals for Addressing New World Challenges (pp. 1-27). Springer, Cham.
- 36] ISO.: Organización Internacional de Normalización ISO14040 (2006): Gestión Ambiental-Evaluación del ciclo de vida-Principios y marco (2016). www.iso.org/obp/ui/#iso:std:iso:14040:ed-2:v1:es
- 37] Kanji, M.A.: Critical issues in soft rocks. J. Rock Mech. Geotech. Eng. 6 (3), 186-195 (2014)
- 38] US Energy Information Administration (US EIA).: International Energy Outlook (2017). www.eia.gov/pressroom/presentations/mead_91417.pdf, www.eia.gov
- 39] McClure, M. W. (2009). Fracture stimulation in enhanced geothermal systems (Doctoral dissertation, Stanford University).
- 40] Xie, J.; Wang, J.; Liu, X. The role of fracture networks randomness in thermal utilization of enhanced geothermal system. Int. Commun. Heat Mass Transf. 2021, 126, 105414. [CrossRef]
- 41] Zheng, S.; Li, S.; Zhang, D. Fluid and heat flow in enhanced geothermal systems considering fracture geometrical and topological complexities: An extended embedded discrete fracture model. Renew. Energy 2021, 179, 163–178.
- 42] Zhang, X.; Huang, Z.; Lei, Q.; Yao, J.; Gong, L.; Yang, W.; Yan, X.; Li, Y. Improving heat extraction performance of enhanced geothermal systems: Insights from critical fracture network parameter and multi-objective optimization method. Appl. Therm. Eng. 2022, 213, 118671.
- 43] Li, L.; Guo, X.; Zhou, M.; Xiang, G.; Zhang, N.; Wang, Y.; Wang, S.; Pagou, A. The Investigation of Fracture Networks on Heat Extraction Performance for an Enhanced Geothermal System. Energies 2021, 14, 1635.

-
- 44] Liu, J.; Xue, Y.; Zhang, Q.; Wang, H.; Wang, S. Coupled thermo-hydro-mechanical modelling for geothermal doublet system with 3D fractal fracture. *Appl. Therm. Eng.* 2022, 200, 117716.
- 45] Franco A, Vaccaro M. Numerical simulation of geothermal reservoirs for the sustainable design of energy plants: a review. *Renew Sustain Energy Rev* 2014;30(2):987–1002.
- 46] Li M, Lai ACK. Review of analytical models for heat transfer by vertical ground heat exchangers (GHEs): a perspective of time and space scales. *Apply Energy* 2015;151:178–91.
- 47] Song X, Shi Y, Li G, Yang R, Xu Z, Zheng R, et al. Heat extraction performance simulation for various configurations of a downhole heat exchanger geothermal system. *Energy* 2017.
- 48] Lyu Z, Song X, Li G, Hu X, Shi Y, Xu Z. Numerical analysis of characteristics of a single U-tube downhole heat exchanger in the borehole for geothermal wells. *Energy* 2017;125:186–96.
- 49] Zarrella A, Capozza A, Carli MD. Analysis of short helical and double U-tube borehole heat exchangers: a simulation-based comparison. *Appl Energy* 2013;112(12):358–70.
- 50] Go GH, Lee SR, Yoon S, Kang HB. Design of spiral coil PHC energy pile considering effective borehole thermal resistance and groundwater advection effects. *Apply Energy* 2014;125(2):165–78.
- 51] Han C, Yu X. Sensitivity analysis of a vertical geothermal heat pump system. *Apply Energy* 2016; 170:148–60.
- 52] Zhang L, Zhang Q, Huang G. A transient quasi-3D entire time scale line source model for the fluid and ground temperature prediction of vertical ground heat exchangers (GHEs). *Apply Energy* 2016;170:65–75.
- 53] Ping C, Xin L, Yi M, Fang Z. Heat transfer analysis of pile geothermal heat exchangers with spiral coils. *Apply Energy* 2011;88(11):4113–9.
- 54] Man Y, Yang H, Diao N, Liu J, Fang Z. A new model and analytical solutions for borehole and pile ground heat exchangers. *Int J Heat Mass Transf* 2010;53 (13–14):2593–601.
- 55] Kazuo H, Jonathan W-R, Robert JH, Yuichi N. Numerical models of HDR geothermal reservoirs—a review of current thinking and progress. *Geothermics* 1999;28(4–5):507–18.
- 56] O'Sullivan MJ, Pruess K, Lippmann MJ. State of the art of geothermal reservoir simulation. *Geothermics* 2001;30(4):395–429.
- 57] Botros FE, Hassan AE, Reeves DM, Pohll G. On mapping fracture networks onto continuum. *Water Resoures* 2008;44(8):134–43
- 58] Bahrami, B.; Nejati, M.; Ayatollahi, M.R.; Driesner, T. Theory and experiment on true mode II fracturing of rocks. *Eng. Fract. Mech.* 2020, 240, 107314.
- 59] Zhang, H.; Shen, Z.; Xu, L.; Gan, L.; Ma, Z.; Wu, Q.; Liu, D. Experimental investigation on hydraulic fracturing in cement mortar with tensile stress. *Eng. Fract. Mech.* 2022, 259, 108058.
- 60] Wang, B.; Zhang, Q.; Yao, S.; Zeng, F. A semi-analytical mathematical model for the pressure transient analysis of multiple fractured horizontal well with secondary fractures. *J. Pet. Sci. Eng.* 2022, 208, 109444.
- 61] Nguyen, H.T.; Lee, J.H.; Elraies, K.A. A review of PKN-type modeling of hydraulic fractures. *J. Pet. Sci. Eng.* 2020, 195, 107607
- 62] Khristianovich, S.A.; Zheltov, Y.P. Formation of Vertical fractures by means of highly viscous liquid. In 4th World Petroleum Congress; OnePetro: Richardson, TX, USA, 1955; Volume 2, pp. 579–586.
- 63] Settari, A.; Cleary, M. Development and Testing of a Pseudo-Three-Dimensional Model of Hydraulic Fracture Geometry. *SPE Prod. Eng.* 1982, 1, 449–466.
- 64] Advani, S.; Lee, T.; Lee, J. Three-Dimensional Modeling of Hydraulic Fractures in Layered Media: Part Finite Element Formulations. *J. Energy Resour. Technol.-Trans. Asme* 1990, 112, 10–19.
- 65] Chen, Z. Finite element modelling of viscosity-dominated hydraulic fractures. *J. Pet. Sci. Eng.* 2012, 88–89, 136–144.
- 66] Pozos Rivera H. (2013). Técnicas de Fracturamiento Hidráulico en pozos Horizontales de la formación Eagle Ford. UNAM, 145, De Programa de Maestría y Doctorado de Ingeniería.
- 67] Irwin. Analysis of stresses and strains near the end of a crack traversing a plate. *J Appl Mech* 1957; 24:361–4.
-

- 68] Rice JR. A path independent integral and the approximate analysis of strain concentration by notches and cracks. *J Appl Mech* 1968;35 (2):379–86.
- 69] Delaney PT, Pollard DD. Deformation of host rocks and flow of magma during growth of Minette Dikes and Breccia-Bearing Intrusions near Ship Rock. New Mexico: USGS Numbered Series. Professional Paper. U.S. G.P.O; 1981.
- 70] Olson JE. Sublinear scaling of fracture aperture versus length: an exception or the rule? *J Geophys Res: Solid Earth* 2003;108(B9):2413
- 71] Wu K, Olson JE. Simultaneous multi-fracture treatments: fully coupled fluid flow and fracture mechanics for horizontal wells. *SPE J* 2015;20(02):337–46.
- 72] McClure MW. Modeling and Characterization of Hydraulic Stimulation and Induced Seismicity in Geothermal and Shale Gas Reservoirs, Ph.D. Thesis; 2012.
- 73] Shlyapobersky J. On-Site Interactive Hydraulic Fracturing Procedures for Determining the Minimum in Situ Stress from Fracture Closure and Reopening Pressures. *Int J Rock Mech Min Sci Geomech Abstracts* 1989;26(6):541–8.
- 74] Al-Shayea NA, Khan K, Abduljawwad SN. Effects of confining pressure and temperature on mixed-mode (I–II) fracture toughness of a limestone rock. *Int J Rock Mech Min Sci* 2000;37(4):629–43.
- 75] Guo H, Aziz NI, Schmidt LC. Rock fracture-toughness determination by the Brazilian Test. *Engng Geol* 1993;33(3):177–88.
- 76] Schmidt RA, Huddle CW. Effect of confining pressure on fracture toughness of Indiana limestone. *Int J Rock Mech Min Sci Geomech Abstracts* 1977;14(5):289–93.
- 77] Thiercelin M. Fracture toughness under confining pressure using the modified ring test. *Proceedings of American Rock Mechanics Association*. 1987.
- 78] Bungler AP, Detournay E, Jeffrey RG. Crack tip behavior in near-surface fluid-driven fracture experiments. *CR Mec* 2005;333:299–304.
- 79] Groenenboom J, Dam DV. Monitoring hydraulic fracture growth: laboratory experiments. *Geophysics* 2000;65(2):603–11.
- 80] Warpinski NR. Measurement of Width and Pressure in a Propagating Hydraulic Fracture. *Soc Petrol Engng J* 1985;25(01):46–54.
- 81] Yew CH, Weng X (2014). *Mechanics of hydraulic fracturing*. Gulf Professional Publishing, pp. 1–2.
- 82] S. Timoshenko, N.J. Goodier, *Theory of Elasticity*, second ed., McGraw-Hill, New York, 1951
- 83] Yew CH, Weng X (2014). *Mechanics of hydraulic fracturing*. Gulf Professional Publishing, pp. 2–3.
- 84] B.C. Haimson, C. Fairhurst, *Hydraulic Fracturing in Porous Permeable Materials*, *Journal of Petroleum Technical Technology* vol. 25, (1969), pp 811–817.
- 85] B.C. Haimson, C. Fairhurst, *Initiation and Extension of Hydraulic Fractures in Rocks*, *Society of Petroleum Engineers Journal* vol. 21, (1967),pp 310–318.
- 86] W.L. Medlin, L. Masse, *Laboratory Investigation of Fracture Initiation Pressure and Orientation*, in: SPE 6087, presented at the 51st Annual Fall Technical Conference and Exhibition of the SPE and AIME in New Orleans, LA, October, 1976.
- 87] E.B. Becker, G.F. Carey, T.J. Oden, in: *Finite Element, An Introduction*, vol. I, Prentice- Hall, New Jersey, 1981.
- 88] Yew CH, Weng X (2014). *Mechanics of hydraulic fracturing*. Gulf Professional Publishing, pp. 41–42.
- 89] SPE & Packers plus Energy Services. (2010). *Advances in OH Multistage Fracturing Systems- A return to good frac-treatment practices*.
- 90] Pijaudier-Cabot, G., Hajimohammadi, A., Nouailletas, O., La Borderie, C., Padin, A., & Mathieu, J. P. (2022). Determination of the fracture energy of rocks from size effect tests: Application to shales and carbonate rocks. *Engineering Fracture Mechanics*, 271, 108630.
- 91] A.S. Rao, G.A. Rao, *Fracture mechanics of fiber reinforced concrete: an overview*, *International Journal of Engineering Innovations and Research* 3 (4) (2014) 517.

- 92] Rama, J. S. K., Sivakumar, M., Vasana, A., Garg, C., &Walia, S. (2015). A review on studies of fracture parameters of self-compacting concrete. In *Advances in Structural Engineering* (pp. 1705-1716): Springer.
- 93] Naus, D. J., Batson, G. B., &Lott, J. L. (1974). Fracture mechanics of concrete. In *Fracture Mechanics of Ceramics* (pp. 469-482): Springer, Boston, MA.
- 94] Wiederhorn, S. M. (1984). Brittle fracture and toughening mechanisms in ceramics. *Annual Review of Materials Science*, 14 (1), 373-403.
- 95] ASM Handbook Committee. (1987). *Metals Handbook Comprehensive Index*. Asm International
- 96] Hull, D. (1999). *Fractography: observing, measuring, and interpreting fracture surface topography*. Cambridge University Press.
- 97] Griffith, A. A. (1921). VI. The phenomena of rupture and flow in solids. *Philosophical transactions of the royal society of london. Series A, containing papers of a mathematical or physical character*, 221(582-593), 163-198.
- 98] Inglis, C. E. (1913). Stresses in a plate due to the presence of cracks and sharp corners. *Trans Inst Naval Archit*, 55, 219-241.
- 99] Pijaudier-Cabot, G., Hajimohammadi, A., Nouailletas, O., La Borderie, C., Padin, A., & Mathieu, J. P. (2022). Determination of the fracture energy of rocks from size effect tests: Application to shales and carbonate rocks. *Engineering Fracture Mechanics*, 271, 108630.
- 100] Hillerborg, A. 1985. The theoretical basis of a method to determine the fracture energy G_f of concrete. *RILEM Materials and Structures*, 18 (106), pp 291-296.
- 101] Wittmann, F. H., Editor, "Fracture Toughness and Fracture Energy of Concrete," Proceedings, RILEM International Conference on Fracture Mechanics of Concrete, EPFL, (held in Lausanne, 1985), Elsevier, Amsterdam, 1986, 699 pp.
- 102] RILEM Committee 50-FMC, "Determination of the Fracture Energy of Mortar and Concrete by Means of Three-Point Bend Tests on Notched Beams," RILEM Draft Recommendation, *Materials and Structures, Research and Testing (RILEM, Paris)*, V. 18, No. 106, July-Aug. 1985, pp. 285-290.
- 103] Bazant, Z. P., & Pfeiffer, P. A. (1987). Determination of fracture energy from size effect and brittleness number. *ACI Materials Journal*, 84(6), 463-480.
- 104] Mier, J.G.M. van, Vliet, M.R.A. van. 2002. Uniaxial tension test for the determination of fracture parameters of c (ete: state of the art. *Engineering Fracture Mechanics* 69, pp. 235-247.
- 105] 2001, R., Rilem-Committee-TDF-162, Vandewalle, C. L., &main author Stang, H. Test and design methods for steel fiber reinforced concrete, recommendations for uniaxial Tension Test. *Mat & Struc*, 34 (235), 3–6.
- 106] D. Phillips, Z. Binsheng, Direct tension tests on notched and un-notched plain concrete specimens, *Mag. Concr. Res.* 45 (162) (1993) 25–35.
- 107] Khalilpour, S., BaniAsad, E., & Dehestani, M. (2019). A review on concrete fracture energy and effective parameters. *Cement and Concrete research*, 120, 294-321.
- 108] L.J. Malvar, G. Warren, Fracture energy for three-point-bend tests on single-edgenotchedbeams, *Exp. Mech.* 28 (3) (1988) 266–272.
- 109] M. Aliha, A. Razmi, A. Mansourian, The influence of natural and synthetic fiberson low temperature mixed mode I+ II fracture behavior of warm mix asphalt(WMA) materials, *Eng. Fract. Mech.* 182 (2017) 322–336.
- 110] S. Pirmohammad, H. Khoramishad, M. Ayatollahi, Effects of asphalt concrete characteristics on cohesive zone model parameters of hot mix asphalt mixtures, *Can. J. Civ. Eng.* 43 (3) (2015) 226–232.
- 111] Y.-R. Kim, Cohesive zone model to predict fracture in bituminous materials and asphaltic pavements: state-of-the-art review, *International Journal of Pavement Engineering* 12 (4) (2011) 343–356.

- 112] UNI (Ente Nazionale Italiano di Unificazione), Concrete Reinforced With Steel Fiber Test Method for the Determination of Early Crack Strength and Ductility Indexes. UNI 11039-2:2003, National Italian Unification Centre, Milan, Italy, 2003.
- 113] ANONGBA, P. (2015). A Theory of the Fracture of Rectangular Bars Bent by Terminal Transverse Load and Couple.
- 114] F. Mujika, On the difference between flexural moduli obtained by three-point and four-point bending tests, *Polym. Test.* 25 (2) (2006) 214–220.
- 115] F. Bencardino, L. Rizzuti, G. Spadea, R.N. Swamy, Implications of test methodology on post-cracking and fracture behaviour of steel fibre reinforced concrete, *Compos. Part B* 46 (2013) 31–38.
- 116] F. Wittmann, K. Rokugo, E. Brühwiler, H. Mihashi, P. Simonin, Fracture energy and strain softening of concrete as determined by means of compact tension specimens, *Mater. Struct.* 21 (1) (1988) 21–32.
- 117] B. Cotterell, On fracture path stability in the compact tension test, *Int. J. Fract. Mech.* 6 (2) (1970) 189–192.
- 118] B. Neale, An investigation into the effect of thickness on the fracture behaviour of compact tension specimens, *Int. J. Fract.* 14 (2) (1978) 203–212.
- 119] H. Kim, M.P. Wagoner, W.G. Buttlar, Simulation of fracture behavior in asphalt concrete using a heterogeneous cohesive zone discrete element model, *J. Mater. Civ. Eng.* 20 (8) (2008) 552–563.
- 120] Kuai, H., Lee, H., Zi, G., & Mun, S. (2009). Application of generalized J-integral to crack propagation modeling of asphalt concrete under repeated loading. *Transportation Research Record: Journal of the Transportation Research Board* (2127), 72-81.
- 121] A. Collop, A. Sewell, N. Thom, Laboratory assessment of the resistance to crack propagation in high-stiffness asphaltic materials, *Proceedings of the Institution of Mechanical Engineers, Part L: Journal of Materials: Design and Applications* 218 (1) (2004) 55–66.
- 122] Kim, H., & Buttlar, W. G. (2005). Micromechanical fracture modeling of asphalt mixture using the discrete element method. In *Advances in Pavement Engineering* (pp. 1-15).
- 123] T. Holušová, S. Seitl, & Fernández-Canteli, A., Numerical support of experimental compact tension test on concrete cylindrical specimens, *Transactions of the VŠB–Technical University of Ostrava, Civil Engineering Series* 13 (2) (2013) 31–40.
- 124] H. Linsbauer, E. Tschegg, Fracture energy determination of concrete with cube shaped specimens, *Zement und Beton* 31 (1) (1986) 38–40.
- 125] E. Brühwiler, F. Wittmann, The wedge splitting test, a new method of performing stable fracture mechanics tests, *Eng. Fract. Mech.* 35 (1–3) (1990) 117–125.
- 126] Flansbjer, M., Löfgren, I., & Forbes Olesen, J. (2005). The WST-method for Fracture Testing of Fibre-reinforced Concrete. In.
- 127] K. Duan, X. Hu, F.H. Wittmann, Boundary effect on concrete fracture and non constant fracture energy distribution, *Eng. Fract. Mech.* 70 (16) (2003) 2257–2268.
- 128] H. Abdalla, B.L. Karihaloo, Determination of size-independent specific fracture energy of concrete from three point-bend and wedge splitting tests, *Mag. Concr. Res.* 55 (2) (2003) 133–141.
- 129] S. Teng, Y. Liu, T.Y.D. Lim, Determination of fracture energy of ultra high strength concrete, *Eng. Fract. Mech.* 131 (2014) 602–615.
- 130] Grassl P, Gregoire D, Rojas Solano L, Pijaudier-Cabot G. Meso-scale modelling of the size effect on the fracture process zone of concrete. *Int J Solids Struct* 2012;49(13):1818–27.
- 131] Lefort V, Nouailletas O, Grégoire D, Pijaudier-Cabot G. Lattice Modelling of hydraulic fracture: theoretical validation and interactions with cohesive joints. *Eng Fract Mech* 2020;235:107178.
- 132] K. Yu, J. Yu, Z. Lu, Q. Chen, Determination of the softening curve and fracture toughness of high-strength concrete exposed to high temperature, *Eng. Fract. Mech.* 149 (2015) 156–169.
- 133] C.V. Nielsen, High temperature effects on tensile softening behaviour of concrete, In *Symposium on Nordic Concrete Research*, Helsingor, 2002.

- 134] B. Zhang, N. Bicanic, Fracture energy of high-performance concrete at high temperatures up to 450 C: the effects of heating temperatures and testing conditions (hot and cold), *Mag. Concr. Res.* 58 (5) (2006) 277–288.
- 135] Bažant, Z. P., & Prat, P. C. (1988). Effect of temperature and humidity on fracture energy. *ACI Materials Journal*.
- 136] B. Akcay, A.S. Agar-Ozbek, F. Bayramov, H.N. Atahan, C. Sengul, M.A. Tasdemir, Interpretation of aggregate volume fraction effects on fracture behavior of concrete, *Constr. Build. Mater.* 28 (1) (2012) 437–443.
- 137] F. Wittmann, K. Rokugo, E. Brühwiler, H. Mihashi, P. Simonin, Fracture energy and strain softening of concrete as determined by means of compact tension specimens, *Mater. Struct.* 21 (1) (1988) 21–32.
- 138] M.H. Beygi, M.T. Kazemi, I.M. Nikbin, J.V. Amiri, S. Rabbanifar, E. Rahmani, The influence of coarse aggregate size and volume on the fracture behavior and brittleness of self-compacting concrete, *Cem. Concr. Res.* 66 (2014) 75–90.
- 139] A. Yan, K.-R. Wu, D. Zhang, W. Yao, Effect of fracture path on the fracture energy of high-strength concrete, *Cem. Concr. Res.* 31 (11) (2001) 1601–1606.
- 140] M.A. Issa, M.A. Issa, M.S. Islam, A. Chudnovsky, Size effects in concrete fracture—part II: analysis of test results, *Int. J. Fract.* 102 (1) (2000) 25–42.
- 141] Kallel, H., Carré, H., Laborderie, C., Masson, B., & Tran, N. C. (2018). Evolution of mechanical properties of concrete with temperature and humidity at high temperatures. *Cement and Concrete Composites*, 91, 59-66.
- 142] C. La Borderie, Phenomenes unilateraux dans un materiau endommageable : modelisation et application a l'analyse de structures en beton, Ph.D. thesis (1991).
- 143] Irwin, G. R. (1957). Analysis of stresses and strains near the end of a crack traversing a plate.
- 144] Gdoutos, E. E. (2005). *Solid Mechanics and its Applications-Fracture Mechanics*. The Netherlands: Springer.
- 145] Swedlow, J. L., Williams, M. L., & Yang, W. H. (1966). Elasto-plastic stresses and strains in cracked plates (Elasto-plastic stresses and strains in cracked plates analyzed by numerical method, noting stress singularities and stress-strain fields, pp. 259-282.
- 146] Benzly, S. (1974). Representation of singularities with isoparametric finite elements. *Int. J. Num. Meth. Engng.* pp.537-545
- 147] Bažant, Z.P., 2002. Concrete fracture models: testing and practice. *Eng. Fract. Mech.* 69, 165–205. [https://doi.org/10.1016/S0013-7944\(01\)00084-4](https://doi.org/10.1016/S0013-7944(01)00084-4)
- 148] Bazant, Z.P., Kazemi, M.T., 1990. Size Effect in Fracture of Ceramics and Its Use To Determine Fracture Energy and Effective Process Zone Length. *J. Am. Ceram. Soc.* 73, 1841–1853. <https://doi.org/10.1111/j.1151-2916.1990.tb05233.x>
- 149] Kuna, M. (2013). *Finite elements in fracture mechanics. Solid Mechanics and Its Applications*, 201, 153-192.
- 150] Oda M. Modern developments in rock structure characterization. *Comprehensive Rock Eng* 1993:185–200. [https://doi.org/10.1016/0148-9062\(94\)90481-2](https://doi.org/10.1016/0148-9062(94)90481-2).
- 151] Hong T, Kempka T, Neng-Xiong X. Physical properties of sandstones after high temperature treatment. *Rock Mech Rock Eng* 2012;45:1113–7.
- 152] Peng, K., Lv, H., Zou, Q., Wen, Z., & Zhang, Y. (2020). Evolutionary characteristics of mode-I fracture toughness and fracture energy in granite from different burial depths under high-temperature effect. *Engineering Fracture Mechanics*, 239, 107306.
- 153] Qi, W., Yun, X., Xiaoquan, W., Tengfei, W., & Zhang, S. (2012). Volume fracturing technology of unconventional reservoirs: Connotation, design optimization and implementation. *Petroleum Exploration and Development*, 39(3), 377-384.
-

CHAPTER III METHODOLOGY

3.0 Generalities

In this chapter, we will outline the methodology employed to obtain the results for the three stages of this research project: 1) mechanical and hydro-mechanical characterization of synthetic rocks, 2) mechanical and hydro-mechanical characterization of natural rocks, and 3) verification of fracture energy values using both traditional methods and finite element analysis. For the fabrication of synthetic rock specimens, materials were procured and prepared in adherence to ASTM standards to produce cementitious materials. Furthermore, rocks were collected from the study area to conduct mechanical and hydromechanical characterization tests. These comprehensive tests encompassed the following aspects:

- a) Estimation of elastic properties, including Young's modulus (E) and Poisson's ratio (θ).
- b) Estimation of compressive strength (σ_c).
- c) Estimation of fracture toughness.
- d) Estimation of the coefficient of permeability and fracture energy at room and high temperature.

Subsequently, the obtained fracture energy results were compared with those obtained through traditional methods described in the literature, followed by verification using finite element analysis.

3.1 Study area and general methodology

The study area is situated between of the state of Queretaro and Guanajuato, Mexico, and encompasses a medium-enthalpy geothermal reservoir characterized by a temperature of approximately 150°C (refer to Figure 29). The maximum temperature in the zone is at a depth of 1.5 km. During the fieldwork, a systematic collection of surface rocks was conducted, resulting in the acquisition of 678 kg of representative rock samples that are indicative of the geological composition of the geothermal reservoir (refer to Figure 30). The collected rocks, including limestone, andesite, and basalt, were subsequently utilized for the mechanical and hydromechanical characterization aimed at simulating the behavior of rocks within the geothermal reservoir.

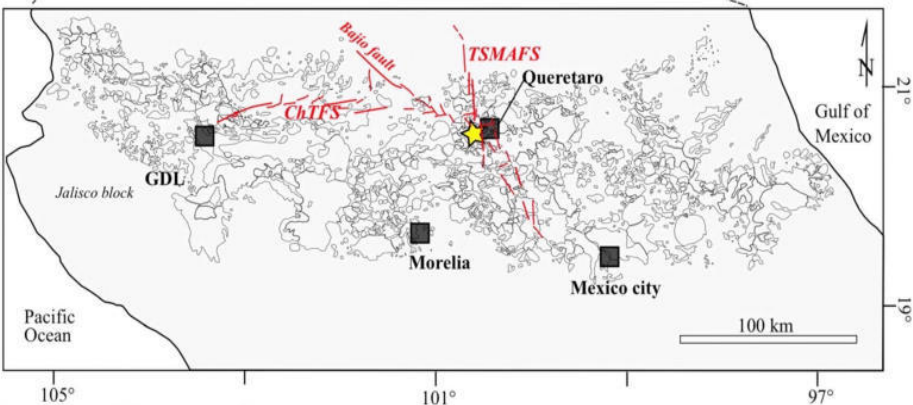


Figure 29. Location of the collection area of rocks representative of a geothermal reservoir

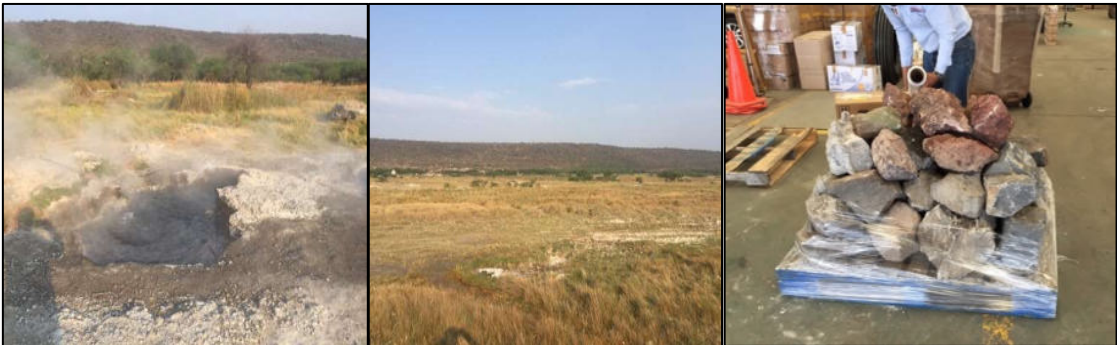
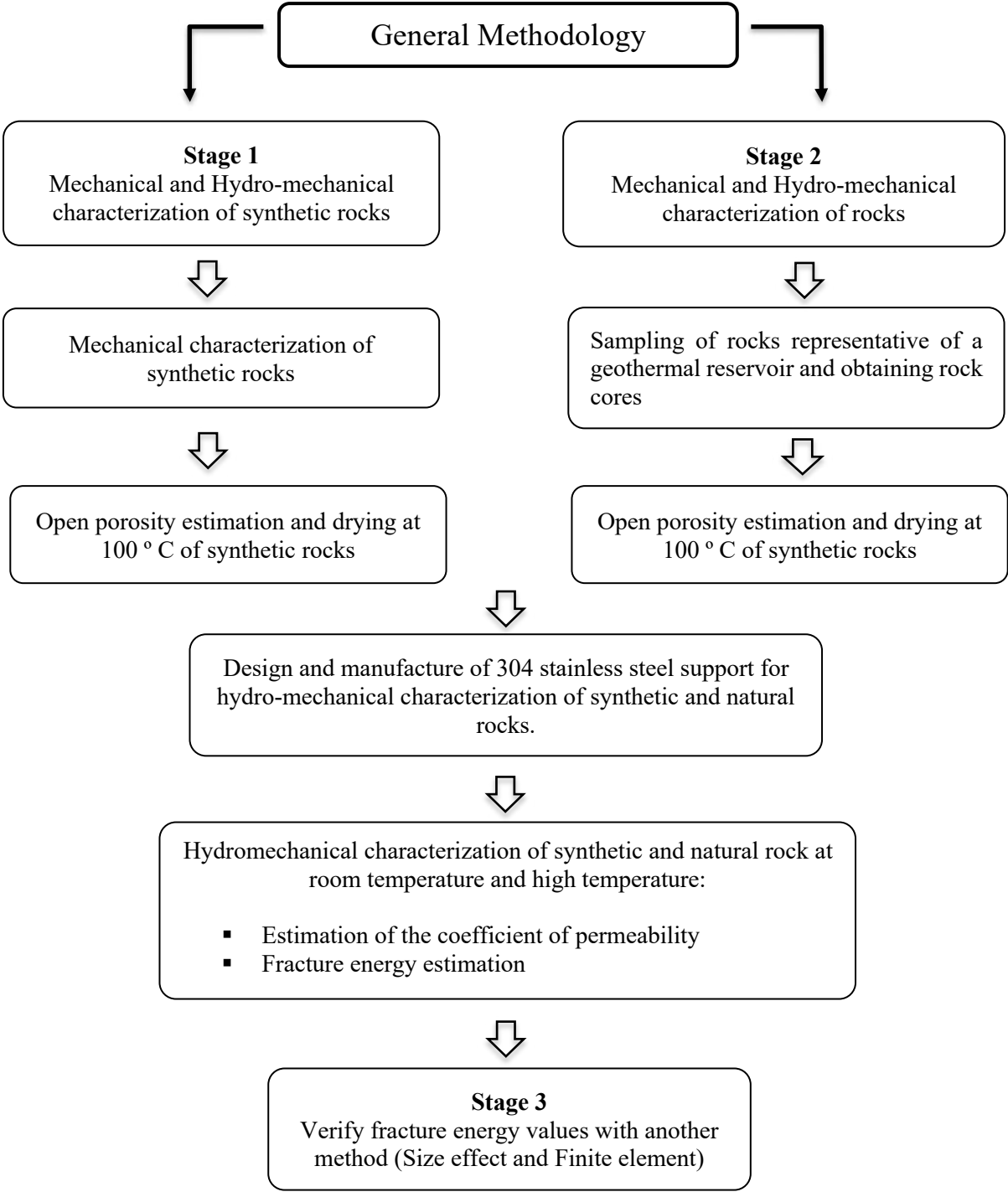


Figure 30. Area of the collection of rocks representative of a geothermal reservoir

3.2 Summary of the methodology

The experimental methodology is divided into three stages and the following diagram describes each stage in detail.



The methodology was designed considering the idea of presenting an experimental method that allows estimating the fracture energy directly in hydraulic fracture tests, by an analog model of an "EGS" at a laboratory scale to emulate an actual geothermal reservoir at a laboratory scale. Figure 31 shows an illustration that explains our analogical model built in the laboratory. This procedure is based on energy conservation and on the fracture area that is created by hydraulic fracturing, which can be considered a method that aims to provide quickly fracture energy.

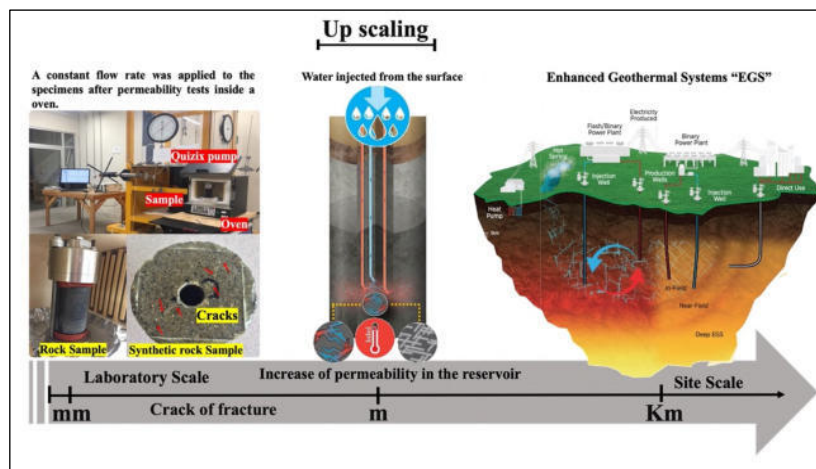


Figure 31. Analog model of an “EGS” at the laboratory scale used to emulate a real geothermal reservoir.

To construct the analog model, we considered the rocks found in the study area, including limestone, andesite rock, basalt, and other relevant rock types. The study area had been previously investigated by Dora Carreon-Freyre in 2005 [1]. In Figure 32, you can see the stratigraphic profile of the soil. The collected rocks were then utilized in the mechanical and hydromechanical characterization stage, aiming to represent the properties of rocks typically found in a geothermal reservoir.

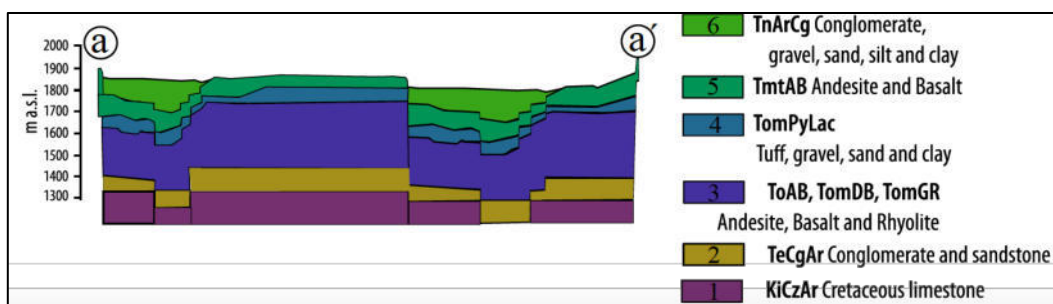


Figure 32. Stratigraphic profile of the study area ^[1]

3.3 Preparation of natural and synthetic rock samples

After the rocks were collected in Queretaro, México, cores of rock with a dimensions of 11.30 cm x 5.30 cm were obtained horizontally and vertically using a GCTS nucleator and cores were obtained. Figure 33 shows these stages.



Figure 33. Rock collection and obtaining cores.

Considering the method discussed to calculate the fracture energy is developed at the laboratory scale and we need many samples for developing the new technique, in the laboratories, it is common to use synthetic rocks such as mortar and concrete to create new experimental techniques [2,3]. Mei et al. (2017) has reported the successful use of synthetic rocks made of a mixture of cement, gypsum, sand, and water, and the validity of this approach has been recently reviewed [4,5] Therefore, we are going to follow the same idea here and consider first mortar specimens in the tests, and then, fracture of rocks samples will be investigated. So, Cylindrical samples with outer and inner diameter of 53 mm and 10 mm respectively, and height 105 mm were prepared (see figure 34). Mortar mix was prepared using CPC 30 R cement and fine aggregate with a maximum particle size of 1.40mm and W/C ratio of 0.45, the mortar samples were cured for 28 days.



Figure 34. Preparation of synthetic rock specimens

3.4 Open porosity and drying of rocks and synthetic rocks samples

The open porosity of the mortar specimens was determined in accordance with the ASTM C-642 standard [6]. The synthetic rocks samples were heated to a temperature of 80° C (see figure 35). With the purpose of eliminating any humidity inside the samples, they were dried following the same procedure as for the mechanical tests before starting the permeability tests. To avoid further contact with humidity, the specimens were placed in hermetic bags filled with oil, the fluid that is going to be used for measuring permeability.



Figure 35. Drying and open porosity test on synthetic and limestone specimens

3.5 Mechanical characterization of rocks and synthetic rock samples

To measure the elastic properties of the material and the compressive strength, the specimens were tested in uniaxial compression using a GCTS RTR 2000 triaxial machine. Subsequently, Splitting Tensile Strength Test (Brazilian) were performed to obtain the tensile strength of mortar specimen (See figures 36 and 37).

In addition, the following characterizations were made:

- a) Estimation of elastic properties (Young modulus E , Poisson's ratio ν),
- b) Estimation of compressive strength σ_c and
- c) Estimation of fracture toughness



Figure 36. Mechanical characterization of synthetic rocks

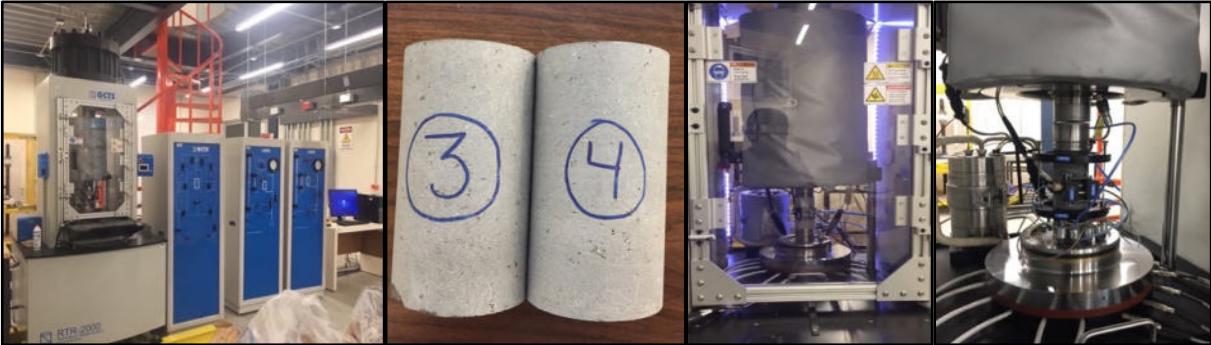


Figure 37. Mechanical characterization of rocks

3.6 Hydro-mechanical characterization of rocks and synthetic rock samples

The hydro-mechanical characterization was performed at room temperature (**21° C**) and high temperature (**100° C**). Steel device was designed and manufactured to perform the permeability and hydraulic fracture tests. This device was connected to a pump (Quizix model Q-5020-HC), a constant flow rate was applied to the specimens and for the tests with high temperature (**100 ° C**) Vulcan Oven 3-550 was used. In figure 38, a cross-section diagram of the operation of the steel device during the hydro-mechanical characterization can be seen.

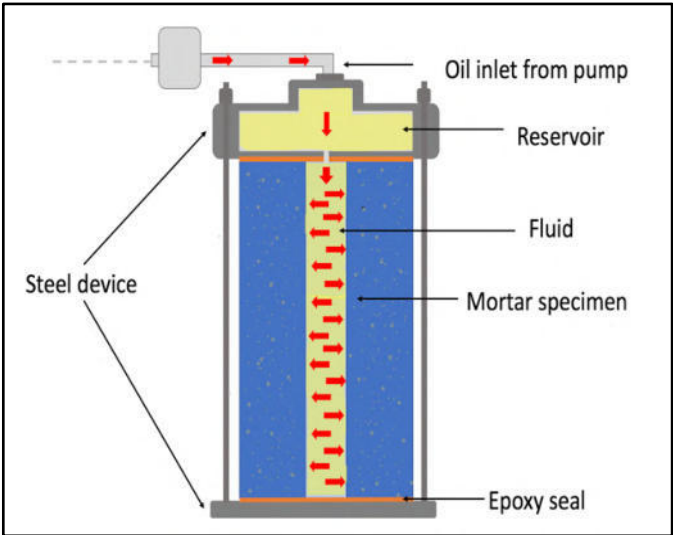


Figure 38. Cross-section of a typical test specimen

3.6.1 Permeability test at room temperature and high temperature

The permeability of the material was determined by injecting pressurized fluid into the hollow cylinder using a pump (Quizix model Q-5020-HC), as depicted in figure 39. Mobile DTE 25 oil was used as the injected fluid due to its flash point of 232°C. Since the high temperature tests reached a maximum of 100°C, we ensured safety by staying below the flash point limit. In the case of extremely high temperature tests, a fracturing fluid with a higher flash point could be employed if higher temperatures are intended. Then, the specimens were placed in the mechanical set-up (See figure 40), a low axial load of 0.245 MPa being applied to prevent leakage, the fluid was injected at pressure levels of 600, 800, 1000, 1400 and 2000 KPa and the flow rate was measured, upon reaching a steady state. The fluid flow rate was estimated by the Pump Works software by using the inner area of its cylinders and the speed of the pistons.

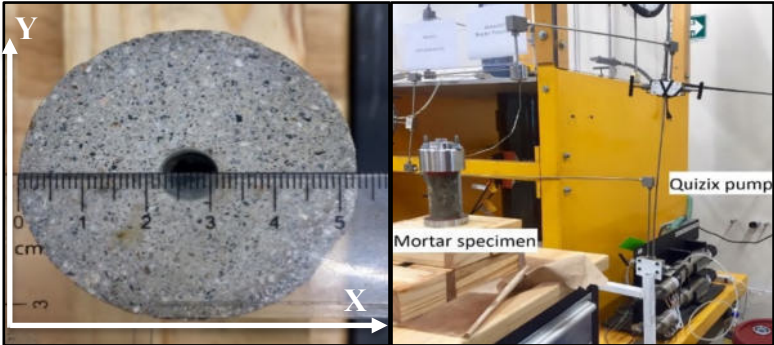


Figure 39. Injection system for permeability tests.

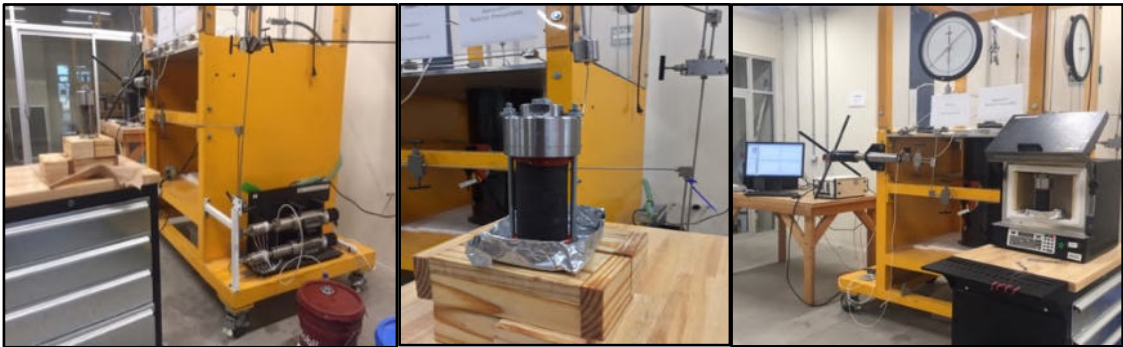


Figure 40. Hydro-mechanical characterization of the synthetic rock specimens.

3.6.2 Hydraulic Fracture test

After conducting the permeability tests using the same specimens, hydraulic fracture tests were performed on hollow cylindrical mortar specimens. Fluid is injected in the hollow cylinder under fixed fluid flow conditions and the pressure is increased until a maximum corresponding to the onset of fracture is reached. In the literature, several set-ups for performing hydraulic fracture tests can be found, mostly on prismatic specimens (see e.g., Goncalves de Silva and Einstein (2018) [7], Zhou et al. (2008) [8], but also on cylindrical specimens (see e.g. Wanniarachchi et al. 2018) [9]. While tests on prismatic cylinders allow to apply lateral confinement stresses that are not equal, which is more representative of actual reservoir conditions, tests on cylinders are simpler to operate and may use a triaxial testing machine if the effect of triaxial states of stresses prior to fracture needs to be investigated. It is this type of geometry, placed in a uniaxial testing device that has been implemented in the present contribution.

In figure 41, it is possible to see the hydraulic fracture tests at room and high temperature, where it was obtained the evolution of hydro-mechanical properties with confinement pressure at room and high temperature in synthetic rock and rock representative of the geothermal reservoir.



Figure 41. Hydro-mechanical characterization of rock representative in geothermal reservoir.

In summary, the hydraulic fracture tests applied a constant flow to the samples. Figure 42 shows a general scheme of the test process in the pump (Quizix model Q-5020-HC) until reaching the mortar or rock samples for the permeability and hydraulic fracture tests. For example, point 1 shows the beginning of the test, which corresponds to the Quizix pump used where the fluid is transported to point 2, where the test specimen is, to break the specimen and come out as potential energy.

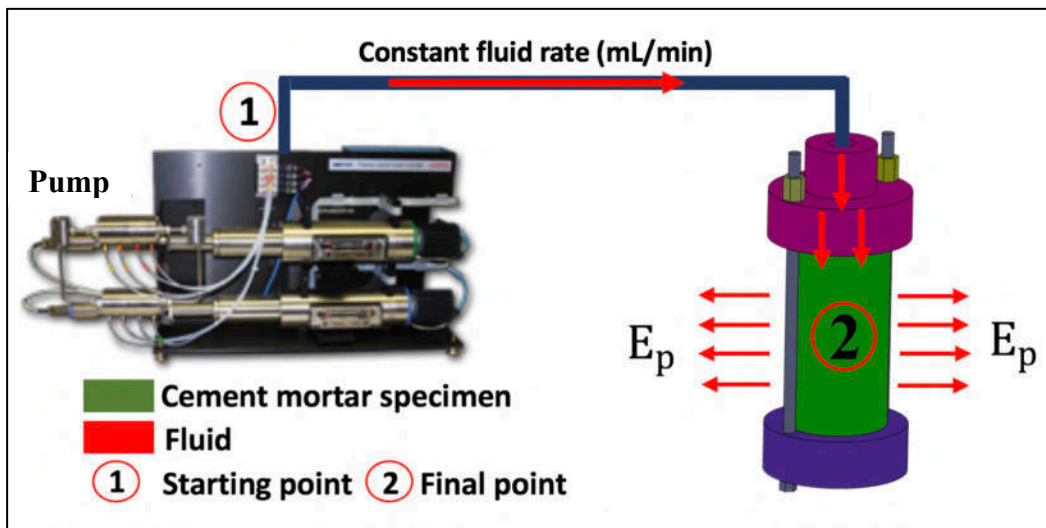


Figure 42. Hydraulic fracture test system for specimens

The process of fracture energy calculation for the system presented in Figure 42 is explained below. To estimate the fracture energy, the different energies involved during the hydraulic fracture tests were considered. We will consider that the fluid is incompressible, with constant viscosity and density, and use Bernoulli's equation:

$$E_{K1} + E_{P1} + E_{z1} = E_{K2} + E_{P2} + E_{z2} + E_{p1-2} \quad (57)$$

Where: E_K : Kinetic energy, E_P : Pressure energy, E_z : Potential energy, E_{p1-2} : Energy for losses, E_μ : Energy dissipated by viscosity, G_f : Fracture energy. During the hydraulic fracture tests performed in the laboratory, the kinetic and potential (fluid lift) energy of the fluid was small compared to the energy related to fluid pressurization and their contributions are disregarded (but should be considered in the field). Therefore, the energy supplied to the specimen comes mainly from the energy supplied by the pump to the fluid, and is denoted as W :

$$W = (p_a A)(Q/A) = p_a \times Q \quad (58)$$

where W is the pump power, P_a is the fluid pressure at the inner bore of the mortar or rock cylinder, Q is the fluid rate and A is the cross-sectional area through which the fluid passes. At a time, interval dt , the energy provided by the pump is dE and defined as:

$$dE = Wdt. \quad (59)$$

Since the tests have been performed with a constant flow rate, the total amount of energy provided by the pump will be:

$$E(t) = \int_0^t Wdt = Q \int_0^t p_a dt, \quad (60)$$

which means that this energy can be easily obtained by integrating the pressure plots, as shown in figure 62 (Chapter of results and discussion). According to the conservation of energy, the energy supplied by the pump during the complete hydraulic fracturing process, at the end of the test corresponding to time t_f , must have been completely dissipated due to the viscosity of the fluid E_μ , or due to the fracture of the specimen E_f :

$$E(t_f) = E_\mu + E_f \quad (61)$$

To isolate the energy consumed during the fracture of the specimen, we now need to estimate the energy dissipated by the viscosity, i.e., the dissipation due to the Darcy flow inside the specimen, so:

$$E_\mu = \int_0^{t_f} P(t) \times Q(t) dt \quad (62)$$

where pressure and fluid flow are now related by Darcy's law (See equation 76). Over the specimen, Darcy's law translates into a linear relationship between pressure and fluid flow (which is kept constant) as illustrated in Figure 59 (Chapter of results and discussion). Therefore, this integral can be easily evaluated: for a typical fluid flow in the range of 0.1 mL/min, integrating over the duration of the test (2000-3000 seconds) using the slope obtained in Figure 56, an energy of the order of 0.01 Joules is obtained. In the case of temperature variations (e.g., from 20° to 100° C), the viscosity may change by an order of magnitude, but this energy will remain small or negligible.

Compared to the energy expected to dissipate during fracture, $E\mu$ is negligible. Therefore, the measured fracture energy does not depend on the properties of the pressure fluid in the present case.

$$K = \frac{Q\mu \ln(b/a)}{2\pi H(p_i - p_e)} \quad (63)$$

This would not be the case if the energy dissipation due to fluid flow in the various devices or in the specimen due to Darcy flow is not negligible, or if the fluid reacts with the rock. Therefore, a correction of the energy balance would be necessary to arrive at an intrinsic estimate of the fracture energy. In the present experiments, Equation 61 gives the energy dissipated due to fracture as a function of the energy supplied by the pump. To obtain the fracture energy, we must divide E_f by the fracture area created during the test, A_f to be obtained experimentally. Therefore:

$$G_f = \frac{Q \int_0^t p_a dt}{A_f} \quad (64)$$

Therefore, the fracture area created at the end of the hydraulic fracture test can be approximated as:

$$A_f = n(D_o - D_i)h, \quad (65)$$

where D_o and D_i are the outside and inside diameters of the specimen, h is the height of the specimen and n is the number of pieces in which the specimen is fractured. All specimens tested in this study were fractured in two parts and four fracture surfaces are generated, therefore, $n = 4$. Finally, the fracture energy estimation was obtained with equation 64, in mortar and rock specimens. The integrals of the pressure plots in figure 62 were calculated according to the trapezoidal rule and the results.

3.7 Verification of the method for estimating fracture energy

With the objective of verifying the fracture energy values obtained with the proposed method and with the three-point test, finite element simulations were performed. A comparison of the three methods used is shown in the next scheme in the figure 43.

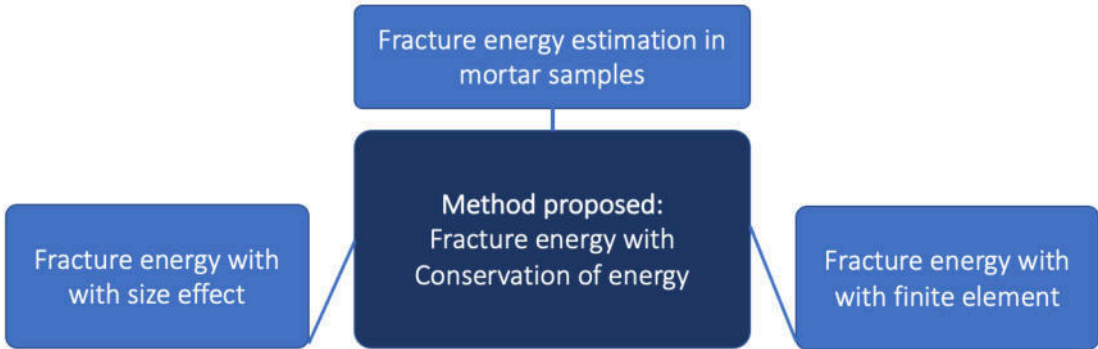


Figure 43. Methods used to obtain fracture energy.

By comparing the fracture energy results obtained using the proposed method with those obtained from a traditional method reported in the literature and with finite element analysis, we will be able to determine the differences between each method and establish a margin of error.

3.7.1 Mortar sample for bending test

To verify the fracture energy values obtained in the first stage, mortar samples of different diameters (20 cm, 10 cm, and 5 cm) were manufactured using the same mortar mix used in the first stage, to perform the bending test. A fine aggregate with a particle size of 1.40 mm and an A/C of 0.45 was used and plastic molds made of PVC pipes were used. The specimens were then unmolded and cured for 28 days, as shown in figure 44. Then, using the same type of mix, more mortar specimens were made, but in different years and with other diameters, for example: (10 cm, 5 cm, 2.5 cm). The specimens were made in different periods to determine the fracture energy and compare the results (see table 2).

Table 2. Mortar mixes

Mortar samples			
Mix	Diameters (cm)	Year of manufacture	Days of curing
1	2.5, 5, 10	2021	28
2	5, 10, 20	2022	



Figure 44. Preparation of mortar specimens

3.7.2 Cutting of mortar samples

To utilize the new mortar specimens for the bending test and determine the fracture energy and size effect, the specimens were cut into half disks with notches, corresponding to their respective diameters (Figure 45). The length of the notch was calculated using the following formula, with the provided example specifically illustrating the calculation for a specimen with a diameter of 20 cm. Here, R represents the radius of the specimen, D represents the diameter, and a represents the desired length of the notch. For instance, to determine the length of the notch for a mortar specimen with a diameter of 20 cm.

$$R = \frac{D}{2}$$

$$R = 20/2$$

$$\underline{R = 10 \text{ cm}}$$

$$a = 0.3R$$

$$a = 0.3 (10 \text{ cm})$$

$$\underline{a = 3.0 \text{ cm}}$$



Figure 45. Notch of the Mortar samples cut in half circle.

After cutting all the mortar specimens, those with the best notches were selected for the three-point test. Table 3 shows the selected specimens, having a notch close to the ideal, since the manual cutting did not allow to obtain an exact length, but all the specimens were cut with a width of 40 mm.

Table 3. Dimensions in mortar specimens.

Mortar sample	Diameter (mm)	B (mm)	Notch obtained (cm)	Ideal Notch (cm)
1	200	40	2.67	2.88
6			2.82	
7			2.70	
2	100	40	1.62	1.57
3			1.60	
6			1.58	
15			0.740	
16	50	40	0.780	0.765
17			0.775	

3.7.3 Three-point bending test

To determine fracture toughness, several methods suggested in the literature can be used: Chevron Bend specimens and Short Rod Specimens [10]. In addition, there are other methods to measure fracture toughness using circular specimens, such as Cracked Chevron notched Brazilian Disk, Semi-Circular Bend, Cracked Brazilian Disc Test, and specimens with chevron notches [11]. Also, the International Society for Rock Mechanics and Rock Engineering (ISRM) [12] recommends two methods with three types of core-based specimens to determine the fracture toughness of rocks, i.e., Chevron Bend and Short Rod specimens and Cracked Chevron-Notched Brazilian Disk specimens [13]. Considering that our study is based on loading mode I, the semicircular bending specimen with a notch in the center was used and then tests were performed on mortar specimens with different diameters, as shown in Figures 48 to 50. After cutting the specimens, sensors (see figure 49) were placed at the bottom of each specimen to measure the displacement (CMOD) during the three-point bend test in the ZWICK 250 tensile machine (see figure 47) with displacement controlled. The maximum stress of each specimen was obtained to later calculate the fracture energy and the size effect.

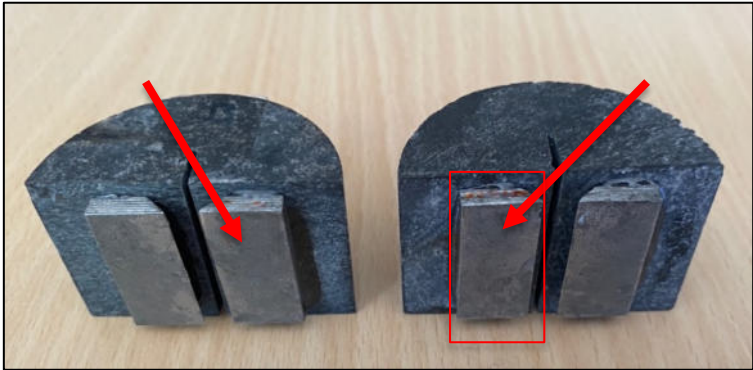


Figure 46. Sensors to measure displacement during the test.



Figure 47. Machine ZWICK 250

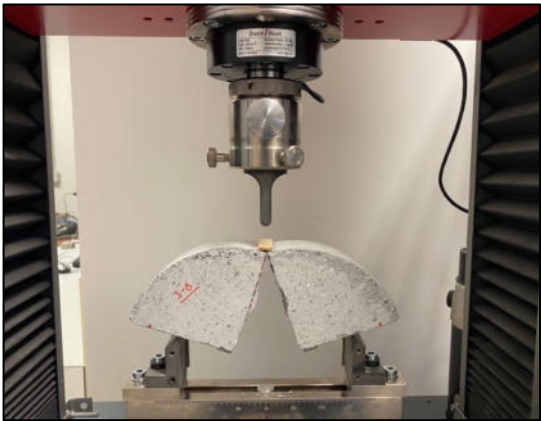


Figure 48. Mortar sample of 20 cm of diameter



Figure 49. Mortar sample of 10 cm of diameter



Figure 50. Mortar sample of 5 cm of diameter

3.7.4 Obtaining the Young's modulus of new mortar samples

Considering the new mortar specimens were made with a considerable time difference but with the same material and mix formulation, Young's Modulus was determined again (See figure 51) with a non-destructive test. This parameter is necessary for the numerical code to obtain the simulations and determine the fracture energy values. The test was performed in accordance with ASTM C469 [14], and the objective was to obtain the elastic behavior of the material for later use in the finite element simulation.



Figure 51. Mortar specimen during the test to calculate the young modulus.

3.7.5 Finite element

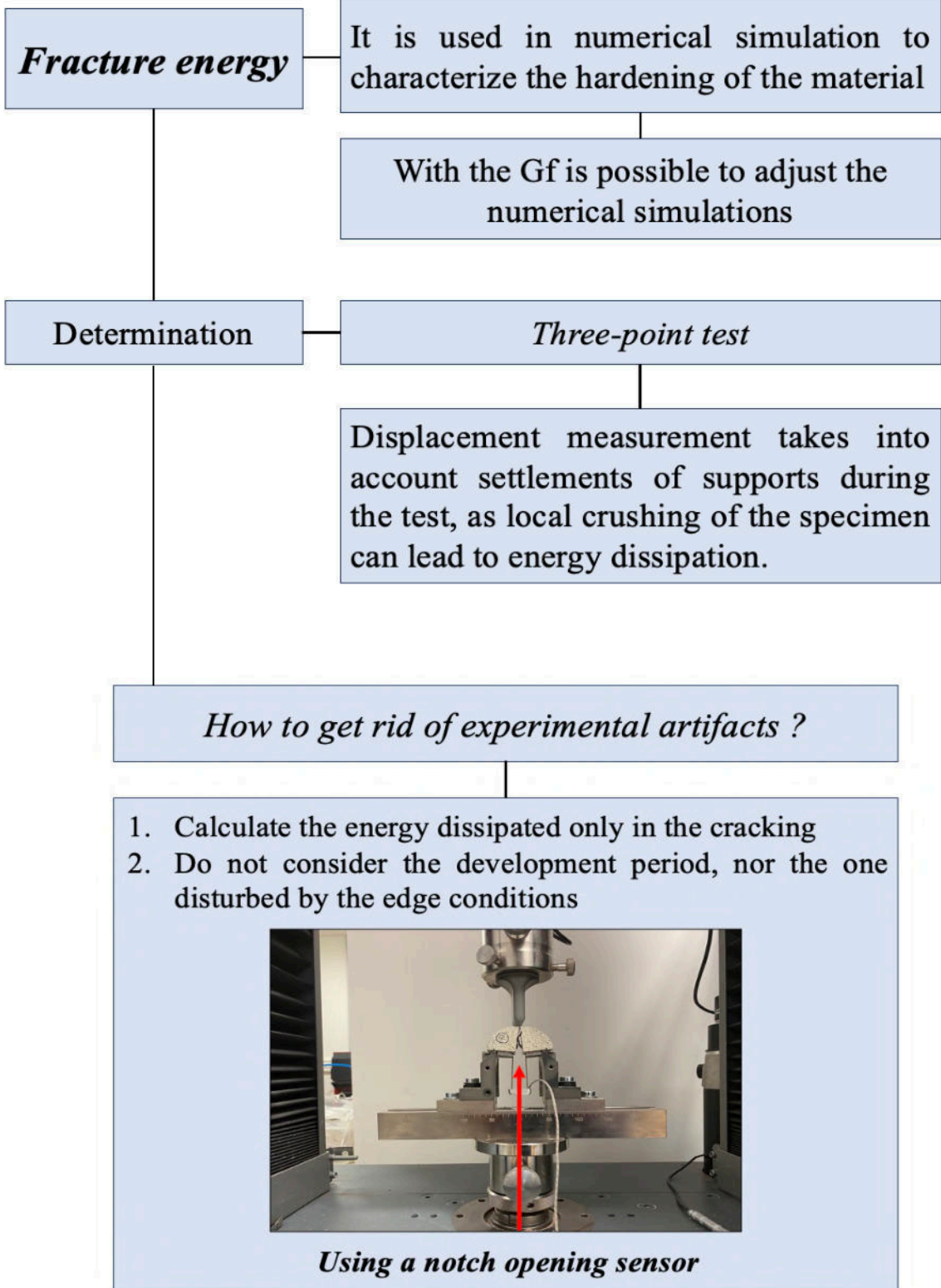
Previously, tests were conducted to determine the fracture energy values of mortar specimens. Using the parameters obtained from these tests, simulations were then performed using a numerical code to calculate the fracture energy once again. This was done to validate the obtained values using both the existing method described in the literature and the proposed method based on energy conservation.

The following provides a general description of the computer code utilized for calculating the fracture energy and Young's modulus. This section involved defining the geometry of the specimen and specifying certain properties, such as Young's modulus, Poisson's ratio, fracture energy, length and width of the notch and radio of the sample. Additionally, the properties of the steel base on which the specimen was placed were also considered. For example, for the 52.5 mm diameter mortar specimen, we used the next parameters in CASTEM.

- YGB=19.E9; NUB=0.2;
- YGA=2.1E11;
- NUA=0.28;
- R1=52.5E-3/2.;
- Th_notch=0.5E-3;
- W_notch=6.69E-3;
- EP1=40.0E-3;
- A1=R1-(41.6e-3/2);
- A_FRAC=EP1*(R1-W_notch);
- th_calle=5.e-3;
- ep_calle=4.E-3;
- b_calle=1.e-2;

The geometry of all specimens was subsequently determined, considering the presence of a notch at the center. While a conceptual map illustrating part of the procedure is provided below, the complete procedure is presented in an appendix. As an important point in the compliance, we took the values that are between 10% and 25% of the maximum load, and then we performed a linear regression and found the value at the origin to determine the value of lambda 0.

For a better understanding, the following concept map illustrates the procedure for obtaining fracture energy.



The image 52 depicts the type of specimen utilized for measuring fracture energy. It is evident that the green area of the specimen represents the region of interest for fracture energy measurement, while the red area of the sample is disregarded as it is not relevant to the analysis. Therefore, it is essential to determine the length and area within the green region for accurate fracture energy assessment.

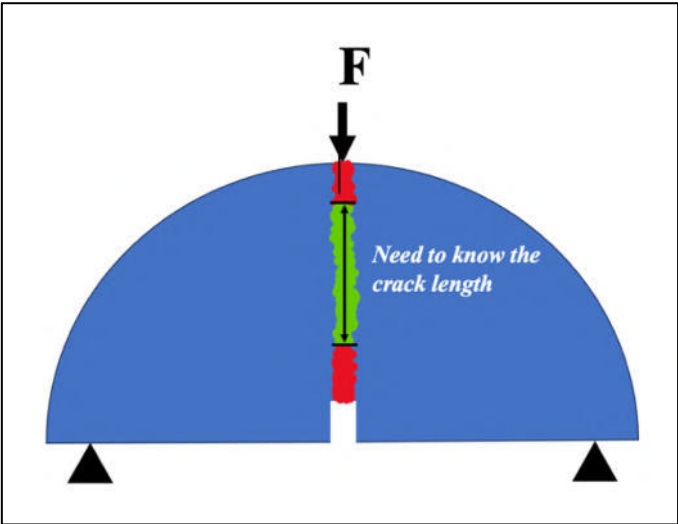


Figure 52. Choosing the cracking zone

3.7.5.1 Fracture Energy

The fracture energy is denoted G_f (J/m²) and is the energy required to generate a unit area of cracking. The fracture energy comprises both a material-specific component that we aim to assess, as well as a scaling component. The cracking energy is determined by the following formula:

$$G_f = \frac{W}{S} \tag{66}$$

Making measurements at the notch opening (CMOD). However, it is necessary to consider the following:

- CMOD displacement is not the displacement of the point of force application,
- CMOD force-displacement curve does not go all the way to total failure.
- The use of the loading point displacement δ for calculating the energy may include artefacts due to hertz deformations and local damage at the contact with the support and jack.

Therefore, the work (section W_{AB}) required to go from point A to point B on the force-displacement curve (Figure 53) was determined. Knowing the elastic energies at A (section W_{eA}) and B (section W_{eB}) and the principle of conservation of mechanical energy (equation 67), and equation 68 gives the value of the work resulting from crack propagation W_f between the two points. Then, the increment of the crack area generated between A and B was determined to determine the cracking energy.

If points A and B are chosen for cracking positions far from the edges, the method also avoids scale effects, which are particularly decisive for small structures, as is our case [15].

- $W_{eA} + W_{AB} = W_{eB} + W_f$ (Principle of conservation of energy) (67)
- $W_f = W_{eA} + W_{AB} - W_{eB}$ (68)

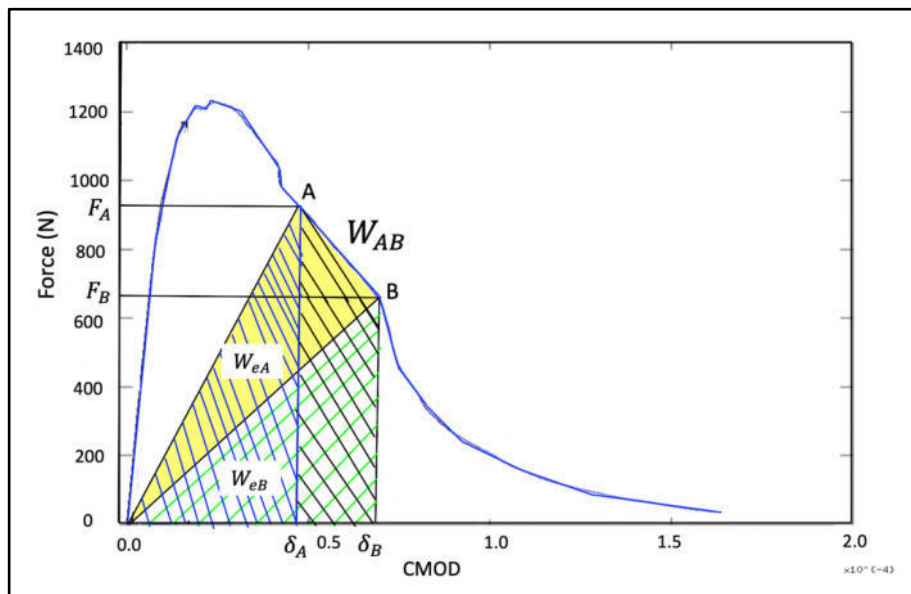


Figure 53. Principle for calculating work between A and B

In order to calculate the cracked surface and loading point displacement, we relied on numerical finite element simulations on the basis of loads and CMOD values. From a numerical point of view, it is agreed that nonlinear fracture mechanics theories more accurately represent cracking phenomena in quasi-fragile materials such as concrete [16]. However, an adaptation of the linear theory of fracture mechanics (LEFM) yields relevant results [17,18]. In our case, the complacency method was used. Compliance, denoted λ , is the inverse of stiffness (K).

It is obtained by dividing a displacement, noted δ , by the corresponding force, noted F . Relative compliance (noted λ) is the ratio of compliance (λ) to initial elastic compliance (λ_0). In our case, to account for dimensional variability between specimens, each specimen was modeled independently in Castem. As the problem is symmetrical, only half the specimen is represented (circular mortar specimen). The boundary conditions are the displacement locks of the nodes linked to the axis of symmetry, which corresponds to the crack ligament. The digital loading is a unitary force ($F \delta$), applied at the center of the specimen.

For each equivalent crack length, we need to calculate:

- Compliance for notch opening
- Compliance for the movement of the samples (*delta*)

$$\lambda_{CMOD} = \frac{u_{CMOD}}{F_u} \quad \text{and} \quad \lambda_{CMOD}^- = \frac{\lambda_{CMOD}}{\lambda_{0,CMOD}} \quad (69)$$

$$\lambda_{delta} = \frac{u_{delta}}{F_u} \quad \text{and} \quad \lambda_{delta}^- = \frac{\lambda_{delta}}{\lambda_0} \quad (70)$$

Figure 54. Process method

The crack is progressively simulated by releasing the symmetry plane nodes that correspond to the crack. For each node release, an elastic calculation is performed. Since we're working on the assumption of small perturbations, in elasticity the value of the complacency does not depend on the force intensity, but only on the geometry of the structure (including the length of the cracked ligament) and its elastic characteristics. Also, it is necessary to consider that for each value of the experimental force (F) can be established: **1)** The equivalent crack length (a_{eq}), **2)** The opening of the crack $CMOD = \Lambda_{Cmod} * F$, **3)** The displacement of the specimen $\delta = \Lambda_{Delta} * F$

For a given crack length, the relative complacency is calculated with the notch opening, which is twice the displacement of point 1, i.e. the starting point (which corresponds to the displacement of the notch opening sensor in the experiment (CMOD, equation 67), and with the displacement of the center of the rollers, (λ rollers, equation 68). The numerical model can be calibrated with the experimental results, and a correction factor, R (equation 71), is defined as the ratio of the experimental elastic compliance CMOD to the numerical elastic compliance CMOD.

$$R = \frac{\lambda_{0,CMOD,exp}}{\lambda_{0,CMOD,numerical}} \tag{71}$$

The parameter R is also used to recalculate the Young's modulus of the tested DCT specimen (equation 72).

$$E_{corr} = \frac{E_{num,ini}}{R} \tag{72}$$

The set of simulations is used to calculate the numerical relative complacency ($\lambda_{CMOD, numerical}$) for each equivalent crack length (Figure 55).

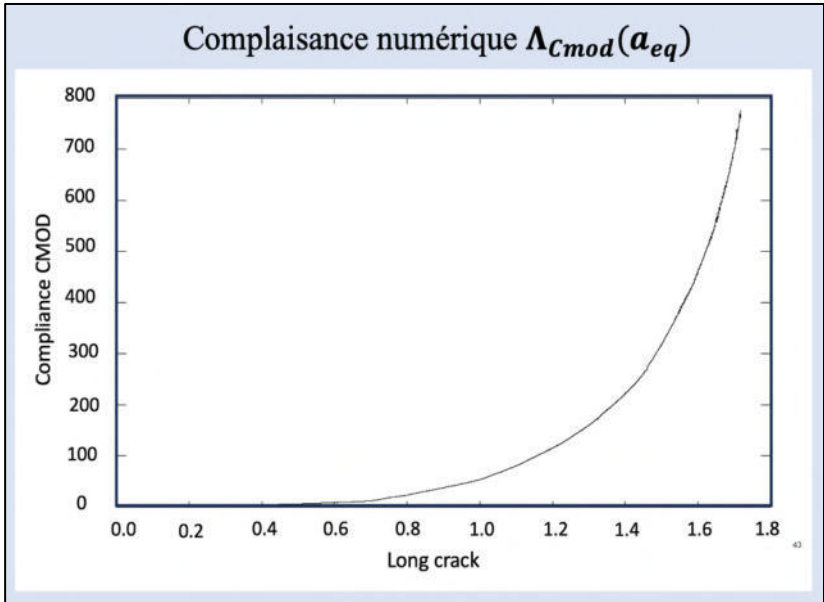


Figure 55. Complacency curve (Equivalent crack length)

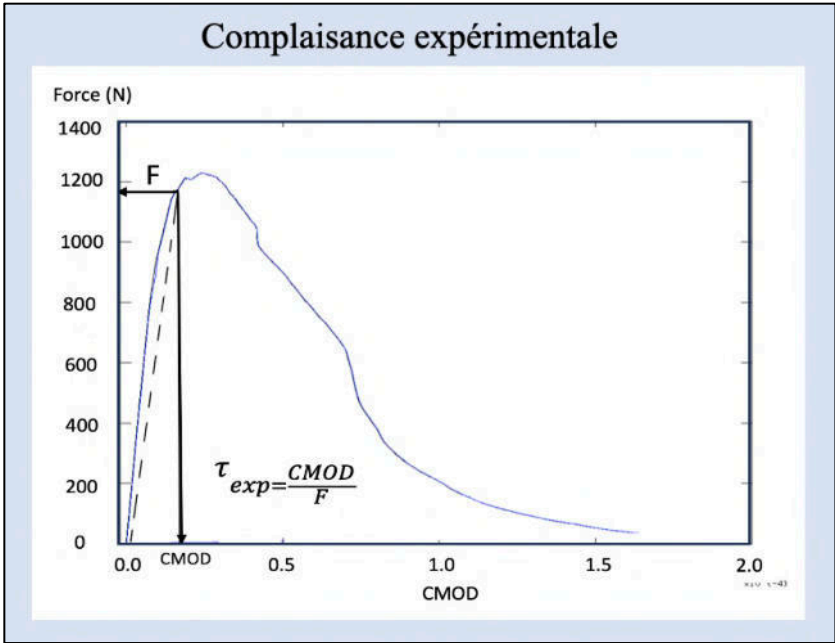


Figure 56. Complacency experimental of the mortar sample of 10 cm of diameter

For each experimental measurement located after the elastic limit, the experimental relative complacency ($\lambda_{CMOD, experimental}$) is calculated using the measurements closest to the specimen, i.e., the CMOD. The numerical configuration corresponding to this experimental point is the one with the same relative complacency ($\lambda_{CMOD, numerical} = \lambda_{CMOD, experimental}$). We can therefore deduce not only the equivalent crack length, but also the displacements of all points in the structure, and in particular the displacement of the point of application of force (point of study in the sample). Figure 57 displays the reconstructed force-displacement curve for the rollers, which closely matches the experimental force-displacement curve of the LVDT. Any significant deviations can be attributed to deformations in the contacting parts and potential rotation of the specimen support.

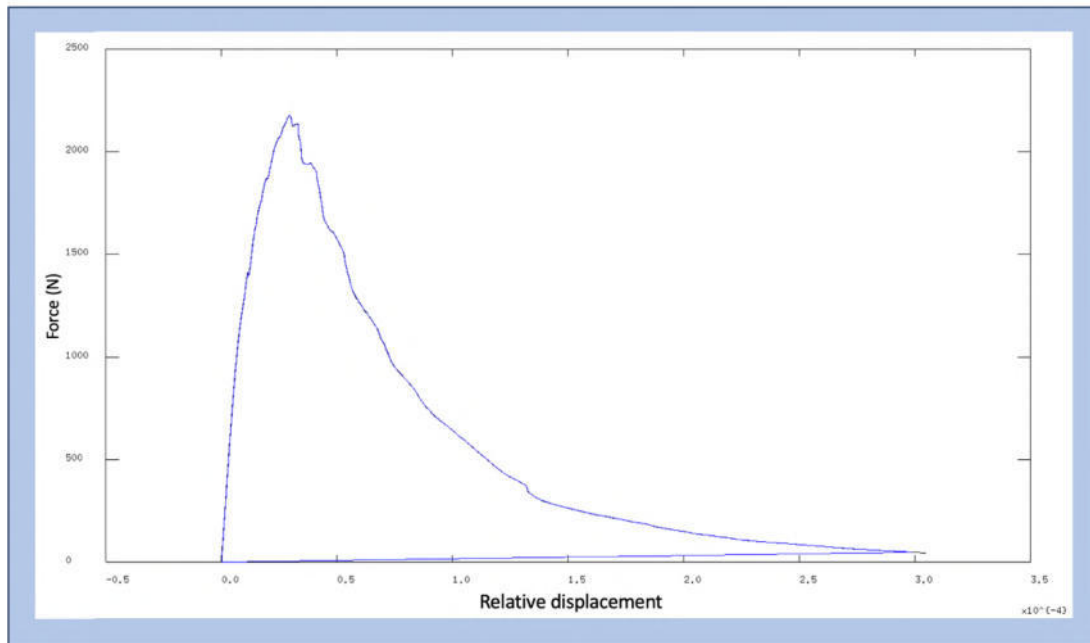


Figure 57. Relative displacement

To eliminate as far as possible the edge effects associated with crack initiation and total failure of the specimen, the cracking energy is calculated between an equivalent crack length (green zone in the figure 52) a_A and a_B , which depends on the specimen diameter. The associated relative compliances are used to define the forces F_A and F_B associated with these equivalent lengths. The work, W_{AB} , is then calculated by integrating the curve in figure 54 between the forces F_A and F_B (equation 73, based on equation 68)(see figure 58). The work is then divided by the equivalent crack length generated multiplied by the width of the noted specimen e (equation 8).

$$W_{AB} = \int_{a_1}^{a_2} F(a) \delta(a) da \quad (73)$$

$$G_f = \frac{W_{1-2}}{(a_2 - a_1) * e} \quad (74)$$

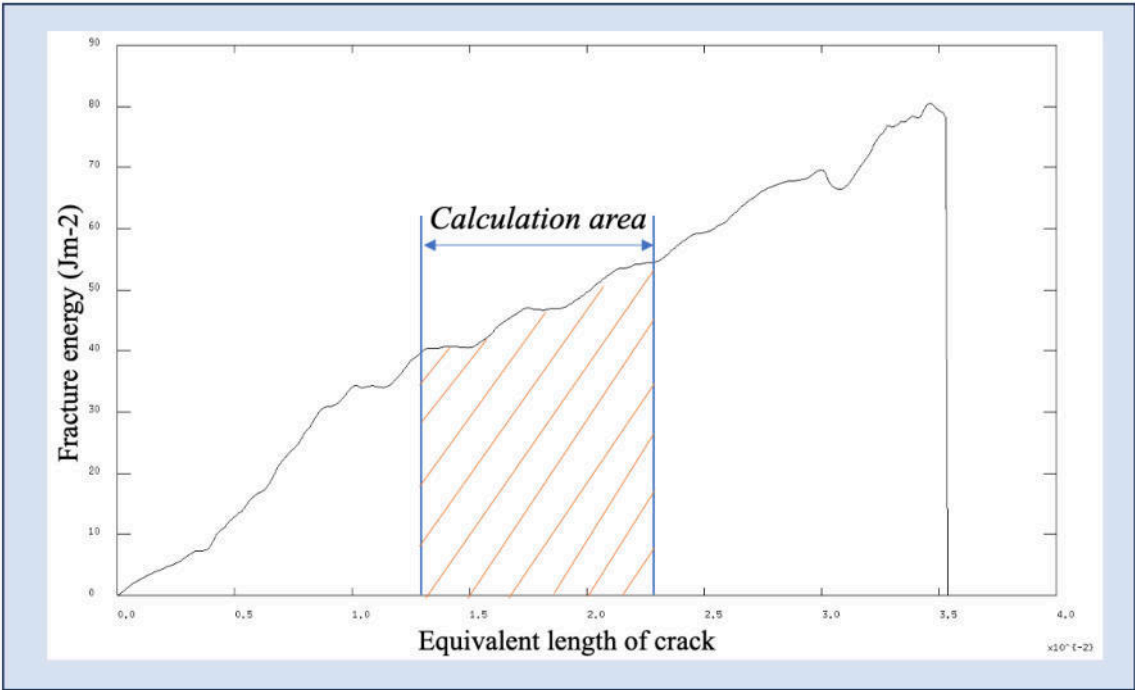


Figure 58. Fracture energy average over the central zone

References

- 1] Dora Carreon-Freyre. (2005). “Influencia de la estratigrafía y estructura geológica en el flujo de agua subterránea del valle de Querétaro”. *Revista mexicana de ciencias geológicas*, pag.18-22.
- 2] Maurel O, Rees T, Matallah M, De Ferron A, Chen W, Laborderie C, Pijaudier-Cabot G, Jacques A, Rey-Bethbeder F (2010) Electrohydraulic shock wave generation as a mean to increase intrinsic permeability of mortar. *Cem Concr Res* 40:1631–1638.
- 3] Chen W, Maurel O, Rees T, Sylvestre De Ferron A, La Borderie C, Pijaudier-Cabot G, Rey-Bethbeder F, Jacques A (2012) Experimental study on an alternative oil stimulation technique for tight gas reservoirs based on dynamic shock waves generated by pulsed electrohydraulic discharges. *J Pet Eng* 88–89:67–74.
- 4] Mei C, Fang Q, Luo H, Yin J, Fu X (2017) A synthetic material to simulate soft rocks and its applications for model studies of socketed piles. *Adv Mater Sci Eng* 2017, 1565438.
- 5] Gell EM, Walley SM, Braithwaite CH (2019) Review of the Validity of the Use of Artificial Specimens for Characterizing the Mechanical Properties of Rocks. *Rock Mech Rock Eng* 52:2949–2961.
- 6] ASTM C 642–13 (2013), Standard test method for density, absorption, and voids in hardened concrete. ASTM International, West Conshohocken, PA, www.astm.org.
- 7] Da Silva, B. G., & Einstein, H. (2018). Physical processes involved in the laboratory hydraulic fracturing of granite: visual observations and interpretation. *Engineering Fracture Mechanics*, 191, 125-142.
- 8] Zhou J, Chen M, Jin Y, Zhang G (2008) Analysis of fracture propagation behavior and fracture geometry using triaxial fracturing system in naturally fractured reservoirs. *Int j Rock Mech Min Sci* 45:1143–1152.
- 9] Wanniarachchi WAM, Ranjith PG, Perera MSA, Rathnaweera TD, Zhang DC, Zhang C (2018) Investigation of effects of fracturing fluid on hydraulic fracturing and fracture permeability of reservoir rocks: an experimental study using water and foam fracturing. *Eng. Fract Mech* 194:117–135.
- 10] Ouchterlony, F. 1988. “Suggested Methods for Determining the Fracture Toughness of Rock.” *International Journal of Rock Mechanics and Mining Sciences & Geomechanics Abstracts* 25 (2): 71–96. [https://doi.org/10.1016/0148-9062\(88\)91871-2](https://doi.org/10.1016/0148-9062(88)91871-2).
- 11] Chang, Soo-Ho, Chung-In Lee, and Seokwon Jeon. 2002. “Measurement of Rock Fracture Toughness under Modes I and II and Mixed-Mode Conditions by Using Disc-Type Specimens.” *Engineering Geology* 66 (1): 79–97. [https://doi.org/10.1016/S0013-7952\(02\)00033-9](https://doi.org/10.1016/S0013-7952(02)00033-9).
- 12] Hudson, J. A., & Harrison, J. P. (2000). *Engineering rock mechanics: an introduction to the principles*. Elsevier.
- 13] Zhou, Y.X., K. Xia, X.B. Li, H.B. Li, G.W. Ma, J. Zhao, Z.L. Zhou, and F. Dai. 2012. “Suggested Methods for Determining the Dynamic Strength Parameters and Mode-I Fracture Toughness of Rock Materials.” *International Journal of Rock Mechanics and Mining Sciences* 49 (January): 105–12. <https://doi.org/10.1016/j.ijrmms.2011.10.004>.
- 14] ASTM C469 A, Standard Test Method for Static Modulus of Elasticity and Poisson’s Ratio of Concrete in Compression, West Conshohocken, Pa, USA, 2014.
- 15] Elices, M., Guinea, G.V., Planas, J., 1992. Measurement of the fracture energy using three-point bend tests: Part 3—influence of cutting the P- δ tail. *Mater. Struct.* 25, 327–334.
- 16] Bazant, Z.P., 2002. Concrete fracture models: testing and practice. *Eng. Fract. Mech.* 69, 165–205. [https://doi.org/10.1016/S0013-7944\(01\)00084-4](https://doi.org/10.1016/S0013-7944(01)00084-4).
- 17] Bazant, Z.P., Kazemi, M.T., 1990. Size Effect in Fracture of Ceramics and Its Use to Determine Fracture Energy and Effective Process Zone Length. *J. Am. Ceram. Soc.* 73, 1841–1853. <https://doi.org/10.1111/j.1151-2916.1990.tb05233.x>
- 18] Bazant, Z.P., 1997. Scaling of quasibrittle fracture: hypotheses of invasive and lacunar fractality, their critique and Weibull connection. *Int. J. Fract.* 83, 41–65.

Appendix

Complete code:

Mortar Sample of 52.5 mm of diameter

- Opti trac PSC;
AA=LIRE 'CSV' 'Test1-52.5mm.csv' 'DEBU' 2 'SEPA' ', ';
EVCMOD_F=evol manu 'CMOD' (1.E-3*AA.2) 'FORCE' (AA.3);
dess EVCMOD_F;
EVDF=evol manu 'Disp' (-1.E-3*AA.4) 'FORCE' (AA.3);
- On divise par 2 la force et le deplacement car on modélise une 1/2 structure

```
FORCE1=(EXTR EVCMOD_F ORDO) ;  
CMOD1=(EXTR EVCMOD_F ABSC) ;  
DV1=EXTR EVDF ABSC;  
DV0=extr dv1 1;  
DV1=DV1 - DV0;  
dv2=enle dv1 1;
```

- Remove the first point in order to avoid 0 divisions

```
FORCE2=ENLE FORCE1 1;  
CMOD2=ENLE CMOD1 1;  
EVDF=evol manu 'Disp' dv2 'FORCE' FORCE2;  
FMAX1=MAXI FORCE2;
```

- Compliance

```
LAMBDA_CMODEXP=CMOD2 / FORCE2;  
EVCMOD2=EVOL MANU CMOD2 FORCE2;
```

we take the values that are between 10% and 25% of Max load, perform a linear regression and find the value at the origin to determinate the value of lambda_0

```
FMIN=0.1*FMAX1;  
FMAX=0.25*FMAX1;  
N1=DIME FORCE2;  
IMIN=1;  
REPETER BOU1 N1;  
F1=EXTR FORCE2 &BOU1;  
MESS &BOU1'F1 ' F1 'FMIN' FMIN 'FMAX' FMAX;  
SI (F1 < FMIN);  
IMIN=&BOU1 + 1 ;  
FINSI;  
SI (F1 > FMAX);  
IMAX=&BOU1 - 1;  
QUITTER BOU1;  
FINSI;  
FIN BOU1;  
LECT1=LECT IMIN PAS 1 IMAX;  
LECT2=LECT IMAX PAS 1 N1;  
FORCE3=EXTR FORCE2 LECT1;
```

CMOD3=EXTR CMOD2 LECT1;

Best linear fit of CMOD F curve between FMIN and FMAX
xml exl yml eyl a1 b1 r1 = @STAT CMOD3 force3;

progF0=prog FMIN FMAX;
CMODMIN=FMIN / A1;
CMODMAX=FMAX / A1;
FORCE4=FMIN ET (EXTR FORCE2 LECT2);

Exp shift on CMOD (suppose tht zero exp load is correct)

CMOD0=1*B1/A1;
CMOD4=CMODMIN ET (EXTR CMOD2 LECT2) + CMOD0;
LAMBDA_CMDEXP=CMOD4 / FORCE4;

Subtitute exp points with linear fit for f< fmax

EVCMOD4=EVOL MANU CMOD4 FORCE4;

PROGCMOD0=PROG CMODMIN CMODMAX;
EVCMOD0=EVOL ROUG MANU PROGCMOD0 PROGF0;

*LAMBDA3=EXTR lambda_cmosexp LECT1;
*EV3=EVOI MANU LAMBDA3 FORCE3;
*DESS EV3;

- Best linear fit

*xm ex ym ey a b r = @STAT lambda3 force3 ;
*force4= (a*lambda3) + b;
*EV4=EVOL MANU BLEU LAMBDA3 FORCE4;
*lambda0_CMDEXP= -1*b / a;
lambda0_CMDEXP=1/a1;

- Initial compliance

evlambda=evol manu lambda_cmosexp force4;
dess evlambda;

Lambdabar=LAMBDA_CMDEXP/LAMBDA0_CMDEXP;
EVLBAR=EVOL MANU CMOD4 LAMBDAbar;
DESS EVLBAR;

- Computation of the numerical compliance / crack length relation

opti dime 2 elem qua4 MODE PLAN CONT;
dens1=1.e-4;
dens2=2.e-4;

YGB=19.E9; NUB=0.2;
YGA=2.1E11;
NUA=0.28;

```
R1=52.5E-3/2.;
Th_notch=0.5E-3;
W_notch=6.69E-3;
EP1=40.0E-3;
A1=R1-(41.6e-3/2);
A_FRAC=EP1*(R1-W_notch);
th_calle=5.e-3;
ep_calle=4.E-3;
b_calle=1.e-2;

densite dens2;
CENT1=0. 0.;
P1=Th_notch 0.;
PC1=(th_calle + ep_calle) 0.;
PC2=(th_calle + b_calle) 0.;
PC3=(th_calle + b_calle) (-1*ep_calle);
PC4= th_calle (-1*ep_calle);
PAP=(R1 - A1) 0.;
P3=0. R1;
C1=LIGN ROTA cent1 -90. P3 ;
P2=C1 POINT FINAL;
P4=0. W_notch;
P5=Th_notch W_notch;
D1_1=D P1 PC1;
D1_2=D PC1 PC2;
D1_3=D PC2 PAP D P2;
D1=(D1_1 ET D1_2 ET D1_3) inve;
DLIG=D P4 P3 dini dens1 dfin dens1;
D2=D P1 P5 D P4;
cont1=D1 ET C1 ET DLIG ET D2;
CONT2= D1_2 ET (D PC2 PC3 D PC4 D PC1);
S1= SURFACE CONT1 PLANE COUL BLEU;
S2=SURF CONT2 PLANE COUL ROUG;
ST=S1 ET S2;
*TRAC S1;

MOD1=MODE S1 MECANIQUE ELASTIQUE;
MAT1=MATE MOD1 YOUN YGB NU NUB DIM3 EP1;
MOD2=MODE S2 MECANIQUE ELASTIQUE;
MAT2=MATE MOD2 YOUN YGA NU NUA DIM3 EP1;
MOTOT=MOD1 ET MOD2;
MATOT=MAT1 ET MAT2;

F1=FORCE FY (-0.5) P3;

CL1=BLOQ DLIG UX;
CL2=BLOQ PAP UY;
CLTOT=CL1 et CL2;

RIG1=RIGI MOTOT MATOT;
RITOT=CLTOT ET RIG1;
DEP1=RESO RITOT F1;
DEF1=DEFO DEP1 ST;
```

```
*TRAC def1;  
AMP1=EXTR DEF1 AMPL;  
Lambda_N0=2*(EXTR DEP1 UX PC4) ;
```

- On recalcule le module pour avoir les mêmes compliances initiales

```
YGB2=YGB*LAMBDA_N0/LAMBDA0_CMODEXP;  
MAT1=MATE MOD1 YOUN YGB2 NU NUB DIM3 EP1;  
MATOT=MAT1 ET MAT2;  
RIG1=RIGI MOTOT MATOT;  
RITOT=CLTOT ET RIG1;  
DEP1=RESO RITOT F1;  
Lambda_N0=2*(EXTR DEP1 UX PC4) ;  
LAMBDA_r0=-1*(extr dep1 uy p3) ;  
message 'lambda_N0=Lambda_N0 'lambda_exp0=' LAMBDA0_CMODEXP;  
*opti donn 5;
```

- Crack progression along DLIG

```
N1=(DLIG NBEL) - 1;  
Proga=prog 0.;  
progLN=prog 1.;  
ProgLR=prog 1.;  
Xn1=mesu DLIG;  
elem1= 16275;  
SS1=prog;  
EPS1=prog;  
REPE BOU1 N1;  
  ELE1=DLIG ELEM 1;  
  DLIG=DIFF DLIG ELE1;  
  Xa=mesu DLIG;;  
  a=Xn1 - Xa;  
  Proga = proga et a;  
  CL1=BLOQ DLIG UX;  
  CLTOT=CL1 ET CL2;  
  RITOT=CLTOT ET RIG1;  
  DEP1=RESOU RITOT F1;  
  SS=sigm dep1 mod1 mat1;  
  eps=epsi dep1 mod1 mat1;  
  SS1=SS1 et (EXTR SS SMXX 2 elem1 1);  
  EPS1=EPS1 et (EXTR EPS EPXX 2 elem1 1);  
* dess (evol chpo dep1 ux d1);
```

- Compliances computation (the load=1)

```
Lambda_R=-1*(EXTR DEP1 UY P3) /LAMBDA_R0;  
Lambda_N=2*(EXTR DEP1 UX PC4)/Lambda_N0;
```

```
ProgLN=ProgLN ET Lambda_N;  
ProgLR=ProgLR ET Lambda_R;
```

```
DEF1=DEFO DEP1 (AMP1/10.) ST;  
* TRAC DEF1 NCLK;
```

```
FIn BOU1;  
opti trac open;  
dess (evol manu eps1 ss1);  
EVOLLR=EVOL BLEU MANU PROGA PROGLR;  
EVOLLN=EVOL ROUG MANU PROGA PROGLN;  
DESS (EVOLLR et evolln) ;
```

```
NA=DIME PROGA;  
PGF=PROG;  
PWF=PROG;  
PGF1=PROG;  
PWF1=PROG;
```

```
PLVDT=PROG;  
PWE=PROG;  
PWE1=PROG;
```

```
M=1;  
REPETER BOU1 (NA - M);  
AI=EXTR PROGA &BOU1;  
AJ=EXTR PROGA (&BOU1 + M);
```

- On cherche les compliances relatives correspondantes

```
LBARI=EXTR PROGLN &BOU1;  
LBARJ=EXTR PROGLN (&BOU1 + M);
```

- On cherche les forces expérimentales correspondantes

```
IFI= (IPOL LBARI Lambdabar force4 tous);  
IFJ= (IPOL LBARJ lambdabar force4 tous);  
SFI=SOMME LFI;  
SFJ=SOMME LFJ;  
NFI=DIME LFI;  
NFJ=DIME LFJ;  
SI (NFI EGA 0);  
FI=0.;  
SINON;  
fi=SFI/NFI;  
FINSI;  
SI (NFJ EGA 0);  
FJ=0.;  
SINON;  
fj=SFJ/NFJ;  
FINSI;
```

```
* LVDTI=maxi (IPOL LBARI lambdabar LVDT3 tous);  
* LVDTJ=maxi (IPOL LBARJ lambdabar LVDT3 tous);
```

- On cherche les déplacements force correspondants

```
LBARFI=(EXTR PROGLR &BOU1);
```

```

LBARFJ=(EXTR PROGLR (&BOU1+M));
LBARI=(EXTR PROGLN &BOU1);
LBARJ=(EXTR PROGLN (&BOU1+M));
DI=FI*LBARFI*Lambda_R0;
DJ=FJ*LBARFJ*Lambda_R0;
CMODI=FI*LBARI*Lambda_N0;
CMODJ=FJ*LBARJ*Lambda_N0;
SI (&bou1 ega 1);
PD=PROG 0 ;
PF=PROG 0 ;
PCMOD=PROG 0 ;
FINSI;

```

- **Calcul des énergies avec compliance num**

```

WEI=FI*DI/2.;
WEJ=FJ*DJ/2.;

WIJ=(DJ - DI)*(FI + FJ)/2.;
W_Frac=WeI+WIJ-WEJ;
message 'Ai=' Ai 'Aj=' AJ 'Di=' DI 'DJ=' DJ 'FI=' FI 'FJ=' FJ ;
Message 'WEI=' WEI 'WEJ=' WEJ 'WIJ=' WIJ 'W_frac' W_frac;
GfI=W_FRAC/(EP1*(AJ - AI));
PGF=PGF ET GFI;
PWF=PWF ET W_Frac;
PF=PF ET FJ;
PD=PD ET DJ;
PCMOD=PCMOD ET CMODJ;

```

- **Calcul des énergies avec lvdt**

```

* message 'increment de longueur de fissure :' (AJ - AI) ', Gf=' GFI ;
FIN BOU1;
L1=LECT (NA - M + 1) PAS 1 NA;
PROGA1=ENLE PROGA L1;

EVGF=EVOL MANU PROGA1 PGF;
DESS EVGF;
J2=(INTG EVDF)/ A_FRAC;
TITRE 'Energie de fissuration moyenne obtenue par aire de la courbe ' J2;
DESS EVGF;
EV1=EVOL BLEU MANU PD PF;
evcmo_num=evol bleu manu pcmo pf;
DESS (EVCMOD_F ET EVcmo_num);
@excel1 evgf 'evgf.csv';
*hypothèse raideur machine + montage constant:
AN DMAXN FMAXN=MAXI EV1;
AE DMAXE FMAXE=MAXI EVDF;
KN=FMAXN/DMAXN;
KE=FMAXE/DMAXE;
KM=1/((1/KE) - (1/KN));
PD2=PD + (PF/km);

```

```
ev2=evol manu pd2 pf;  
dess (ev2 et evdf);
```

- On étudie la valeur de la "raideur machine" sur la partie croissante

```
l5=LECT 700 pas 1 (ae - 6000);  
dv5=extr dv2 l5;  
lf5=extr force2 l5;  
fmax5=maxi lf5;  
dmaxn=mini (ipol fmax5 pf pd tous);  
masq1=pd masque infe dmaxn;  
N5=(entier (somm masq1)) - 1;  
le5=lect 1 pas 1 n5;  
pd5=extr pd le5;  
pf5=extr pf le5;  
pd5=pd5 et dmaxn;  
pf5=pf5 et fmax5;  
pd52=ipol lf5 pf5 pd5;  
pke=lf5/(dv5 - pd52);  
evke =evol manu lf5 pke;
```

- Eavec ke au carré on a une belle droite

```
PKE2=PKE **2;  
evke2 =evol manu lf5 pke2;  
XM EX YM EY A B R=@stat lf5 pke2;  
PKM2=(A * PF) + B;  
PKM=PKM2**0.5;  
PD5=PD + (PF/PKM);  
ev5=evol roug manu pd5 pf;  
dess (ev5 et evdf);
```

CHAPTER IV RESULTS AND DISCUSSION

The results obtained in the experimental part presented in Chapter II are shown below with an interpretation or analysis. The results correspond to the values obtained in the mechanical and hydromechanical characterization of rocks and synthetic rocks that corresponded to the estimation of the permeability coefficient and fracture energy at room temperature and high temperature. Then, the values obtained in the three-point test and in the numerical simulation are shown.

4.1 Porosity

The connected porosity of the material, denoted as ϕ , was evaluated by hydrostatic weighing: Eq. (75):

$$\phi = \frac{M_w - M_a}{M_w - M_l} \quad (75)$$

M_w : Mass in water, M_a : Mass in air, M_l : Density of water

On average, the connected porosity was 14.07 % of porosity or void fraction (measure of the void) in the mortar sample. Considering that porosity is important in terms of moisture transport and mechanical properties, then the value obtained refers to the volume that is not composed of solids and is expressed as a percentage of the apparent volume. In other words, it is the total pore volume through the pore size distribution and the specific surface area of the specimens [1].

4.2 Mechanical characterization

To measure the elastic properties of the material and the compressive strength, the specimens were tested in uniaxial compression using a GCTS RTR 2000 triaxial machine. Subsequently, Brazilian tests were performed to obtain the tensile strength of mortar samples. Table 4 summarizes the average results obtained on five mortar samples for each test:

Table 4. Results in mechanical characterization for mortar samples

Mechanical Characterization	
Maximum compressive strength	29.78 ± 0.752 MPa
Young modulus	13.62 ± 0.397 GPa
Poisson's ratio	0.15 ± 0.00548
Tensile strength	2.95 ± 0.110 MPa

Considering the limited availability of rock specimens, the estimation of elastic properties was done by a non-destructive test (Ultrasonic Wave Propagation Test) on a GCTS RTR 2000 triaxial machine. Table 5 and 6 show the results for the rock specimens.

Table 5. Estimation of elastic properties (Young modulus E , Poisson's ratio ν) and estimation of fracture properties (Maximum compressive strength σ_c) for rocks samples.

Ultrasonic wave propagation test	
Spécimen 4	
Axial Load 3 KN	
Sampling Rate: 40 MHz	
Young modulus (GPa)	24.98 GPa \pm 5 %
Poisson's ratio ν	0.29 \pm 5 %
Shear Modulus (GPa)	9.75 \pm 5 %

Table 6. Estimation of fracture toughness for rocks samples

Mechanical Characterization	
Properties (MPa)	Specimen 3
Indirect tensile strength max	4.22
Compressive strength (MPa)	41.50 \pm 5 %

The values obtained in the mortar specimens are like those reported in the literature for a mortar mix with a CPC 30R cement with a W/C ratio of 0.45 and 28 days of curing. The results of the rock specimens cannot be directly compared with those reported in the literature because the value of a mechanical characterization depends on the origin of the rocks.

The parameters obtained in the mortar and rock specimens during mechanical characterization with destructive and non-destructive tests were used in the numerical simulation. The objective of making mortar specimens and classifying them as artificial or synthetic rocks was to have a wider margin of trial and error in hydromechanical characterization at laboratory level, it is usual to use synthetic rocks as mortar and concrete to develop new experimental techniques, as in our case, since the general objective was to develop a new method to calculate fracture energy by hydraulic fracturing [see, for example, Maurel et al. (2010) or Chen et al. (2012)] [2][3], Mei et al. (2017) [4] have reported the successful use of synthetic rocks made from a mixture of cement, gypsum, sand, and water, and the validity of this approach has been recently reviewed (Gell et al. 2019) [5].

4.3 Permeability test

For the calculation of the intrinsic permeability of mortar, denoted as K , we assumed a radial flow in the hollow cylindrical specimen, from the inner surface of the specimen to its outer surface and used Darcy's law. Hence, the permeability reads:

$$K = \frac{Q \mu \ln(b/a)}{2\pi H(p_i - p_e)} \quad (76)$$

where Q is the measured flow rate (m^3/s), μ is the dynamic viscosity ($\text{kN}\cdot\text{s}/\text{m}^2$), b the outer radius of the specimen, a is the inner radius, H the height of the specimen, p_i the inner pressure (kN/m^2) and p_e is the outer pressure (kN/m^2), the atmospheric pressure. The dynamic viscosity of the injected oil was provided by the manufacturer and was calculated by the Norm ASTM D 445-06 [6]. The oil used was Mobil DTE 25 with a dynamic viscosity of $0.03872 \text{ kN}\cdot\text{sec}/\text{m}^2$ at room temperature and $0.00587 \text{ kN}\cdot\text{sec}/\text{m}^2$ at 100°C . Fig. 56 shows a typical recording of the fluid flow rate vs the injection pressure. Table 7 and 8 show the permeability coefficients obtained for the samples.

Table 7. Permeability test in mortar samples

Average permeability coefficient			
Room temperature		High temperature	
Specimen	$K \text{ (m}^2\text{)}$	Specimen	$K \text{ (m}^2\text{)}$
14	0.98E^{-18}	45	$7.46\text{x}10^{-18}$
40	1.98E^{-18}	46	$15.00\text{x}10^{-18}$
42	5.93 E^{-18}	47	$7.49\text{x}10^{-18}$
44	5.90 E^{-18}	48	$5.98\text{x}10^{-18}$

Table 8. Permeability test in rock samples

Average permeability coefficient			
Room temperature		High temperature	
Specimen	$K \text{ (m}^2\text{)}$	Specimen	$K \text{ (m}^2\text{)}$
2	0.82E^{-18}	12	$9.64\text{x}10^{-18}$
8	0.26E^{-18}	13	$9.54\text{x}10^{-18}$
11	1.83 E^{-18}	9	$1.27\text{x}10^{-18}$
7	9.17E^{-18}	5	$8.27\text{x}10^{-18}$

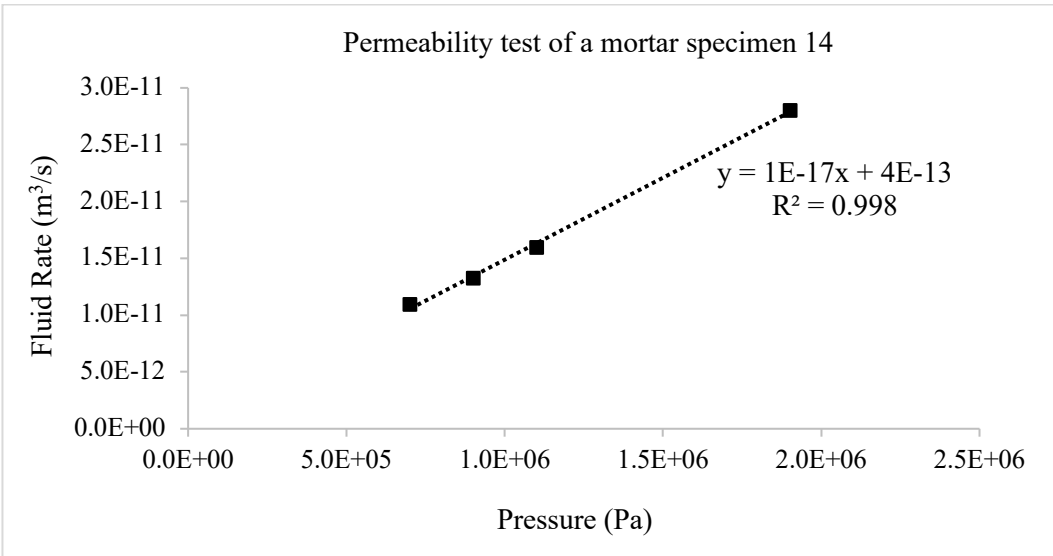


Figure 59. Evolution of injected fluid flow rate as a function of the injection pressure in mortar sample 14.

Table 9 shows the average permeability of all the specimens used in the permeability tests. A total of ten samples were used, i.e., five samples for room temperature tests and five samples for high temperatures test. Figures 57 shows the evolution of the flow rate of the injected fluid as a function of the injection pressure in mortar and rock specimens, where it can be observed that the permeability increases in the high temperature test.

Table 9. Permeability coefficient of the mortar and rocks specimens

Specimen	Temperature (°C)	Average Permeability (x10 ⁻¹⁸ m ²)
Mortar	20°	3.70
	100°	7.78
Rock	20°	3.97
	100°	7.13

Figures 58, 59, 60 and 61 show the evolution of permeability for each specimen, either mortar or rock, but in Figure 57, we can better see the behavior through a comparison between the two types of specimens. But analyzing the permeability test for each specimen, in Figure 58 we have the evolution of the permeability for the mortar specimens at room temperature and in Figure 59 for the high temperature test. Between these two graphs we can see that the permeability increases twice as much, probably due to the thermal expansion that the mortar specimen undergoes at a temperature of 100°C inside the oven.

The behavior presented in the mortar samples was again observed in the rock specimens. Figures 63 and 64 show the difference between the two tests at room temperature and high temperature, where the permeability increases (See figure 60). Regarding the values obtained for the permeability coefficient, similar values are reported in the literature, for example, P. Halamickova et al. reported for mortar specimens with 28 days of curing and permeability coefficients from 10^{-16} to 10^{-18} [7] and for rock specimens, Siavash Ghabezloo et al. reported values from 10^{-17} to 10^{-19} [8-9].

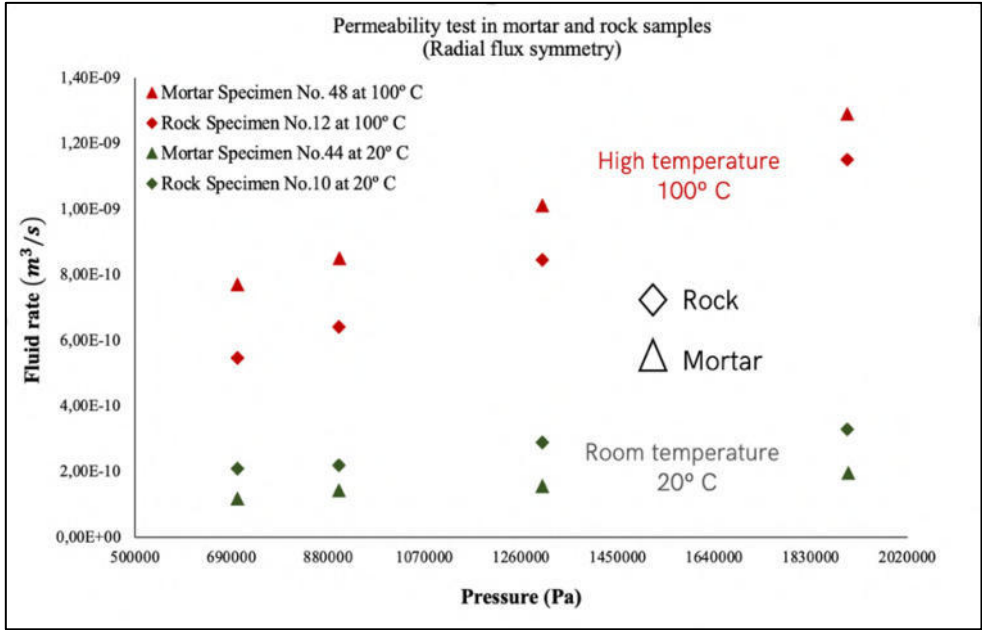


Figure 60. Permeability testing on some mortar and rock samples

In short, this kind of dispersion among the measurements is typical of what could be expected in such tests. For instance, Choinska et al. (2007) [10] observed dispersion of the same order on the permeability of concrete measured with nitrogen using a similar apparatus. The dispersion for each test on the two types of specimens can be seen in more detail below.

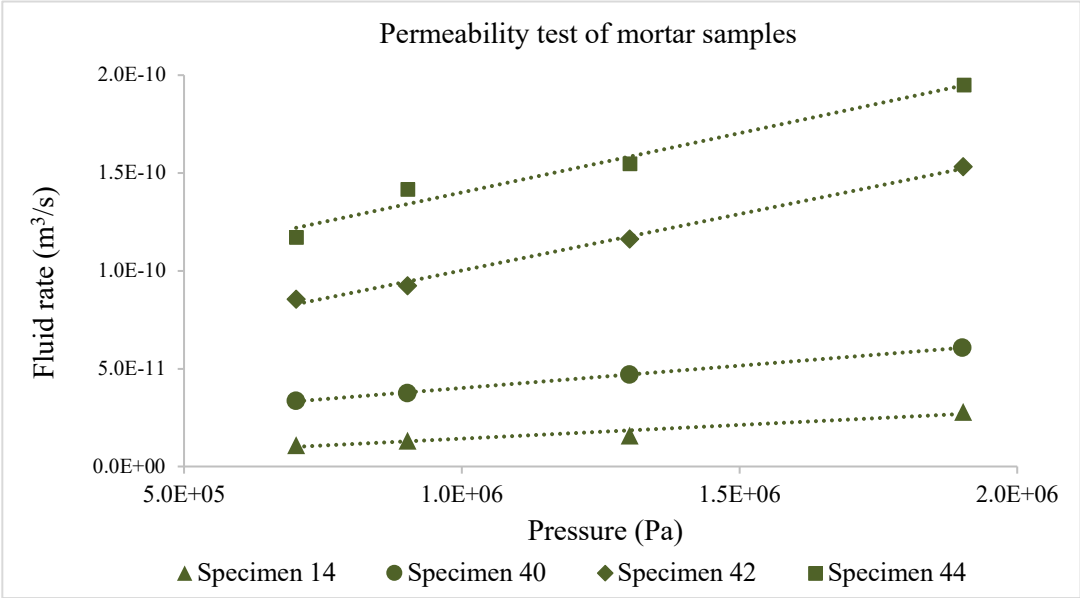


Figure 61. Permeability test at room temperature of mortar samples

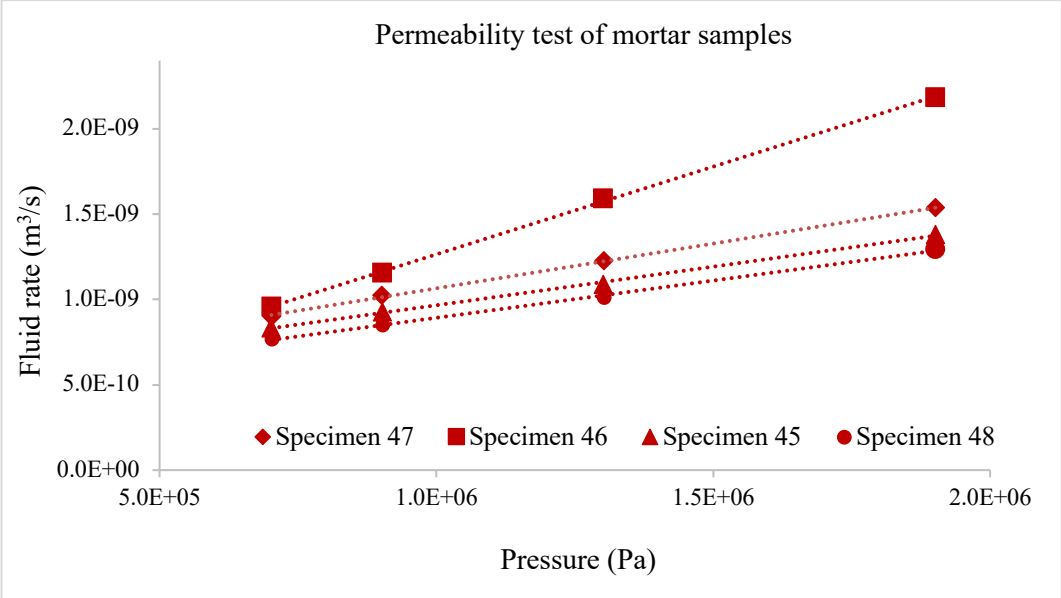


Figure 62. Permeability test at high temperature of mortar samples

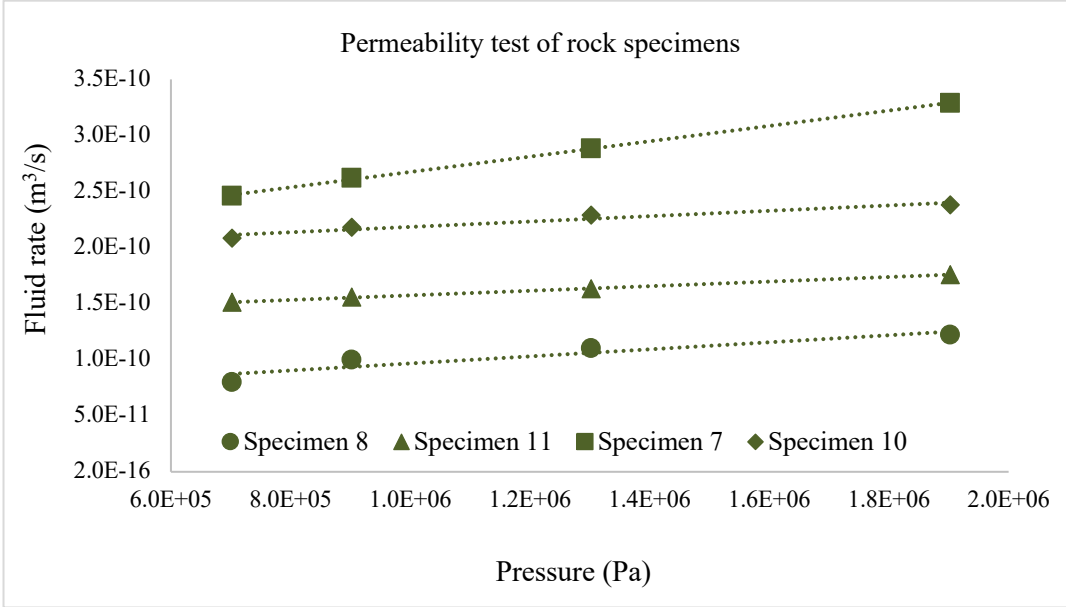


Figure 63. Permeability test at room temperature of rock samples

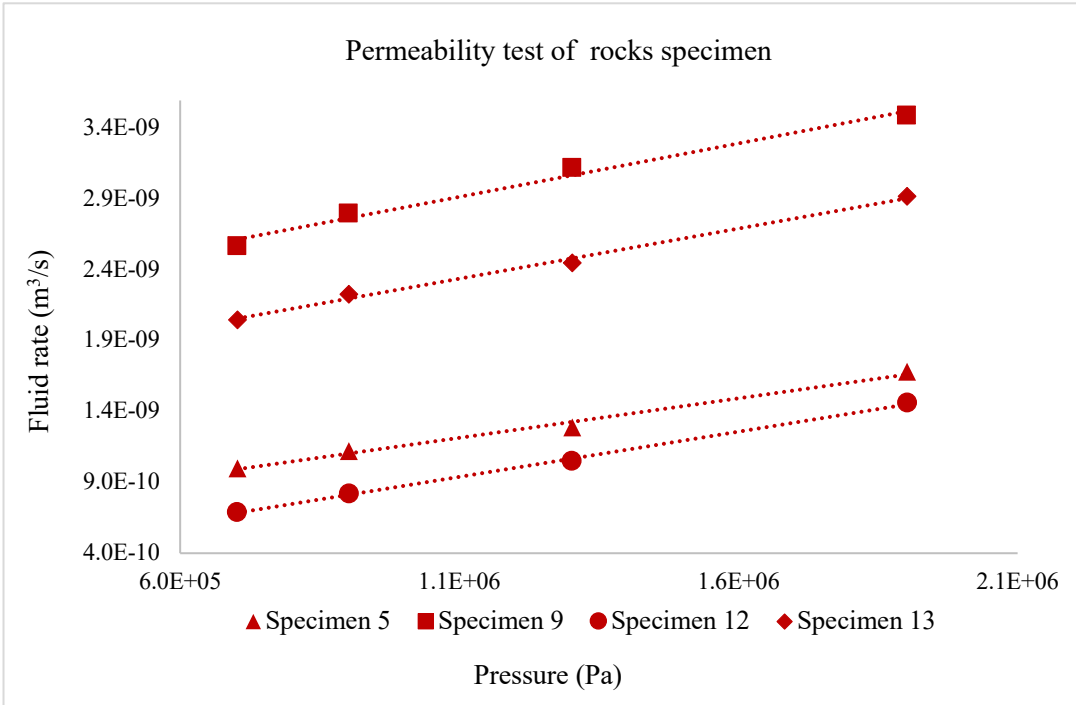


Figure 64. Permeability test at high temperature of rock samples

4.4 Hydraulic fracture test

4.4.1 Synthetic and natural rocks

As explained in Chapter III, to estimate the fracture energy, the different energies involved during the hydraulic fracture tests were considered. In short, the fracture energy can be easily obtained by integrating the pressure plots, as shown in figure 65. According to the conservation of energy, the energy supplied by the pump during the complete hydraulic fracturing process, at the end of the test corresponding to time t_f , must have been completely dissipated due to the viscosity of the fluid E_μ , or due to the fracture of the specimen E_f (Equation 77):

$$E(t_f) = E_\mu + E_f \quad (77)$$

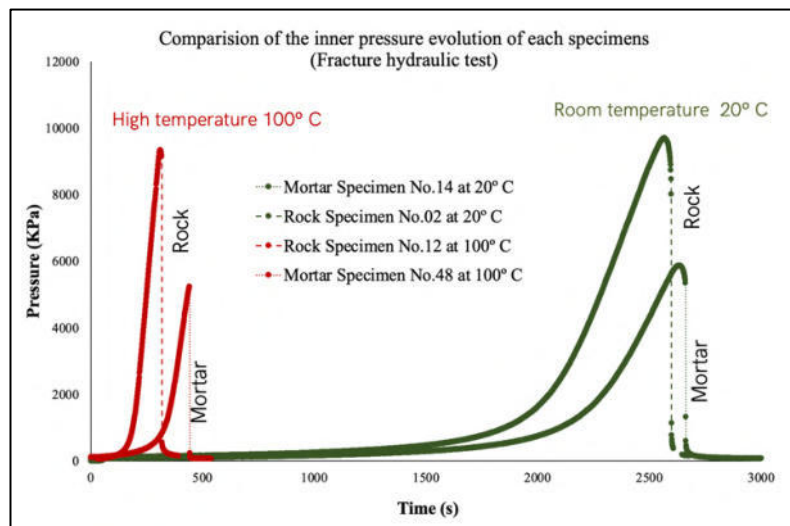


Figura 65. Comparison of pore pressure evolution in mortar and rock samples at 20° C and 100° C.

Over the specimen, Darcy's law translates into a linear relationship between pressure and fluid flow (which is kept constant) as illustrated in Figure 56. Therefore, this integral can be easily evaluated: for a typical fluid flow in the range of 0.1 mL/min, integrating over the duration of the test (2000-3000 seconds) using the slope obtained in Figure 59, an energy of the order of 0.01 Joules is obtained. In the case of temperature variations (e.g., from 20° to 100° C), the viscosity may change by an order of magnitude, but this energy will remain small or negligible. Compared to the energy expected to dissipate during fracture, E_μ is negligible. Therefore, the measured fracture energy does not depend on the properties of the pressure fluid in the present case.

This would not be the case if the energy dissipation due to fluid flow in the various devices or in the specimen due to Darcy flow is not negligible, or if the fluid reacts with the rock. Therefore, a correction of the energy balance would be necessary to arrive at an intrinsic estimate of the fracture energy. In the present experiments, Equation 77 gives the energy dissipated due to fracture as a function of the energy supplied by the pump. To obtain the fracture energy, we must divide E_f by the fracture area created during the test, A_f to be obtained experimentally. Therefore:

$$G_f = \frac{Q \int_0^t p_a dt}{A_f}. \quad (78)$$

Therefore, the fracture area created at the end of the hydraulic fracture test can be approximated as:

$$A_f = n(D_o - D_i)h, \quad (79)$$

where D_o and D_i are the outside and inside diameters of the specimen, h is the height of the specimen and n is the number of pieces in which the specimen is fractured. All specimens tested in this study were fractured in two parts and four fracture surfaces are generated (See Figure. 66), therefore, $n = 4$.

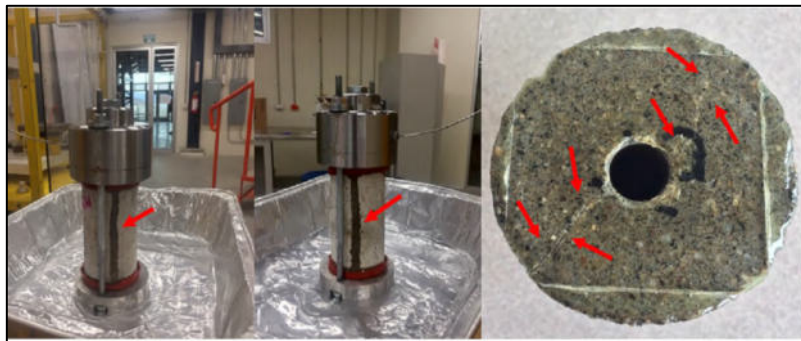


Figure 66. Mortar samples after hydraulic fracture test at room temperature, arrows indicate location of cracks.

Fracture energy estimation was obtained with equation 78, in mortar and rock specimens. The integrals of the pressure plots in Figure 62 were calculated according to the trapezoidal rule and the results are presented in Table 10 for some mortar and rock specimens. On average, a fracture energy of 92.97 Joules/m² was obtained and the standard deviation is 4.03 Joules/m² for mortar specimens (See Table 11). These values are very consistent with the typical fracture energies obtained and reported for mortar specimens with a similar water-cement ratio, using fracture mechanics tests, such as the Three-Point Bending test on notched specimens by Haidar et al. in 2005 who reported a fracture energy of 88.5 Joules/m² [11].

Table 10. Fracture energy values of specimens reported in Figure 62.

	Specimen	Temperature (°C)	Fracture energy (J/m ²)
Mortar	14	20°	97.89
	18	100°	131.65
Rock	02	20°	214.20
	12	100°	261.92

Table 11. Fracture energy values at room temperature in mortar specimens.

	Specimen	Temperature (°C)	Fracture energy (J/m ²)
Mortar	1	20°	97.89
	2		88.32
	3		94.06
	4		91.62
		Average	92.97
		Standard deviation	4.03

As mentioned above, only limestone rock specimens were used, since the maximum temperature recorded in the study area is present in the limestone rock layer, according to the stratigraphic profile (see image 32). Cylindrical rock specimens with the same dimensions as the mortar specimens were used. The specimens were tested at room temperature and at 100°C, a temperature chosen to be representative of the real conditions of geothermal reservoirs. For the tests at 100°C, the experimental equipment was placed in a Vulcan 3-400 oven regulated at constant temperature (see Figure 67). It should be noted that the present experiments could be performed at higher temperatures (e.g., above 200°C), but a limitation of our procedure is the flash point of the oil used for the turnover (232°C in our case). In addition, we stayed below this limit for safety reasons, as the tests were performed in a conventional laboratory. If higher temperatures are intended, a fluid with a higher flash point can be used.



Figure 67. Set-up for high temperature tests in limestone samples. The arrows indicate the location of through cracks after the test at 100° C.

The oven was turned on and the temperature was raised (heating ramp at a rate of 1°C/min) until 100°C was reached. Afterwards, the test tube was left for 20 minutes at 100°C and then the tests were started. In this way, the fluid inside the specimen was at the same temperature as the rock specimen. Also, the pipes connected to the steel device, the specimens inside the furnace were long enough to allow heat transfer and to achieve a balance between the fluid entering the specimen and the fluid already contained in the specimen. figures 71 and 72 shows the pressure plots for the rock specimens at both temperatures. In general, the curves are similar, except that the fluid flow was modified in tests at room temperature (0.05 mL/ min) and in tests at 100 °C (0.32 mL/min) due to the decrease in oil viscosity with increasing temperature, as reported by Reid et al. in 1987 [12]. This decrease in viscosity was considered in the permeability calculation.

A total of eight limestone samples were used, four at room temperature and four at 100°C. The average results are presented in table 11. We can observe from this table that the permeability increases with temperature by 44 %. This is consistent with measurements reported in the literature by Choinska et al. in 2007) [10]. In addition, there is a 20 % increase in fracture energy values. For example, in mortar specimens with the same procedure, a fracture energy of 93.42 J/m² at 20°C and 129.1 J/m² at 100°C was obtained. This increase in fracture energy observed in mortar specimens is also consistent with existing data in the literature, for example, in the data reported by Menou et al. in 2006 [13]. Figures 72 and 73 show the influence of temperature and the evolution of fracture energy values for mortar and rock specimens. The green color represents tests at room temperature and the red color represents tests at 100° C. Several explanations for this increase can be found in the literature: first, the fracture energy increases as microcracking occurs, due to differences in thermal expansion of the different minerals contained in the material [14]. The principle is that, due to the existing microcracks, a larger fracture can be arrested, therefore, more energy is needed to propagate. Also, it is accepted that fracture is a thermally activated velocity process, as published by Bazant and Prat in 1988 [15]. While thermal expansion occurs, the local fracture energy decreases locally, producing an increase in microfracture.

Finally, thermal expansion associated with heating from room temperature to 100°C can reduce the radius of curvature at the tip of microcracks, thus reducing the stress intensity factor, which will result in more energy being required to propagate a fracture.

Table 11. Summary of results obtained from limestone rock samples.

Amount	Temperature	Young Modulus (GPa)	Poission ratio (ν)	Permeability (m ²)	Connected porosity	Fracture energy (J/m ²)
4	20° C	24.98	0.29	4.5 X 10 ⁻¹⁸	0.30	213.50
4	100° C	--	--	6.5 X 10 ⁻¹⁸	--	258.70

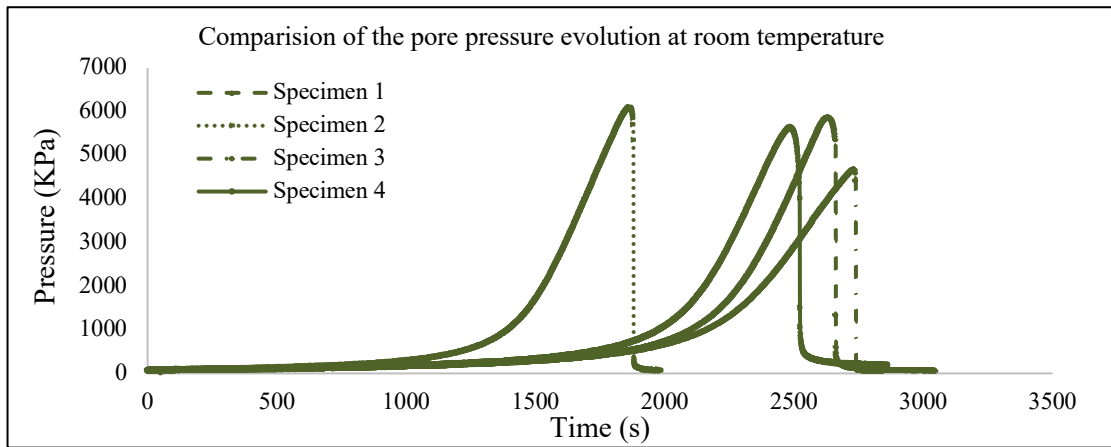


Figure 68. Hydraulic fracture test in mortar samples at room temperature

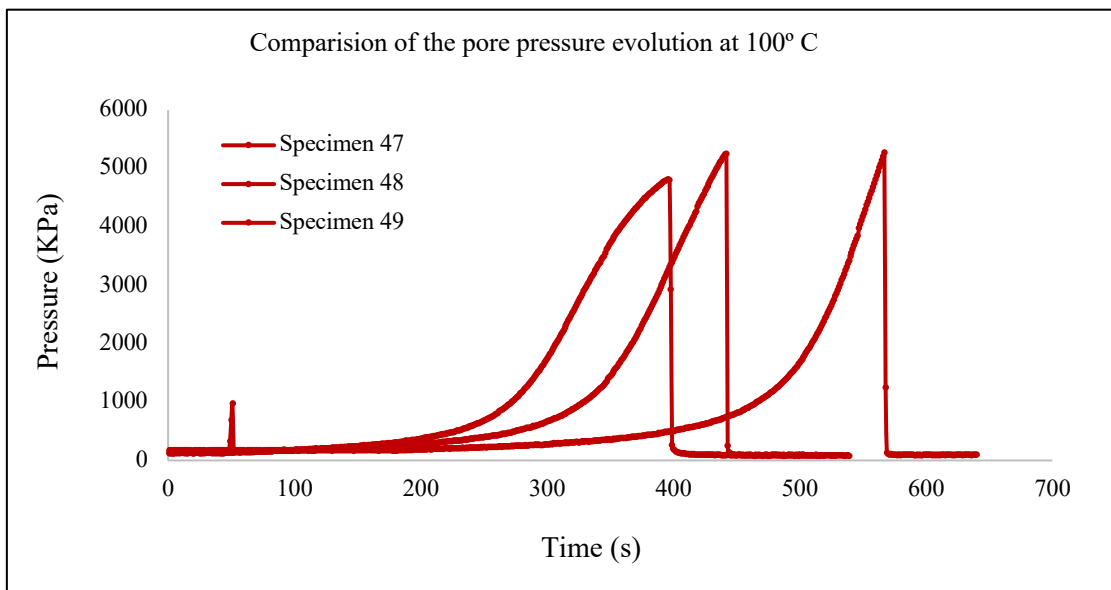


Figure 69. Hydraulic fracture test in mortar samples at high temperature

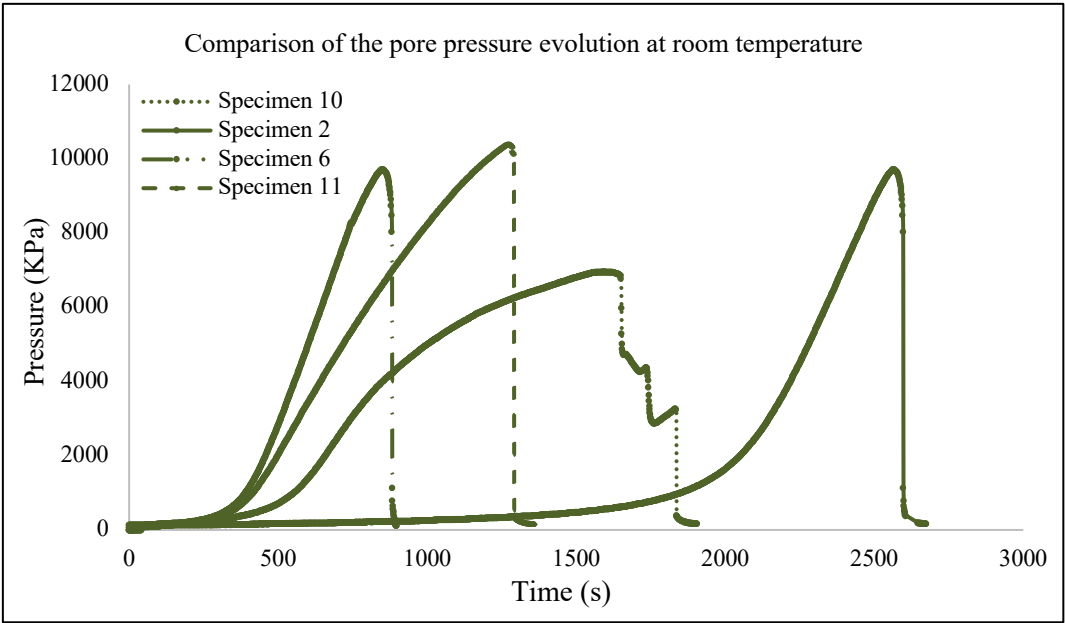


Figure 70. Hydraulic fracture test at room temperature of rock samples

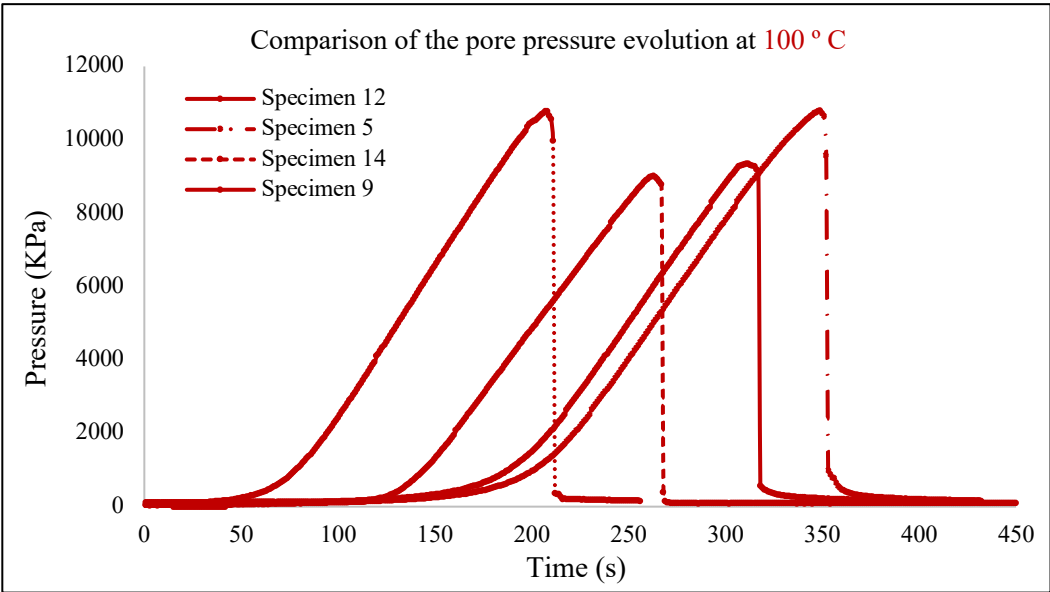


Figure 71. Hydraulic fracture test at high temperatures of rock samples

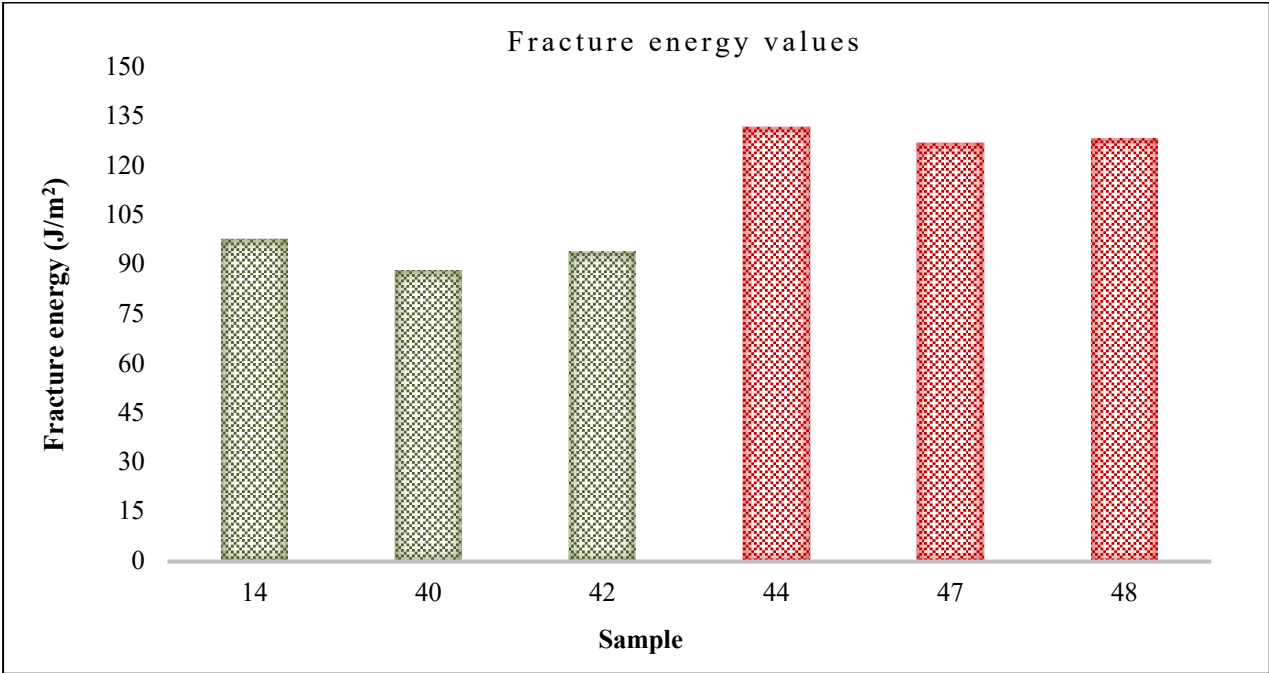


Figure 72. Fracture energy values of synthetic rocks at room temperature

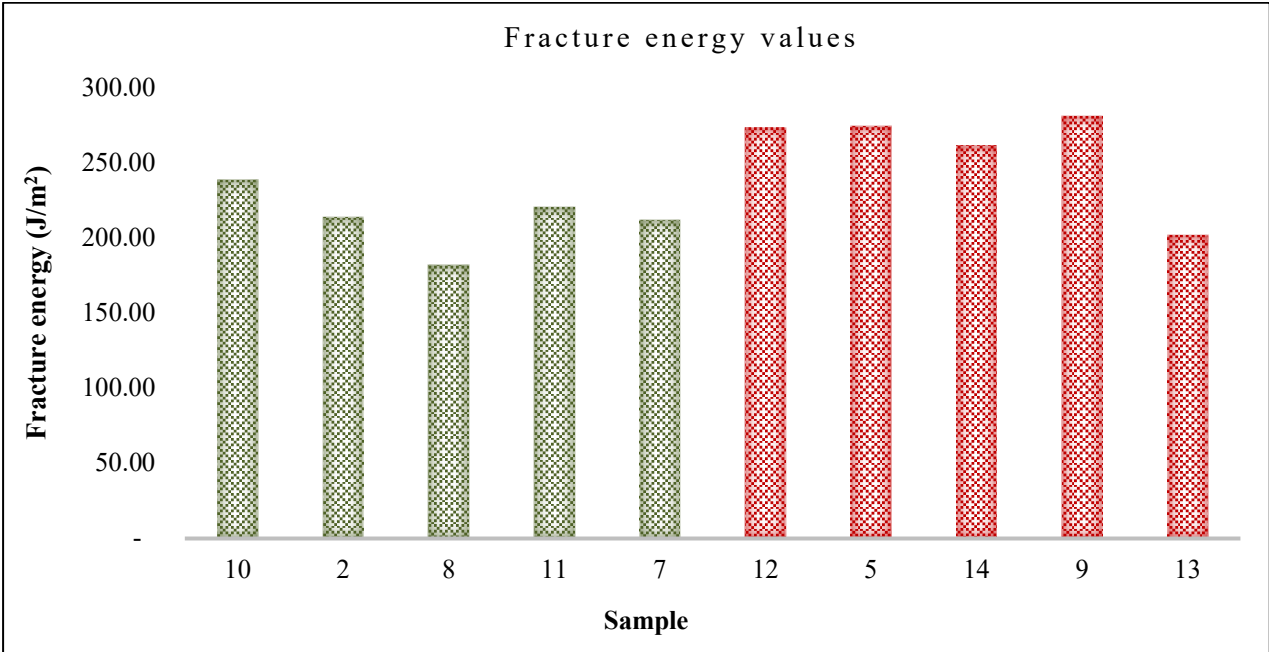


Figure 73. Fracture energy values of natural rocks test at room temperature

4.5 Corroboration of fracture energy values with a test reported in the literature

4.5.1 Three-Point bending test

To validate the fracture energy values obtained with the proposed method through a kinetic, potential and pressure energy balance, the three-point test was performed on mortar samples cut into half disks with notches made in 2021 and 2022. Tables 13 and 14 show the maximum force according to the diameter of each sample.

Table 13. Results of the bending test for mortar samples from 2021

Mortar sample	Diameter (cm)	Force (N)
1	10.20	2,113
2		2,108
3		2,119
Average		2113.34
<hr/>		
1	5.20	1,221
2		1,233
3		1,212
Average		1222
<hr/>		
1	2.50	598
2		591
3		604
Average		597

Table 14. Results of the bending test for mortar samples from 2022

Mortar sample	Diameter (cm)	Force (N)
1	20	3,281
6		3,406
7		3,148
Average		3,278.33
<hr/>		
1	10.20	2,177
6		2,226
3		2,336
Average		2,446.33
<hr/>		
1	5.20	1,391
2		1,001
3		1,163
Average		1,185

Figures 74 to 76 show the maximum strength obtained in the three-point test with the semi-circular mortar specimens that were manufactured in 2021. In the 2.5 cm diameter mortar specimens it was not possible to perform the bending test due to the size of the specimen, therefore, only the maximum force was obtained and not the deformation. Figures 77 to 79 correspond to the maximum strength of the mortar samples manufactured in 2022.

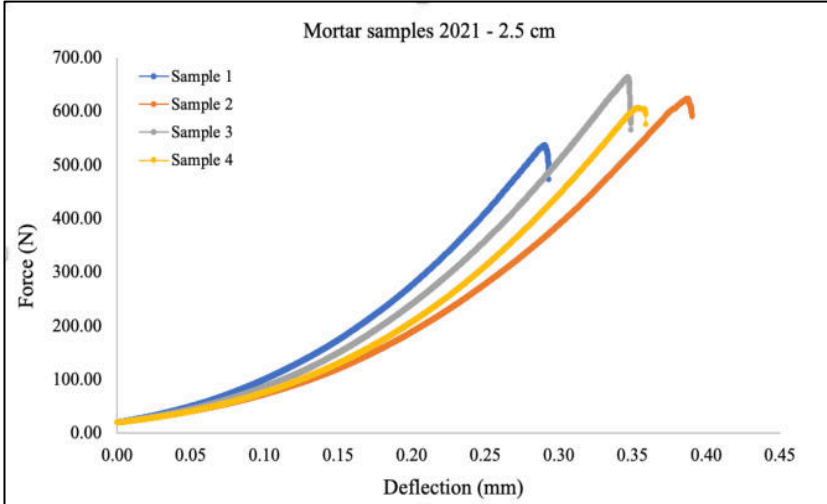


Figure 74. Mortar samples of 2.5 cm of diameter from 2021

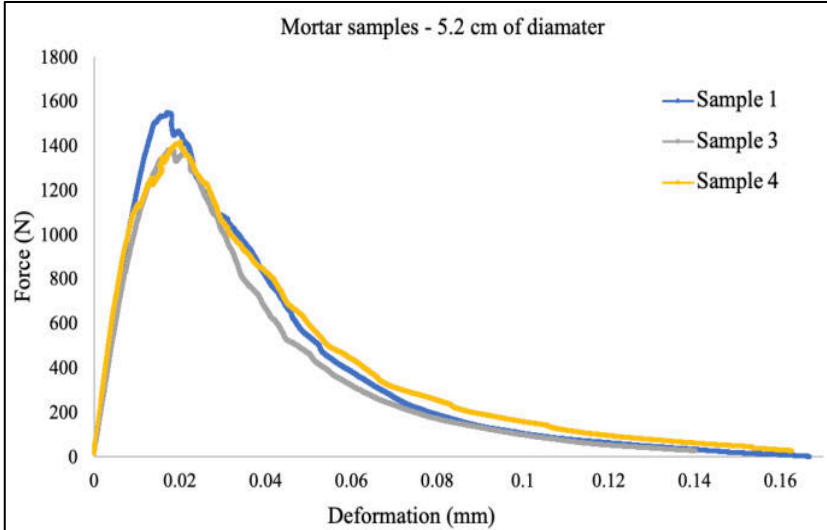


Figure 75. Mortar samples of 5.2 cm of diameter from 2021

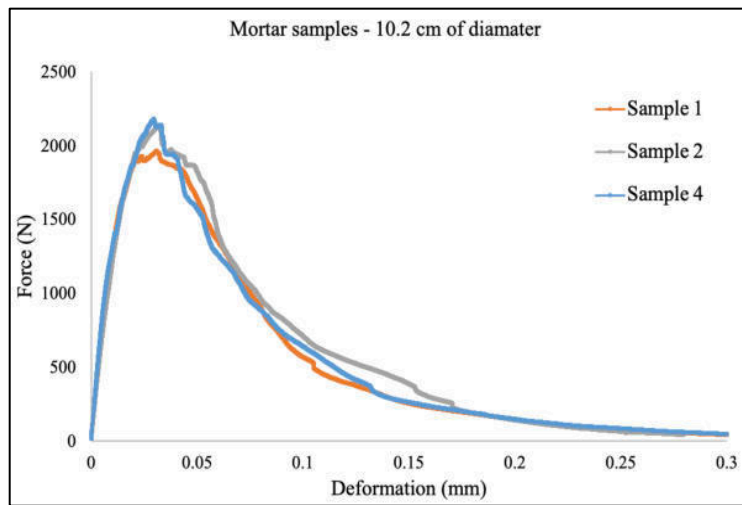


Figure 76. Mortar samples of 10.20 cm of diameter from 2021

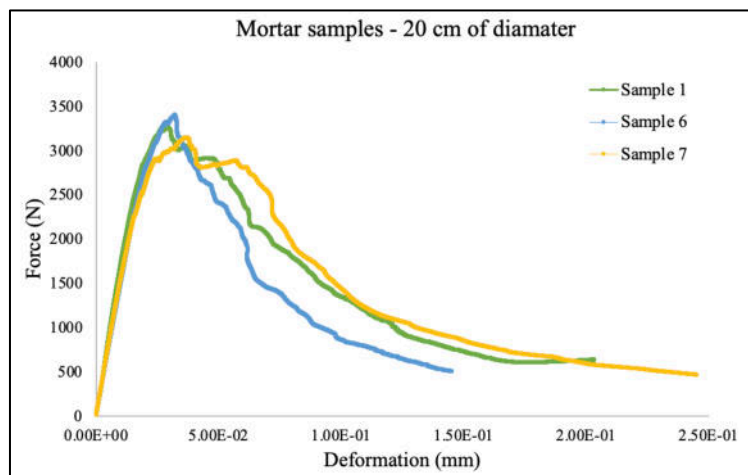


Figure 77. Mortar samples of 20 cm of diameter from 2022

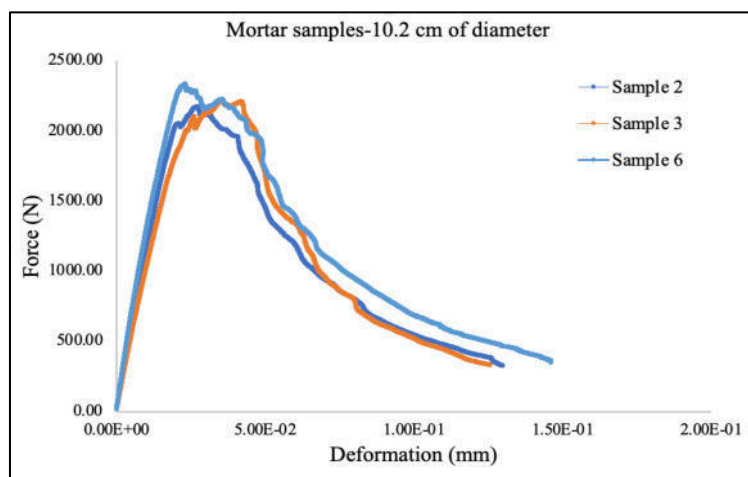


Figure 78. Mortar samples of 10.20 cm of diameter from 2022

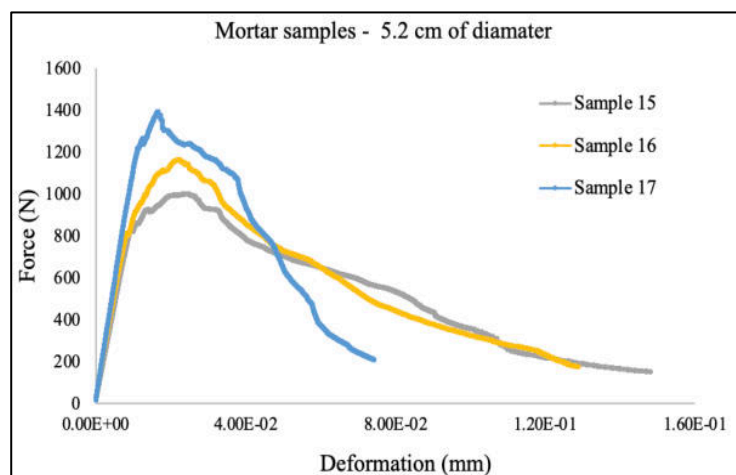


Figure 79. Mortar samples of 5.20 cm of diameter from 2022

After obtaining the maximum strength of each specimen with the three-point test, the fracture energy was determined from the effect of size and brittleness number with the method reported by Bazant, Z.P et Pfeiffer, P.A (1987) [16]. Also, we calculated the fracture energy in mortar samples through the utilization of the size effect approach, employing notched semicircular specimens. In contrast to prismatic samples, semicircular specimens exhibit a higher level of ease in their machinability when derived from cores. The experimental configuration adheres to conventional practices and is comparable to other studies examining size effects, as evidenced by existing literature [17-18]. Also, the ratio of the notch length a_0 to the radius of the specimen R is equal to 0.3. The thickness of the notch corresponds to that of the saw ($t = 2$ mm). The span l in the three-point bending test is equal to $1.6R$. Four different radii have been considered: $R = 25, 50, 100,$ and 200 mm. A perpendicular notch was employed due of its alignment with the anticipated direction of crack propagation in practical scenarios. The experimental setup employs a uniaxial testing frame with a maximum load capacity of 25 KN, upon which a three-point bending mechanism is installed. Two distinct kind of three-point bending testing have been conducted, namely Crack Mouth Opening Displacement controlled (CMOD) tests and displacement-controlled tests. To conduct the CMOD tests, it is necessary to position a sensor on either side of the notch located on the lower surface of the specimen, as explained in the previous chapter. The specimen is affixed between two metallic plates that are adhered to the bottom surface, excluding the area containing the notch. The load is delivered in a manner that results in a constant rate of $0.2 \mu\text{m/s}$ growth of the CMOD (Crack Mouth Opening Displacement). Displacement-controlled experiments have been employed in cases where it was impractical to position the sensor directly on the specimen, namely for the most diminutive specimens, for example, with mortar samples of 25 mm of diameter. In this scenario, the variable being considered is the displacement of the traverse of the testing machine, which undergoes movement at a consistent velocity of $1.0 \mu\text{m/s}$.

Figures 74 to 79 show the results of all the three-point tests, but sometimes the load-displacement curve is not linear at the beginning of the loading, since irreversible displacements occur in the supports, mainly due to the plastic deformation of the wooden plates placed between the supports and the specimens for greater stability. This phenomenon can be generated because one displacement response with respect to the other is simply since the curves have not been treated to eliminate the displacement mismatch between the loading device and the specimen existing at the beginning of the test as has been reported in the literature [19].

For example, using the size effect relationships, the ratio of g , which is a constant and is related to the geometry of the specimen, was obtained with the Equation 80. Considering that the size effect is due to the redistribution of stresses ahead of a crack tip, in the fracture process zone that typically applies to quasi-brittle materials that have a fracture process zone whose size cannot be considered negligible. Therefore, to perform this calculation from effect tests, specimens of geometrically similar size are required. A minimum of three different sizes is required, for example. For numerical analysis, we used three sizes of mortar specimens to determine Eq. 81 and Eq. 82 and to demonstrate the size effect, the fracture toughness of the two shales has been computed. The mode of hardness can be derived from Equation 83 as shown by Bao et al. in their study [20]. The dimensionless parameter Y_1 is dependent on both the geometric properties and the elastic constants. To analyze the relationship between fracture toughness and specimen size, it is necessary to consider the experimental conditions in which specimens were tested. Specifically, the bedding orientation with the applied load and the geometry of the specimens were kept constant. Consequently, we will examine the ratio of fracture toughness relative to specimen size, using the smallest size as a reference point. Tables 21 and 22 summarizes, for each shale and for each size, the ratio $K_{IC}(D)/K_{IC}(D = \text{diameter of sample})$ and the toughness increases with the size of the specimen.

$$G_f = \frac{g(\alpha_0)}{EA} \quad (80)$$

$$Y = AX + C \quad (81)$$

Where: $X=D$, $Y=(1/\sigma_N)^2$; A and C are constants to be fitted:

$$Bf_t = 1/\sqrt{C} ; D_0 = C/A \quad (82)$$

$$K_{IC} = \frac{F_{\max} \sqrt{\pi a_0}}{2RB} Y_1 \quad (83)$$

To validate the fracture energy values obtained through energy balance in hydraulic fracture, we employed the phenomenon of size effect resulting from stress redistribution ahead of the crack tip within the fracture process zone. This phenomenon was demonstrated by Zhang et al. [21] in their analogous experiments utilizing digital image correlation on sandstone specimens. This phenomenon is generally observed in quasi-brittle materials that exhibit a fracture process zone of non-negligible size, as described in more detail in reference [22]. Let us define first the nominal stress of our semi-circular notched specimens denoted as σ_N :

$$\sigma_N = \frac{3}{2} \frac{Fl}{b(D/2-a)^2} \quad (84)$$

where F is the peak load, b is the thickness of the specimen, l is the span, D is the diameter of the specimen, and a is the notch length. The nominal stress is calculated here, according to the beam theory, as the maximum tensile stress in the ligament at the middle section of the specimen. In its simplest form, applied to geometrically similar specimens, the size effect law relates the nominal stress σ_N to the tensile strength f_t and to the size D of the specimen:

$$\sigma_N = \frac{Bf_t}{\sqrt{1+D/D_0}} \quad (85)$$

B and D_0 are two constants which need to be fitted from experiments. One needs at least experiments on three different, geometrically similar, sizes for their determination from experiments, as we will see next. The above size effect law has been derived from asymptotic matching between strength of material and LEFM. It is not general, and it can be viewed as a particular case of the universal size effect law [23]. This expression fits in the case of notched specimens. It is important to note that the size effect law applies to both isotropic and orthotropic materials, with the condition that the path of crack propagation remains aligned with one of the principal directions of orthotropy. Li et al. [24] employed an equivalent expression to analyze the size effect test results of notched prismatic shale specimens. It is a widely adopted practice to utilize Equation (84) when the notch length is assumed to be zero. The constancy of the ratio between the length of the notch and the diameter of the specimen results in a mere alteration of the numerical value of constant B in the fitting process. The calculation of the coefficients in Equation (85) is derived based on a suggestion made by Rilem [25]. Equation (85) is reformulated as:

$$Y = A.X + C \quad (86)$$

$$\text{Where } X = D \text{ and } Y = (1/\sigma_N^2)$$

In this form, the size effect law can be fitted using a standard linear regression scheme and:

$$Bf_t = 1/\sqrt{C} ; D_0 = C/A \quad (87)$$

If the tensile strength of the material is known, the regression yields constant B . The fracture energy of the specimen, denoted as G_f , is also recovered as [26]:

$$G_f = \frac{g(\alpha_0)}{EA} \quad (88)$$

$$\text{Where } \alpha_0 = a/D$$

where E is the Young's modulus of the material. The function $g(\alpha_0)$ depends on the geometry of the specimen (including the loading) and on the elastic constants because of anisotropy. It can be regarded as a non-dimensional energy release rate. G_f corresponds to the energy release rate required for crack growth in a structure of infinite size and of any shape. In summary, the size effect law described by Equation (85) and the fracture energy represented by Equation (88) both incorporate three parameters, namely B , $g(\alpha_0)$, and D_0 in addition to the tensile strength and Young's modulus. The variables B and $g(\alpha_0)$ are influenced by the geometry of the system and are also influenced by the elastic characteristics of the material, particularly in the case of orthotropic materials. The parameter D/D_0 quantifies the proximity of failure in a specimen of a given size to either a strength of material criterion (indicated by a small value) or a fracture criterion (shown by a big value). For a given size of specimen, a low value of D_0 suggests that the response of the specimen is in close proximity to Linear Elastic Fracture Mechanics (LEFM). Additionally, the size of the Fracture Process Zone (FPZ) is tiny, indicating that the specimen's response is more prone to brittleness [26]. From a pragmatic perspective, the parameter D_0 can be considered significant as it exhibits a correlation with the dimensions of the fracture process zone. The suitability of using Linear Elastic Fracture Mechanics (LEFM) without significant mistakes is contingent upon the ratio of the thickness of the formation to the propagation of the fracture, denoted as D_0 . When this ratio is substantial, it indicates that the thickness is considerably greater than D_0 , thus enabling the application of LEFM with minimal inaccuracies. Put simply, if the thickness of the formation is significantly more than D_0 , Linear Elastic Fracture Mechanics (LEFM) may be relevant. If the condition is not met, one can still conduct calculations based on Linear Elastic Fracture Mechanics (LEFM), but the resulting fracture energy (or toughness) would exhibit a dependence on size [19]. The procedure and the results obtained for mortar samples manufactured in different years are shown below.

4.5.1.1 Determination of fracture energy in mortar samples from 2021 with size effect

Table 15. Calculations of mortar samples from 2021

Sample	B (mm)	D (mm)	R:D/2	Ls	Fmax (N)	σ_N (MPa)	$1/\sigma_N$	$Y = (1/\sigma)^2$
1	40	25	12.50	20	598	5.8579	0.1707	0.02914
2		52	25	41.6	1222	5.7551	0.1737	0.03019
3		105	50	88	2113	5.1629	0.1936	0.03751

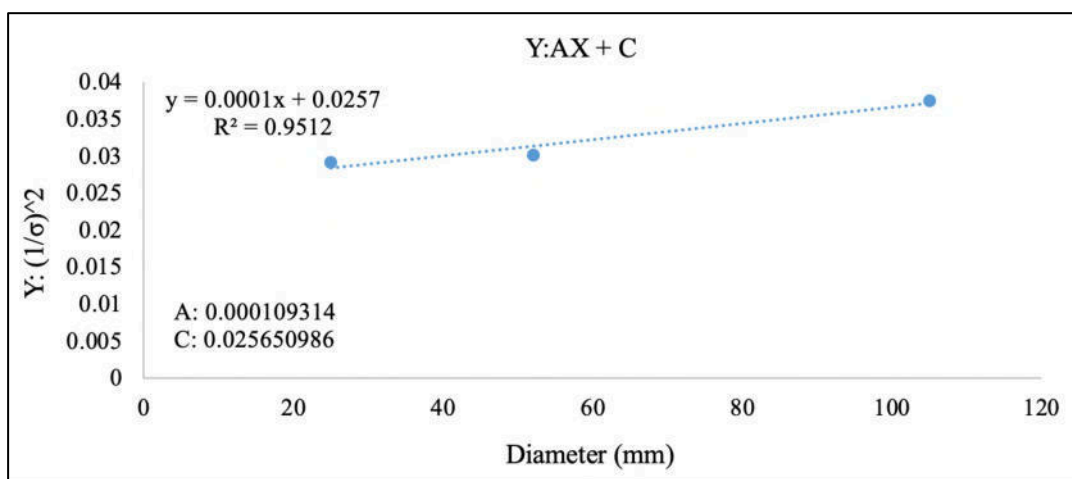


Figure 80. Determination of the slope and intercept of the regression line for mortar samples

Table 16. Calculations of mortar samples from 2021

Sample	D	$D_0 = C/A$	D/D0	Log (D/D0)	(B*ft)	σ_N (MPa)	Log($\sigma_N/B*ft$)
1	25	234.653	0.106539	-0.972487864	6.2437854	5.9355974	-0.021983
2	52		0.221602	-0.654424529		5.6491478	-0.043465
3	105		0.447467	-0.349238574		5.1897157	-0.080304

Table 17. Parameters obtained

Parameters	
$C = 1 / (B*ft) =$	0.025650986
A =	0.000109314
$D_0 = C/A =$	234.6539519
$(B*ft)^2 = 1 / C =$	38.98485645
$(B*ft) =$	6.243785426

Table 18. Obtaining fracture energy

Parameters	
$(B*ft)^2 =$	38.98485 (MPa) ²
E =	1.9E+04 N/mm ²
$D_0 =$	234.65395 mm
g =	0.11
Fracture energy (G_f) =	5.30E-02 (N.mm)/mm ² = 52.96 J/m ²

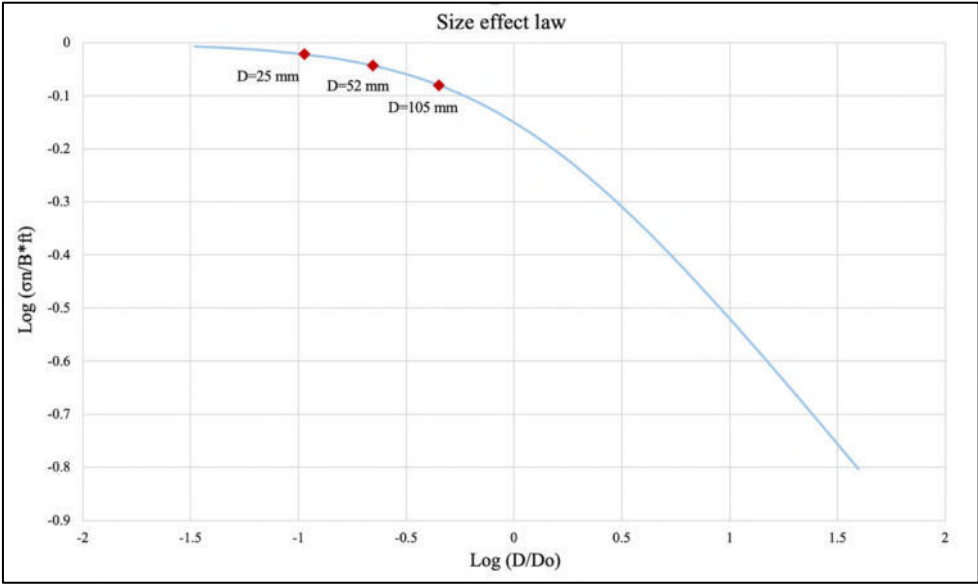


Figure 81. Size effect law for mortar samples from 2021

4.5.1.2 Determination of fracture energy in mortar samples from 2022

Table 19. Calculations of mortar samples from 2022

Sample	B (mm)	D (mm)	R:D/2	Ls	Fmax (N)	σ_N (MPa)	$1/\sigma_N$	$Y = (1/\sigma)^2$
1	40	51	25.5	40.8	1045	5.0180	0.1992	0.03097
2		105	55	84	2115	4.9329	0.2027	0.0410
3		205	105	160	3278	4.0138	0.2491	0.0620

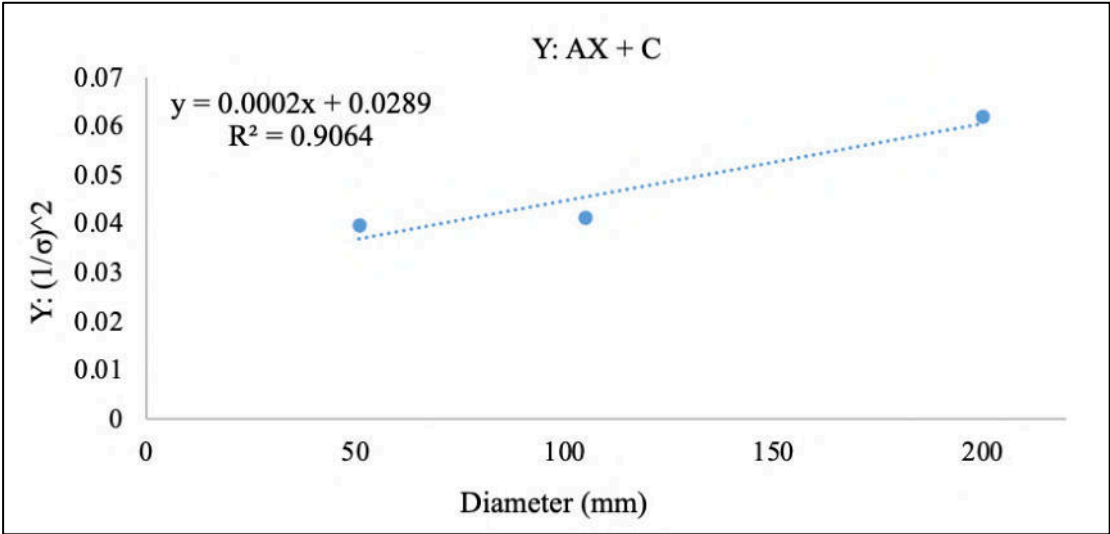


Figure 82. Determination of the slope and intercept of the regression line for mortar samples

Table 20. Calculations of mortar samples from 2022

Sample	D	D ₀ = C/A	D/D ₀	Log (D/D ₀)	(B*ft)	σ _N (MPa)	Log(σ _N /B*ft)
1	51		0.2793	-0.5538		5.2038	-0.0534
2	105	182.56	0.5751	-0.2402	5.8860	4.6898	-0.0986
3	205		1.0955	0.0396		4.0660	-0.1606

Table 21. Parameters obtained

Parameters	
C = 1 / (B*ft) =	0.02886
A =	0.00015
D ₀ = C/A =	182.561
(B*ft) ² = 1 / C =	34.6454
(B*ft) =	5.88603

Table 22. Obtaining fracture energy

Parameters	
(B*ft) ² =	34.6454 (MPa) ²
E =	1.9E+04 N/mm ²
D ₀ =	182.5614 mm
g =	0.11
Fracture energy (G _f) =	3.69E-02 (N.mm)/mm ² = 36.93 J/m ²

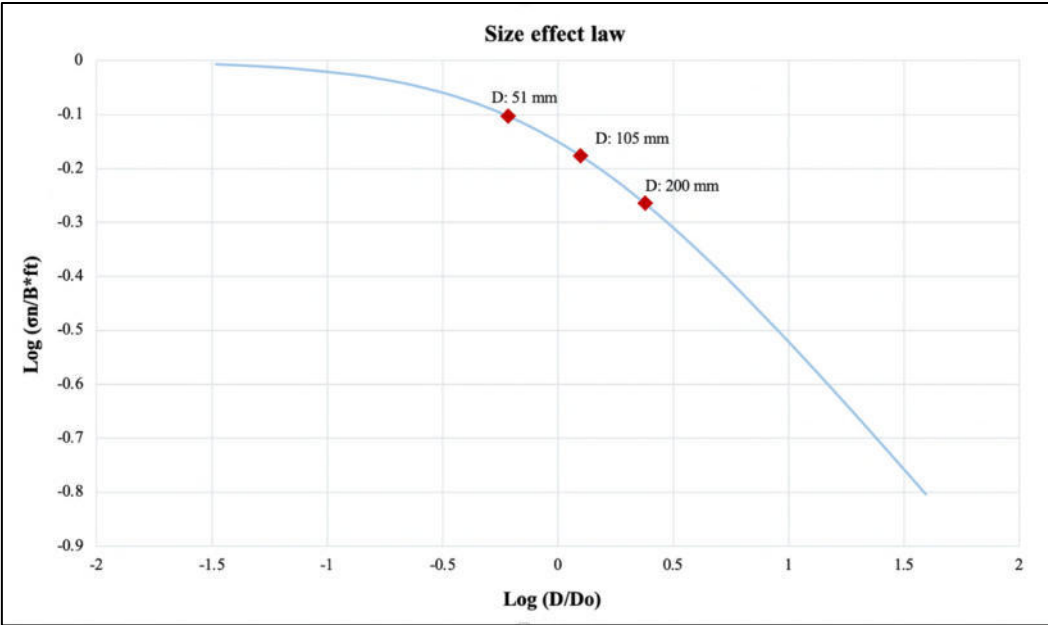


Figure 83. Size effect law for mortar samples from 2022

Then, a calculation was made with 4 mortar specimens to see the evolution of the size effect law, since the previous results show a negative trend for the smallest diameters. Figure 84 shows the size effect for 4 mortar samples with different diameters, it can be observed that as the diameter of the samples increases there is an increase in the size effect, therefore, to have a totally positive trend it is recommended to manufacture larger samples.

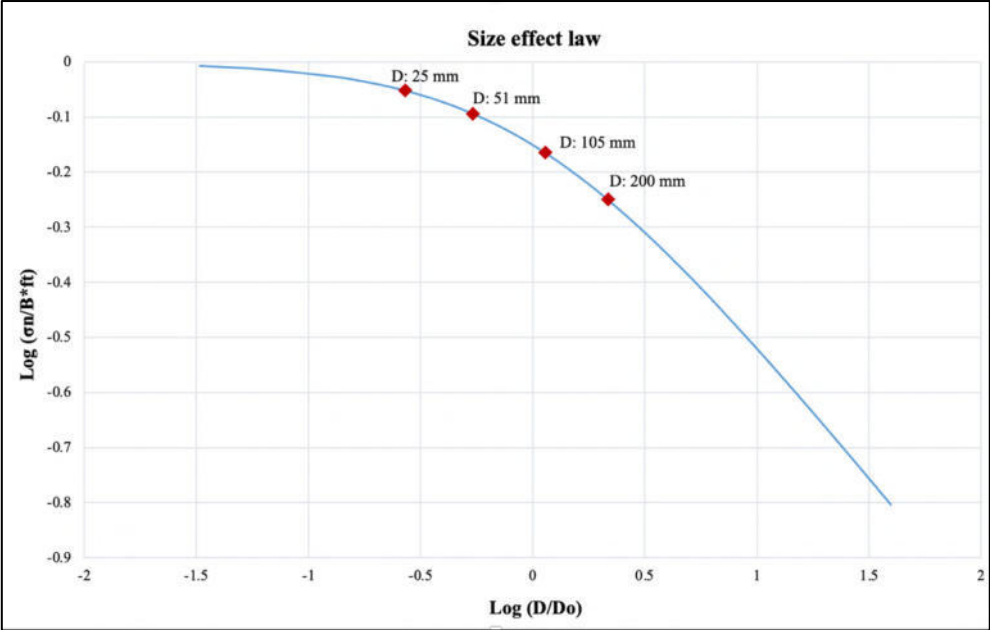


Figure 84. Size effect law for 4 mortar samples

To ascertain the fracture energy through size effect testing, it was imperative to possess an understanding of the non-dimensional energy release rate $g(\alpha_0)$ since it constitutes a crucial element in Equation 88. The mathematical expression representing the behavior of standardized prismatic notched specimens made of isotropic elastic material has been recorded in a previous study [25]. Nevertheless, it is important to note that there is a lack of existing data about the behavior of semi-circular notched specimens when subjected to three-point bending. There are multiple numerical methods that can be employed to ascertain the value of $g(\alpha_0)$. As an illustration, the computation might be executed utilizing J integrals, as exemplified in the investigation carried out by Li et al. [27], particularly for prismatic specimens. We used a unique methodology that is grounded in a continuum damage model and entails performing computations on specimens that possess identical geometric properties. The methodology assumes that the constitutive relation has the capacity to represent the size impact, a fact that has been confirmed through various examples [28-29]. The constitutive relation examined in this research is a continuum representation of the constitutive model utilized by Grassl et al. [29]. The input parameters for this connection consist of the Young's modulus, Poisson's ratio, tensile strength, and fracture energy.

Table 23. Fracture toughness for mortar samples from 2022

Diameter (mm)	Max load (N)	Toughness
50	1118	0.40
	1001	
	1163	
100	2177	0.53
	2226	
	1878	
200	3094	0.54
	2713	
	3148	

Table 24. Fracture toughness for mortar samples from 2021

Diameter (mm)	Max load (N)	Toughness
25	624	0.32
	663	
	606	
50	1551	0.52
	1383	
	1416	
100	2131	0.55
	2179	
	2175	

When comparing the fracture energy results obtained using the size effect method across mortar specimens produced in different years, a discernible variance emerged when compared to values derived from the energy balance method. Specifically, there was a notable difference of 40%. Utilizing the size effect method, we derived fracture energy values of 53 J/m² and 37 J/m² for different specimens. Conversely, the energy balance method yielded an average fracture energy of 90 J/m². It's crucial to consider that these specimens were produced at distinct geographical locations across Mexico. As a result, the cement and fine aggregate used in these specimens originate from various quarries. This geographic variability may introduce certain differences in the material composition, which is an essential factor to consider in our analysis.

In the next phase of our investigation, we intend to calculate fracture energy by employing finite element numerical simulations. This approach promises to provide further insights into our research and enhance our understanding of these complex phenomena.

4.6 Determination of fracture energy with numerical simulation

As mentioned in Chapter III, to calculate the fracture energy, we rely on finite element numerical simulations. Therefore, to corroborate the results obtained previously, the fracture energy was calculated by means of numerical simulation using the parameters obtained in the three-point bending test. Figures 85 and 86 correspond to the specimens carried out in 2021, and Figures 87, 88 and 89 to the specimens carried out in 2022. The graphs show the evolution of the fracture energy during the bending test, therefore, in the graphs we can see the total fracture energy generated until the sample breaks.

4.6.1 Mortar samples from 2021

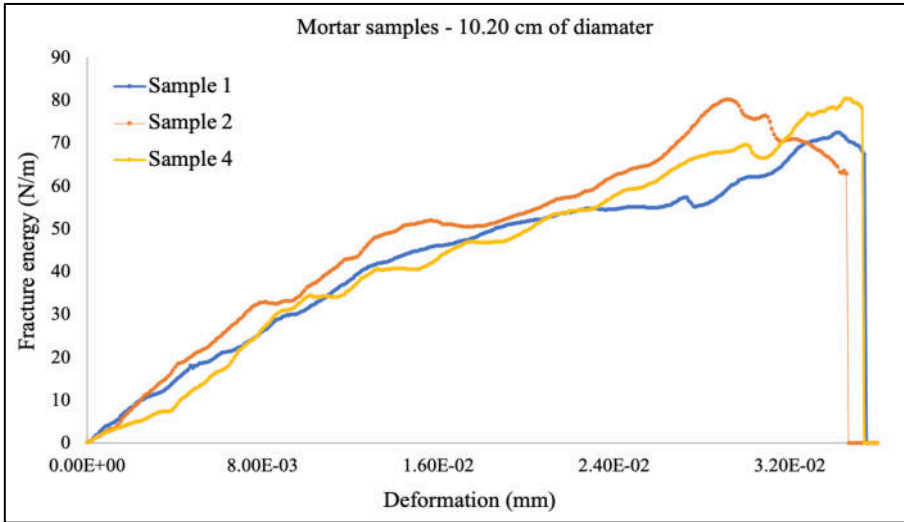


Figure 85. Last fracture energy for sample of 10.20 cm of diameter

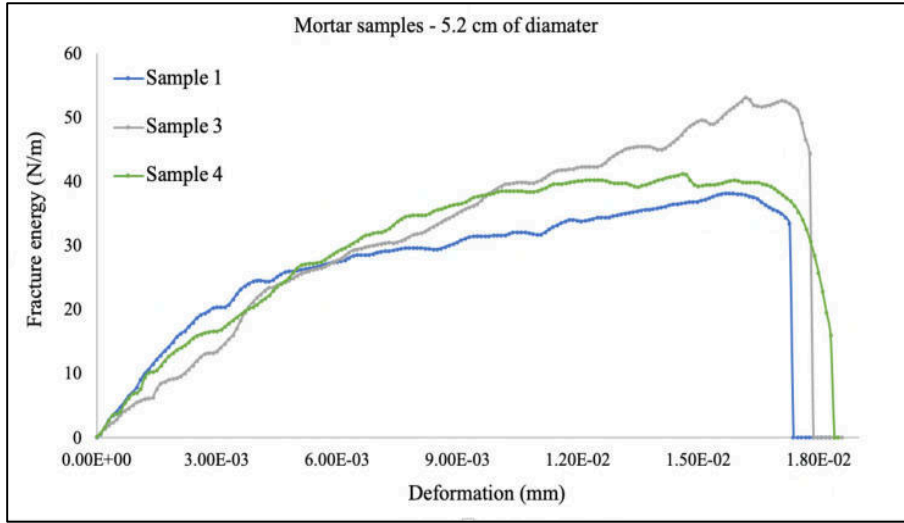


Figure 86. Last fracture energy for sample of 5.2 cm of diameter

4.6.2 Mortar samples from 2022

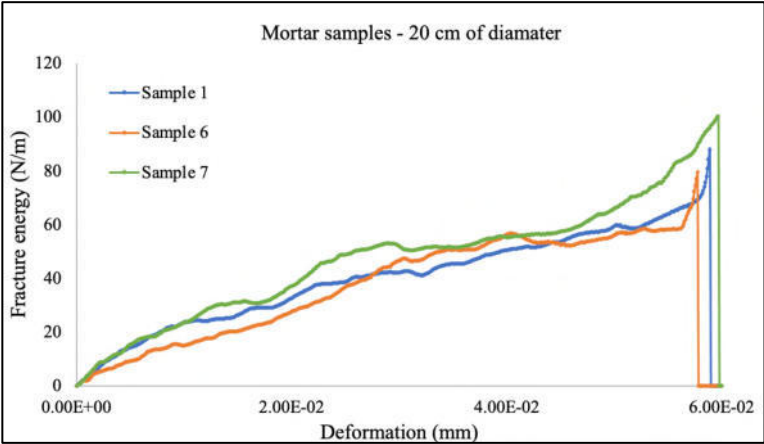


Figure 87. Last fracture energy for sample of 20 cm of diameter

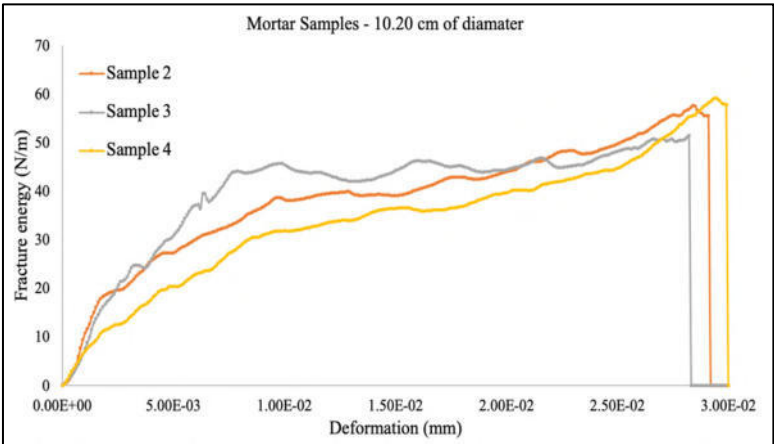


Figure 88. Last fracture energy for sample of 10.20 cm of diameter

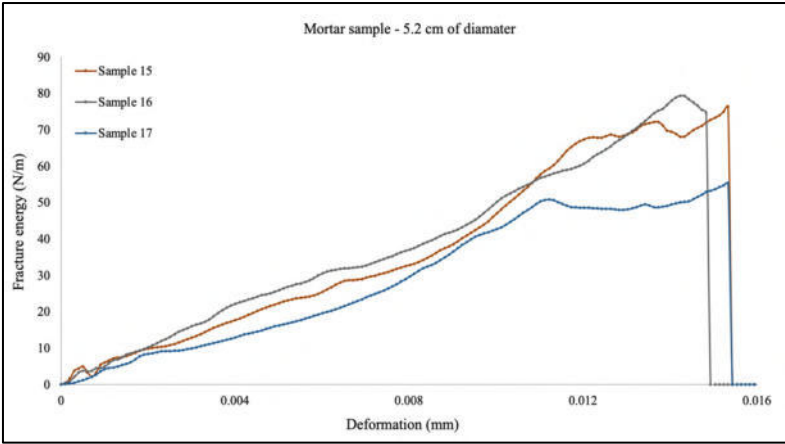


Figure 89. Last fracture energy for sample of 5.20 cm of diameter

To eliminate edge effects associated with crack initiation and total mortar sample failure, crack energy is calculated between an equivalent crack length a_{min} equal to $0.4a$ and a_{max} equal to $0.6a$. The associated relative compliances are used to define the forces a_1 and a_2 associated with these equivalent lengths and based on equation 89, explained in chapter II, we proceed to calculate the fracture energy (see equations 90 and 91).

$$W_f = W_{eA} + W_{AB} - W_{eB} \quad (89)$$

$$W_{AB} = \int_{a_1}^{a_2} F(a) \delta(a) dx \quad (90)$$

$$G_f = \frac{W_{1-2}}{(a_2 - a_1) * e} \quad (91)$$

Table 25 shows a comparison of the averages obtained from the fracture energy values obtained with various methods. With the proposed method, an average fracture energy of 90 J/m^2 was obtained with the bending test method and then by means of a numerical simulation two values were obtained, the final energy during the test and the real fracture energy, in other words, the fracture energy needed to generate or initiate a fracture during the test. To obtain this energy, the integral of the fracture energy graph was considered and then with the area of the trapezoid the real fracture energy is obtained. For example: for mortar specimen number 7 with a diameter of 20 cm, after integrating the fracture energy to 3 mm and calculating the area with the trapezoid, an energy of 61 N/m is obtained. Figure 90 shows an example with sample 7 with a diameter of 20 cm.

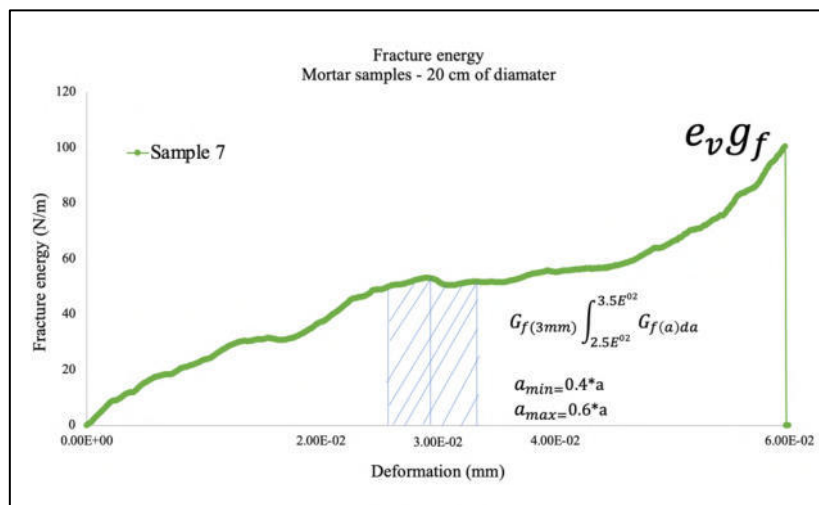


Figure 90. Determination of real fracture energy

Table 25. Fracture energy average values obtained by several methods.

Diameter	Young modulus	Samples 2019		Samples 2021			Samples 2022	
		Conservation of energy	Fracture energy (J/m ²)		Size effect law	Fracture energy (J/m ²)		Size effect law
			Real	Last		Real	Last	
2.5	19	--	--	--	52	--	--	37
5.2		90	38	57		40	69	
10.2		--	46	76		41	63	
20		--	--	--		43	85	

Regarding the fracture energy values acquired through the proposed method and their comparison with values obtained through other methods, a notable twofold increase in energy is observed. This augmentation may be attributed to the dynamic nature of fracture propagation. In other words, the propagation is not constant, demanding a more substantial energy input, especially during the initial stages of hydraulic fracture initiation. It's crucial to consider that during the hydraulic fracture tests, the pressure remained constant. Consequently, this constancy in pressure led to an unstable volume, which, in turn, resulted in an erratic and sudden crack propagation. In essence, a portion of the energy input is converted into kinetic energy during this process. This dynamic aspect of fracture propagation adds complexity to the energy calculations and underscores the importance of considering kinetic energy in our analysis

References

- 1) Thomson, Margaret & Lindqvist, Jan & Elsen, Jan & Groot, Caspar. (2007). Chapter 2.5 Characterisation: Porosity of mortars.
- 2) Maurel O, Rees T, Matallah M, De Ferron A, Chen W, Laborderie C, Pijaudier-Cabot G, Jacques A, Rey-Bethbeder F (2010) Electrohydraulic shock wave generation as a mean to increase intrinsic permeability of mortar. *Cem Concr Res* 40:1631–1638.
- 3) Chen W, Maurel O, Rees T, Sylvestre De Ferron A, La Borderie C, Pijaudier-Cabot G, Rey-Bethbeder F, Jacques A (2012) Experimental study on an alternative oil stimulation technique for tight gas reservoirs based on dynamic shock waves generated by pulsed arc electrohydraulic discharges. *J Pet Eng* 88–89:67–74.
- 4) Mei C, Fang Q, Luo H, Yin J, Fu X (2017) A synthetic material to simulate soft rocks and its applications for model studies of socketed piles. *Adv Mater Sci Eng* 2017, 1565438.
- 5) Gell EM, Walley SM, Braithwaite CH (2019) Review of the Validity of the Use of Artificial Specimens for Characterizing the Mechanical Properties of Rocks. *Rock Mech Rock Eng* 52:2949–296.
- 6) ASTM D-445-06 (2006): Standard Test Method for Kinematic Viscosity of Transparent and Opaque Liquids (and Calculation of Dynamic Viscosity); American Society for Testing Materials: West Conshohocken, PA, 2006.
- 7) P. Halamickova, (1995), "Water permeability in portland cement mortars", *Cement and Concrete Research*, pp 790-802
- 8) Siavash Ghabezloo, (2008), "Effective stree law for the permeability of a limestone, *International Journal of rocks Mechanics*, Vol. 46, pp. 297-306
- 9) Laurence Jouniax, (1995), "Permeability dependence of streaming potential in rocks for various fluid conductivities, *Geophysical Research Letters*, Vol 22, pp. 485-488.
- 10) Choinska M, Khelidj A, Chatzigeorgiou G, Pijaudier-Cabot G (2007), Effects and interactions of temperature and stress-level related damage on permeability of concrete. *Cem Concr Res* 37:79–88.
- 11) Haidar K, Pijaudier-Cabot G, Dub. JF, Loukili A (2005) Correlation between the internal length, the fracture process zone and size effect in model materials. *Mater Struct* 38:201–210.
- 12) Reid RC, Prausnitz JM, Poling BE (1987) *The properties of gases and liquids*. McGraw-Hill, New York, p 136.
- 13) Menou A, Mounajed G, Carre PBH (2006) Residual Fracture Energy of Cement Paste, Mortar and Concrete Subject to High Temperature. *Theoret Appl Fract Mech* 45:64–71.
- 14) Marinescu ID, Pruteanu M (2015) Deformation and fracture of ceramic materials. In: Doi T, Uhlmann E, Marinescu ID (eds) *Handbook of ceramics grinding and polishing*, 2nd edn. Elsevier Pubs, pp 50–66 (Chapter 2)
- 15) Bazant ZP, Prat PC (1988) Effect of temperature and humidity on fracture energy of concrete. *ACI Mater J* 85:262–271.
- 16) Bazant, Z. P., & Pfeiffer, P.A. (1987). Determination of fracture energy from size effect and brittleness number. *ACI Materials Journal*, 84(6), 463-480.
- 17) Muñoz-Ibañez A, Delgado-Martín J, Juncosa-Rivera R. Size Effect, and other effects on mode I fracture toughness using two testing methods. *Int J of Rock Mech and Mining Sci* 2021;143:104785.
- 18) Zhang S, Wang H, Li X, Zhang X, An D, Yu B. Experimental study on development characteristics and size effect of rock fracture process zone. *Eng Fract Mech* 2021;241:107377.
- 19) Pijaudier-Cabot, G., Hajimohammadi, A., Nouailletas, O., La Borderie, C., Padin, A., & Mathieu, J. P. (2022). Determination of the fracture energy of rocks from size effect tests: Application to shales and carbonate rocks. *Engineering Fracture Mechanics*, 271, 108630.
- 20) Bao G, Ho S, Suo Z, Fan B. The role of material orthotropy in fracture specimens of composites. *Int J Solids & Struct* 1992;29:1105–16.
- 21) Zhang S, Wang H, Li X, Zhang X, An D, Yu B. Experimental study on development characteristics and size effect of rock fracture process zone. *Eng Fract Mech* 2021;241:107377.
- 22) Bazant ZP, Planas J. *Fracture and Size Effect in Concrete and other Quasi-Brittle Materials*. CRC Press; 1998.
- 23) Bazant ZP. Scaling of quasi-brittle fracture: asymptotic analysis. *Int J Fract* 1997;83:19–40.

- 24) Li W, Jin Z, Cusatis G. Size effect analysis for the characterization of marcellus shale quasi-brittle fracture properties. *Rock Mech Rock Eng* 2019;52(1):1–18.
- 25) Rilem recommendations. Size effect method for determining fracture energy and process zone size of concrete, *Mater Struct* 1990;23:461-5.
- 26) Bazant ZP, Pfeiffer PA. Determination of fracture energy from size effect and brittleness number. *ACI Mater J* 1987;84:463–80.
- 27) Li W, Jin Z, Cusatis G. Size effect analysis for the characterization of marcellus shale quasi-brittle fracture properties. *Rock Mech Rock Eng* 2019;52(1):1–18.
- 28) Le Bellego C, François Dube J, Pijaudier-Cabot G, Gerard B. Calibration of non local damage model from size effect tests. *Eur J Mech A/Solids* 2003;22(1):33–46
- 29) Grassl P, Gregoire D, Rojas Solano L, Pijaudier-Cabot G. Meso-scale modelling of the size effect on the fracture process zone of concrete. *Int J Solids Struct* 2012;49(13):1818–27

CHAPTER V CONCLUSIONS AND PERSPECTIVES

In this contribution, the hydraulically induced fracture in mortar and rock specimens has been studied experimentally. The experiments are carried out in hollow cylinders subjected to the pressure of the internal fluid until the specimen fractures. The fluid used was oil, to make possible the tests at 100° C.

The experimental set-up allowed the tests to be carried out at room temperature, but also at a temperature of 100 °C. The mechanical and permeability properties of the mortar and limestone were measured before the fracture tests were performed. Fracture energy was estimated based on conservation of energy. The energy supplied by the hydraulic pump turns out to be equal to the energy dissipated during fracture in a specimen.

Dissipation due to fluid viscosity is negligible. Such estimation is obtained directly from the hydraulic fracturing test data without any specific mechanical model. The Estimation of the fracture energy obtained with the laboratory setup presented in this project provides consistent values in mortar specimens at room temperature with the data reported in the literature on similar materials. Also, it was observed that the temperature influences the values of fracture energy obtained, for example, as the temperature increases, both for limestone specimens and for mortar specimens, the fracture energy increases from 20 to 30%.

We have examined a hypothesis positing that all the energy is solely allocated to fracturing both synthetic and natural rocks, without accounting for the energy expended on fluid flow into the porous media of the sample. This supposition appears to be accurate due to the low permeability of the material, restricting the influx of fluids into the porous media of the samples. However, it's important to note that this assumption becomes less applicable when dealing with "hot samples" characterized by significantly higher permeability. It's worth mentioning that "hot samples," thanks to their enhanced permeability, warrant a more comprehensive consideration of energy allocation, encompassing both fracturing and fluid flow aspects. This distinction becomes particularly pertinent when assessing the overall energy distribution within these specific samples, which may exhibit unique behaviors due to their increased permeability characteristics.

In other words, it takes more energy to fracture in hotter zones. Observing the variation of the fracture energy values with respect to temperature (ambient and 100 ° C), we can speculate that in a geothermal reservoir the fractures generated will be directed towards the coldest places, since more energy will be needed to reach the hottest areas. Of course, this speculation does not consider heterogeneities in rock properties or in situ stresses. These could be much more important than the temperature gradient and would allow the propagation of fractures in the hot spots of geothermal reservoirs.

The fracture energy obtained with the proposed method is twice that of a method reported in the literature and with numerical simulation. This may be since the hydraulic fracture generation is dynamic and therefore requires more energy at the beginning of the test. This original contribution in the field of fracture mechanics applied to geothermal reservoirs is based on laboratory tests and has potential application to real reservoirs; The proposed methods yield results validated by strict international scrutiny and configure an additional tool to improve the permeability and, therefore, the extraction efficiency of geothermal energy, which is a green, renewable and still scarcely exploited source in our country and in the rest of the world. world. Due to the foregoing, the authors consider that contributions such as this one, however modest it may seem, will contribute to the mitigation of the already significant effects of climate change caused by human activity.

PERSPECTIVES

Although a method to calculate the energy-balanced fracture energy was obtained by means of an analogue model of a laboratory-scale EGS in synthetic and natural rocks, some issues still need to be addressed. Therefore, based on the results of our research, the following research needs and recommendations are proposed: In relation to the computation of fracture energy, the assessment of this parameter can be conducted with enhanced efficiency or on an alternative scale because the fracture energy measurements or determinations are inherently approximate due to the complex nature of fracture surfaces and their dependence on area, therefore;

- With synthetic rock specimens, for example, cement paste, mortar, and concrete. Secondary or tertiary phases could be incorporated within the matrix and a simulation could be performed to examine the contribution of each phase to the fracture behavior to measure the resulting fracture energy. In other words, the goal would be to predict the overall fracture energy by summing the individual fracture energies of each phase within a sample, rather than relying solely on traditional measurement methods and measuring the energy in a manner.
- Investigate the influence of fracture surface roughness exponent on fracture self-sharpening or dulling behavior. That is; how does the roughness exponent affect the energy or behavior of the fracture? Previous studies by M. Freidman et al. in 1971 discussed the fracture energy of individual minerals present in rocks, such as calcite.
- Validate the prediction made in this research that, during hydraulic fracturing, newly generated fractures tend to propagate into cooler zones. Develop a model that considers temperature changes and the contribution of each phase in the model material to verify this prediction.

These objectives aim to deepen our understanding of fracture energy behavior in model materials, particularly in composite structures, and explore the relationship between fracture surface characteristics, individual phase contributions, and temperature effects.

CONTRIBUTIONS

Participation in conferences:

- 43rd Annual Meeting of the Geothermal Resources Council (GRC) 2019 in the scientific poster session in Palms Spring, California, USA.
- Engineering Mechanics Institute Conference / Probabilistic Mechanics and Reliability 2021 at Columbia University, New York, USA.
- The Biot-Bazant Conference on Engineering Mechanics and Physics of Porous Materials 2021 in Northwestern University, USA.
- Fracture Mechanics of Concrete and Concrete Structures Conference (FraMCos-XI) 2023 in Bangalore, India.

Awards:

- Marcelo Lippmann Scholarship Awards 2019 in the category Best Geothermal Energy Research Project.
- CAMPUS FRANCE Scholarship Awards 2020 in the category engineering project.
- EMI Award 2021 - Second place in the category of Best Scientific Poster, granted by the American Society of Civil Engineers (ASCE) and Columbia University in New York, USA.
- Research Award UANL 2022 in the earth sciences category granted by the Mexican government.

Publications

- Estimation of Fracture Energy from Hydraulic Fracture Tests on Mortar and Rocks at Geothermal Reservoir Temperatures in the Journal Rock Mechanics and Rock Engineering in 2021
- Fracture energy estimation with finite element simulation using an energy balance at geothermal reservoir temperatures (in progress).



Estimation of Fracture Energy from Hydraulic Fracture Tests on Mortar and Rocks at Geothermal Reservoir Temperatures

Omar Rodríguez Villarreal^{1,2,3,4} · Alberto Varela Valdez¹ · Christian La Borderie² · Gilles Pijaudier-Cabot³ · Moisés Hinojosa Rivera¹

Received: 8 October 2020 / Accepted: 29 April 2021

© The Author(s), under exclusive licence to Springer-Verlag GmbH Austria, part of Springer Nature 2021

Abstract

An Enhanced Geothermal System (EGS) can be thought of as an underground heat exchanger designed to extract geothermal energy. The performance of these systems can be improved by increasing permeability with hydraulic fracturing, following the same technique used for hydrocarbon reservoirs. To understand hydraulic fracturing, whether it is implemented in an EGS or in a hydrocarbon reservoir, it is important to know the fracture parameters of the rock at stake, e.g., the fracture energy. We report here the use of a method based on an energy balance during hydraulic fracture tests. Specimens were prepared and they have been mechanically and hydromechanically characterized at 20 °C and 100 °C, a temperature representative of actual reservoir conditions. The fracture energy is obtained from a balance of kinetic, potential and pressure energies involved in the hydraulic fracture tests. The method provides fracture energies that are consistent with the literature data on similar materials. It is also found that the fracture energy increases upon heating.

Keywords Enhanced geothermal systems · Permeability · Hydraulic fracture · Fracture energy · Mortar · Rocks

List of Symbols

G_f	Fracture energy
E	Modulus of elasticity
ϕ	Open porosity
ν	Poisson ratio
σ_t	Tensile strength
κ	Coefficient of permeability
σ_c	Maximum compressive strength
P_{atm}	Atmospheric pressure
E_μ	The Energy dissipated by viscosity

C	Constant
D_o	Diameter outside
D_1	Diameter inside
AE	Acoustic emission

1 Introduction

In the oil and gas industry, hydraulic fracturing has demonstrated its viability in the establishment of fracture networks in deposits with low permeability (see e.g. Yew and Weng 2014), this is also the case in the field of geothermal energy. A geothermal system can be thought of as an underground heat exchanger, and the surfaces where heat is exchanged with the circulating fluid should be as large as possible. This is the purpose of enhancement procedures based on hydraulic fracturing, yielding to an Enhanced Geothermal System (EGS).

Maximizing the surfaces where heat is exchanged means that the hydraulic fracturing process should be controlled as much as possible. Ideally, the induced fractures should be numerous, diffuse and connected to each other. Obviously, such a goal is difficult to achieve as rock properties, in situ stresses, and heterogeneities can neither be controlled nor changed. Nevertheless, a prerequisite for a better control,

✉ Gilles Pijaudier-Cabot
Gilles.Pijaudier-Cabot@univ-pau.fr

¹ Facultad de Ingeniería Mecánica y Eléctrica, Universidad Autónoma de Nuevo León, Pedro de Alba s/n, Ciudad Universitaria, C.P 66451, San Nicolás de los Garza, Nuevo León, Mexico

² Université de Pau et des Pays de l'Adour, E2S UPPA, SIAME, Allée du Parc Montaury, 64600 Anglet, France

³ Université de Pau et des Pays de l'Adour, E2S UPPA, CNRS, Total, LFCR, Allée du Parc Montaury, 64600 Anglet, France

⁴ Centro de Investigación Científica y de Educación Superior de Ensenada (CICESE), Centro Mexicano de Innovación en Energía Geotérmica, Unidad Experimental de Yacimientos Geotérmicos, Rinconada del Pedregal 95, Playitas, C.P. 22860, Ensenada, Baja California, Mexico

e.g., for hydraulic fracturing with multiple stages, is the knowledge of the fracture parameters of the rocks at stake (see the report by Tester et al. 2006). Therefore, the estimation of the fracture energy (G_f), that is, the energy needed to create a fracture of unit surface, and its distribution in the geothermal system need to be measured, or estimated, as accurately as possible.

Geothermal reservoirs are made of different types of rocks such as granite, carbonate and many others for which there exist reported values of fracture energy estimates (Friedman et al. 1972). An accurate determination of the fracture properties of rocks, however, relies on experimental testing methods and consistent interpretation models:

- Extracting and machining fracture specimens according to standard procedures set, e.g., by ASTM (e.g., compact tension specimens) may not be feasible and in most cases only core-based specimens are available. Starting in the mid 80's the International Society for Rock Mechanics suggested several geometries for measuring the fracture toughness on core-based specimens (Ouchterlony 1988; Kuruppu et al. 2013). Configurations include cylinder geometries and half-cylinder geometries subjected to bending, as well as disc geometries subjected to uniaxial compression.
- Data interpretation is often based on linear elastic fracture mechanics (LEFM). However, in quasi-brittle materials such as rocks, concrete or mortars, the fracture resistance is increased by a hardening mechanism that originates at the tip of the crack, inside a region with non-linear behavior and distributed micro-cracking, the fracture process zone. The size of the fracture process zone does not depend on the size of the tested specimen and a size effect is observed (For a complete description, see e.g. Bazant and Planas 1998), meaning that obtained the fracture energy and the apparent strength are size dependent. A size independent value of the fracture energy of the material can be derived from size effect tests (Bazant and Kazemi 1990). For concrete, RILEM (1990) developed such a standard procedure based of three point notched bending beams. For rocks, size effects are never considered in standards. It follows that the apparent fracture toughness that is usually obtained using LEFM is specimen-size dependent and overestimates the real material property generally (Wei et al. 2017).

The purpose of this paper is to present an experimental method that provides the estimation of the fracture energy directly from hydraulic fracture tests. Being based on energy conservation and on the area of the fracture created, it can be regarded as a method that provides easily the fracture properties of the tested material in the laboratory, without a

mechanical model. Size effect is not accounted for here. Size effect mechanical tests on rocks have been performed (see e.g. Li et al. 2019 or Pijaudier-Cabot et al. 2021). A size independent fracture energy could be obtained following our experimental methodology, at the price of experimental studies on specimens of various sizes.

The present technique may, in principle, also be implemented on site provided several conditions would be fulfilled: (1) the location of pre-existing fractures and the overall geometry of the reservoir should be known; (2) the site should be instrumented to determine the geometry of the hydraulically induced crack systems, e.g., with the localization of micro-seismic events (similar to the analyses of acoustic emissions in laboratory tests); (3) upon crack propagation, micro-seismic analyses should provide a sufficiently accurate estimate of the generated crack surfaces. Would these conditions be met, the present method could provide estimates of the fracture energy of the horizon where the cracks propagate. In addition, site experiments might be considered as a possibility of avoiding the bias due to size effect, i.e., by measuring the fracture energy for the “real” geometry of the rock mass at stake.

The method discussed in this paper is developed at the laboratory scale. In the laboratory it is common to use synthetic rocks such as mortar and concrete to develop new experimental techniques [see e.g. Maurel et al. (2010) or Chen et al. (2012)]. Mei et al. (2017) has reported the successful use of synthetic rocks made of a mixture of cement, gypsum, sand, and water, and the validity of this approach has been recently reviewed (Gell et al. 2019). We are going to follow the same idea here and consider first mortar specimens, then, fracture of limestone will be investigated. The experimental set-up allows the measurements of fracture energies at various temperatures. Fracture energies at 20 °C and 100 °C are reported, as these conditions are more representative of actual geothermal reservoir conditions.

This paper is organized as follows: the experimental set-up for hydraulic fracturing is presented in Sect. 2, along with material characterization according to standard procedures. We derive in Sect. 3 the fracture energy from conservation of energy considerations and discuss the results obtained on the mortar samples at room temperature. Section 4 presents the results obtained on limestone at two different temperatures: 20 °C and 100 °C.

2 Hydraulic Fracture Test Set-Up and Material Characterization

Hydraulic fracture tests are performed on hollow cylindrical specimens. Fluid is injected in the hollow cylinder under fixed fluid flow conditions and the pressure is increased until a maximum corresponding to the onset of fracture is reached. In the literature, several set-ups for performing

hydraulic fracture tests can be found, mostly on prismatic specimens [see e.g. Goncalves de Silva and Einstein (2018), Zhou et al. (2008)], but also on cylindrical specimens (see e.g. Wanniarachchi et al. 2018). While tests on prismatic cylinders allow to apply lateral confinement stresses that are not equal, which is more representative of actual reservoir conditions, tests on cylinders are simpler to operate and may use a standard triaxial testing cell if the effect of triaxial states of stresses prior to fracture needs to be investigated. It is this type of geometry, placed in a uniaxial testing device that has been implemented in the present contribution. A schematic view of the testing device is shown in Fig. 1.

Prior to describing these experiments, let us detail the specimen geometry and material characterization.

2.1 Preparation and Characterization of Specimens

Cylindrical specimens with outer and inner diameter of 53 mm and 10 mm respectively, and height of 105 mm were fabricated. Mortar was prepared using CPC 30 R cement and fine aggregate with a maximum particle size of 1.40 mm and with a proportion of 1:2 and W/C ratio of 0.45, the specimens were cured during 28 days.

The mortar specimens were dried following ASTM C-642 standard (2013). The specimens were dried in a Vulcan 3-550 oven. They were heated at a rate of 1°C per minute from room temperature up to 100°C and maintained for four hours. Their dry mass (M_a), weight immersed in boiling water (M_w) and weight immersed in water (M_1) at room temperature were measured, then, the connected porosity of the material, denoted as ϕ , was evaluated following Eq. (1):

$$\phi = \frac{M_w - M_a}{M_w - M_1} \times 100. \quad (1)$$

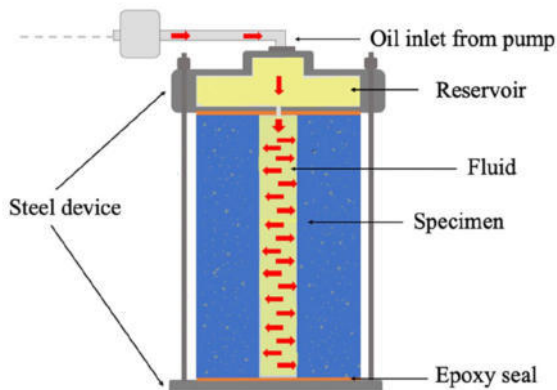


Fig. 1 Testing set-up and cross-section of a typical specimen

On average, the connected porosity was 14.07% for the mortar specimens. To measure their elastic properties and their compressive strength, the specimens were tested in uniaxial compression using a GCTS RTR 2000 triaxial machine. Subsequently, Brazilian tests were performed to obtain the tensile strength of mortar. Table 1 summarizes the results obtained on average for five samples for each test:

The permeability was measured by injecting Mobil DTE 25 oil under pressure in the hollow cylinder with the help of a pump (Quizix model Q-5020-HC), as illustrated in Fig. 1. With the purpose of eliminating any humidity inside the specimens, they were dried following the same procedure as for the mechanical tests before starting the permeability tests. To avoid further contact with humidity, the specimens were placed in hermetic bags filled with Mobil DTE 25 oil. Then, the specimens were placed in the mechanical set-up (Fig. 2), a slight axial load of 525 N was applied to prevent leakage. Next, the fluid was injected at pressure levels of 600, 800, 1000, 1400 and 2000 kPa.

The flow rate was measured upon reaching a steady state. The fluid flow rate was estimated by the PumpWorks software using the inner area of its cylinders and the speed of the pistons.

For the calculation of the intrinsic permeability of mortar K , we assumed a radial flow in the hollow cylindrical specimen, from the inner surface of the specimen to its outer surface and used Darcy's law. Hence, the permeability reads:

$$K = \frac{Q\mu \ln\left(\frac{b}{a}\right)}{2\pi H(p_i - p_e)}, \quad (2)$$

where Q is the measured flow rate (m^3/s), μ is the dynamic viscosity ($\text{kN}\cdot\text{s}/\text{m}^2$), b the outer radius of the specimen, a the inner radius, h the height of the specimen, p_i the inner pressure (kN/m^2) and p_e is the outer pressure (kN/m^2), i.e., the atmospheric pressure.

The values of the dynamic viscosity of the fluid depends on temperature, as provided by the manufacturer. It is equal to $0.03872 \text{ kN}\cdot\text{s}/\text{m}^2$ at room temperature and to $0.00587 \text{ kN}\cdot\text{s}/\text{m}^2$ at 100°C according to ASTM D 445-06 standard. Figure 3 shows a typical plot of the fluid flow rate vs. the injection pressure.

Table 1 Mechanical characterization of mortar

Mechanical characterization	
Maximum compressive strength	$29.78 \pm 0.752 \text{ MPa}$
Young modulus	$13.62 \pm 0.397 \text{ GPa}$
Poisson's ratio	0.15 ± 0.00548
Tensile strength	$2.95 \pm 0.110 \text{ MPa}$

Fig. 2 Injection system for the permeability tests

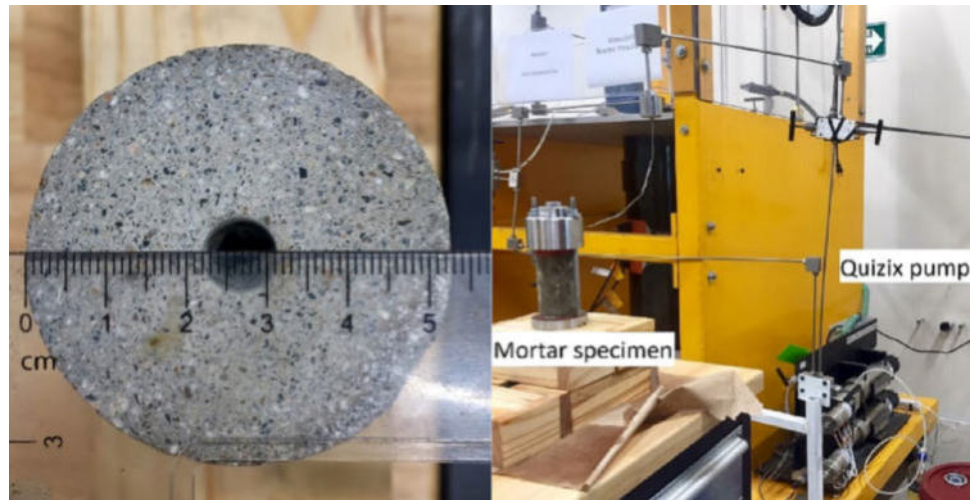


Fig. 3 Evolution of injected fluid flow rate as a function of the injection pressure in mortar specimen 1

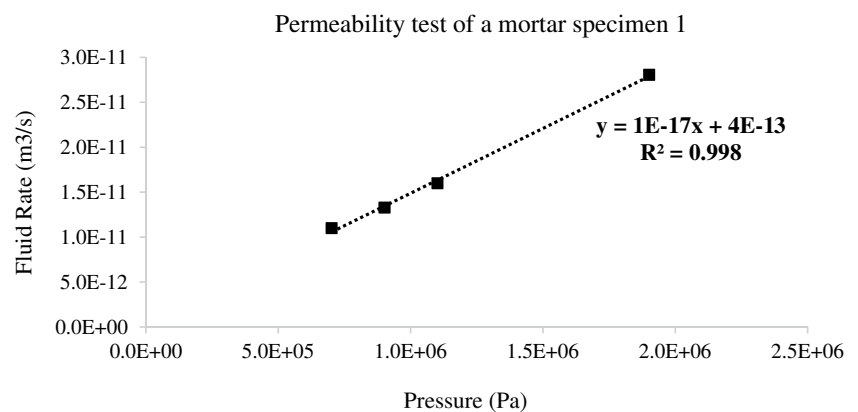


Table 2 Permeability coefficient of the mortar specimens

Mortar specimen	Permeability coefficient (K , m^2)
1	0.98×10^{-18}
2	1.98×10^{-18}
3	5.93×10^{-18}
4	2.13×10^{-18}
Average	2.76×10^{-18}

Table 2 presents the permeability results for the four mortar specimens. The dispersion among the measurements is typical of what could be expected in such tests. For instance, Choinska et al. (2007) observed dispersion of the same order on the permeability of concrete measured with nitrogen using a similar apparatus. For mortar mixtures with a W/C ratio of 0.45 and 28 days of curing, permeability coefficients similar to those reported in this document have also been reported (Halamiczkova et al. 1995).

2.2 Hydraulic Fracture Test

The hydraulic fracture tests were performed on the same specimens used for the permeability test and in the same device. The experiment consisted now in applying a constant flow rate of 0.05 mL/min of Mobile oil DTE 25 to the specimens after the permeability tests. The set-up is illustrated in Fig. 4.

Figure 5 shows the records of the increase of pressure for the mortar specimens tested at ambient temperature. These curves are characterized by a relatively smooth increase of fluid pressure, followed by an abrupt drop down corresponding to the occurrence of fracturing. We may remark in this figure that there is one experiment where the pressure rises sooner compared to the others. Converted into a volume of injected fluid, the time difference (1000 s) corresponds to 0.8 ml which is very small. It may be due to a variation of the initial state of saturation in the specimen. This specimen might be better saturated prior to running the fracture experiment compared to the others. As we will see next, this discrepancy does not affect that much the interpretation of the test data which relies on the calculation of the integrals over

Fig. 4 Hydraulic fracture test system

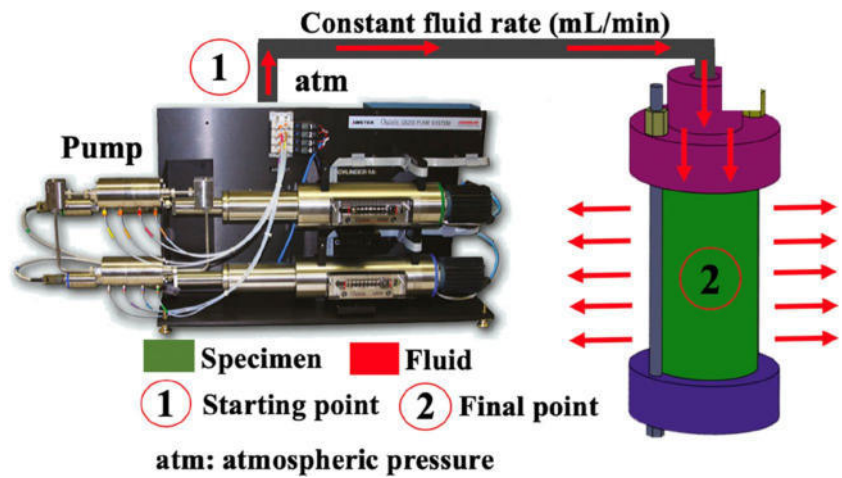


Fig. 5 Comparison of the inner pressure evolution of each mortar specimen tested at ambient temperature

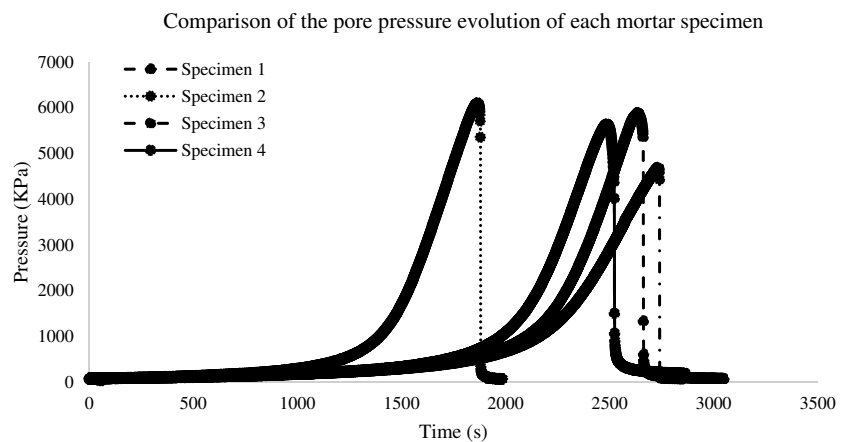


Table 3 Estimated fracture energy for the mortar specimens at room temperature

Mortar specimen	Fracture energy (J/m ²)
1	97.89
2	88.32
3	94.06
4	91.62
Average	92.97
Standard deviation	4.03

time of these curves. The area under the curve in the initial regime, prior to the rise of pressure is very small compared to the area during the entire fracture process. This difference in the initial regime yields a dispersion on the fracture energy in the range of a few percents only (see Table 3).

Figure 6 shows a specimen after the test has been completed. One can see the cracks that have been generated by the increase of pressure (two cracks that start from the borehole).

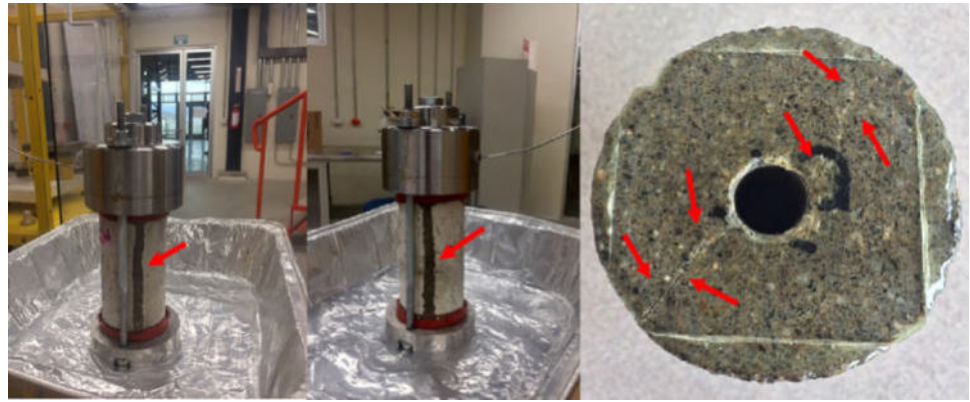
3 Estimation of Fracture Energy

To estimate the fracture energy, we consider the various energies at stake during the tests. We consider that the fluid is incompressible, with constant viscosity and constant density, and we apply Bernoulli's equation. During the hydraulic fracture tests carried out in the lab, the kinetic and potential energy (elevation of the fluid) of the fluid are small compared to the energy related to the pressurization of the fluid and their contributions are discarded (but should be accounted for in field applications). Therefore, the energy that is provided to the specimen originates mainly from the power supplied by from the pump to the fluid denoted as W :

$$W = (p_a A)(Q/A) = p_a \times Q, \tag{3}$$

where W is the power of the pump, p_a is the fluid pressure in the inner hole of the mortar cylinder, Q is the fluid rate and A is the area of the cross section through which the fluid passes. Over a time interval dt the energy provided by the pump is dE defined as:

Fig. 6 Mortar specimen after hydraulic fracture test, the arrows indicate the location of through cracks



$$dE = Wdt. \quad (4)$$

Because the tests were carried out at a constant flow rate, the total amount of energy provided by the pump is:

$$E(t) = \int_0^t Wdt = Q \int_0^t p_a dt, \quad (5)$$

which means that this energy can be easily obtained by integrating the pressure histories in Fig. 5. According to the conservation of energy, the energy supplied by the pump over the entire hydraulic fracture process, at the end of the test corresponding to time t_f , must have been dissipated either due to the viscosity of the fluid E_μ , or due to the fracture of the specimen E_f :

$$E(t_f) = E_\mu + E_f \quad (6)$$

To isolate the energy consumed during the fracture of the specimen, we need now to estimate the dissipated energy due to viscosity, in other words, the dissipation due to Darcy's flow inside the specimen:

$$E_\mu = \int_0^{t_f} P(t) \times Q(t) dt \quad (7)$$

where the pressure and fluid flow are now related by Darcy's law (Eq. 2). Over the specimen, Darcy's law translates into a linear relationship between the pressure and the fluid flow (which is set constant) as illustrated in Fig. 3. Therefore, this integral may be easily evaluated: for a typical fluid flow rate in the range of 0.1 mL/min, the integration over the test duration (2000–3000 s) using the slope obtained in Fig. 3 yields an energy which is in the range of 0.01 J. Upon variations of temperature (e.g., from 20 to 100 °C), the viscosity might change by an order of magnitude but this energy will remain small. Compared to the energy that is expected to be dissipated during fracture, E_μ is negligible. Hence, the

measured fracture energy does not depend on the properties of the pressuring fluid in the present case. It would not be the case if the dissipation of energy due to fluid flow in the various apparatuses or in the specimen due to Darcy flow is not negligible, or if the fluid would react with the rock. A correction of the energy balance would be needed to arrive to an intrinsic estimate of the fracture energy.

In the present experiments, Eq. (6) provides the energy dissipated due to fracture as a function of the energy supplied by the pump. To obtain the fracture energy, we have now to divide E_f by the area of fracture created during the test, A_f which will be obtained experimentally. Therefore:

$$G_f = \frac{Q \int_0^t p_a dt}{A_f}. \quad (8)$$

The fractured area created at the end of the hydraulic fracture test can be approximated as:

$$A_f = n(D_o - D_i)h, \quad (9)$$

where D_o and D_i are the outer and inner diameters of the specimen, respectively, h is the height of the specimen and n is the number of pieces the specimen is fractured into. All the specimens tested in this study were fractured in two parts and four fracture surfaces are generated (see e.g. Fig. 6), hence $n = 4$.

The estimate of the fracture energy, Eq. (8), has been used for the mortar specimens tested. The integrals of the pressure histories in Fig. 5 have been calculated according to the trapezoidal rule and the results are provided in Table 3. On average, a fracture energy of 92.97 J/m² is obtained and the standard deviation is 4.03 J/m². Such values are very consistent with typical fracture energies measured on mortar samples with similar water to cement ratio. Using mechanical fracture tests (Three-Point Bending on notched specimens) Haidar et al. (2005) reported a fracture energy of 88.5 J/m².

4 Fracture Energy of Limestone at Two Different Temperatures

We proceed now to tests on natural rock. Limestone specimens with the same dimensions as those of mortar were prepared from rocks recovered from a geothermal reservoir in Queretaro, México. These specimens were tested at room temperature and also at 100 °C, this temperature being chosen since it is representative of real conditions in geothermal deposits. For the test at 100 °C, the experimental set-up was placed into a Vulcan 3-400 oven regulated at constant temperature. Note that the present experiments could be used to test hard dry rock reservoirs at higher temperatures (e.g., above 200 °C). The limitation of our procedure is the flash point of the oil that is used for fracturing (232 °C in our case). We should stay below this limit for safety reasons, or use another fracturing fluid if high temperatures are aimed at.

Figure 7 shows the configuration used. Before starting the high-temperature tests, the specimens, saturated with oil, were mounted on the steel device inside an oven. The furnace was turned on and the temperature was raised (heating ramp at a rate of 1 °C/mn) until reaching 100 °C. Then, the specimen was left for 20 min more at 100 °C and the tests started. In this way, the fluid contained in the specimen was at the same temperature as the rock. Regarding the fluid used for the measurement of permeability and for fracture, the pipes connected to the specimen and placed in the oven were sufficiently long to allow for heat transfer and to achieve an equilibrium between the fluid entering in the specimen and the fluid contained already in this specimen.

Figure 8 shows the pressure histories for measured for the limestone specimens at both temperatures.

Overall, the curves are similar, except that the fluid flow rate has been changed from ambient temperature (0.05 mL/min) to 100 °C (0.32 mL/min) due to the decreasing viscosity of the oil with increasing temperature (Reid et al., 1987). This decrease of viscosity was accounted for in the calculation of the permeability. A total of eight limestone

samples were used, four at room temperature and four at 100 °C. The average results are summarized in Table 4.

We may observe in this table that the permeability increases with the temperature by 44%. This is consistent with measurements reported in the literature (Choinska et al. 2007).

Also, there is an increase of 20% of the fracture energy. A similar increase can be also reported for mortar samples tested according to the same procedure: from 93.42 J/m² at 20 °C to 129.1 J/m² at 100 °C. This growth of the fracture energy observed on mortar samples is also consistent with existing data (see e.g. Menou et al. 2006).

Several explanations for this increase can be found in the literature: first of all, fracture energy increases as micro-cracking occurs due to the differences in thermal expansion of the various minerals contained in the material (Marinescu and Pruteanu 2015). The principle is that, due to existing micro-cracks, a major fracture may be arrested and therefore needs more energy to propagate. It is also generally accepted that fracture is a thermally activated rate process (Bazant and Prat 1988). At the same time that thermal expansion occurs, the local fracture energy decreases locally, yielding an increase of micro-cracking. Finally, thermal expansion associated with heating from room temperature to 100 °C can reduce the radius of curvature at the tip of micro-cracks, thus reducing the stress intensity factor which will lead to more energy needed to propagate fracture.

5 Conclusions

- In this contribution, hydraulically induced fracture has been studied experimentally on mortar and rock specimens. The experiments are performed on hollow cylinders subjected to inner fluid pressure up to fracture. The fluid used is oil. The set-up allows to perform tests at ambient temperature, but also at temperature of 100 °C at least. The mechanical and permeation properties

Fig. 7 Set-up for high temperature tests in limestone samples. The arrows indicate the location of through cracks after the test at 100 °C



Fig. 8 Pressure histories during the hydraulic fracture test for limestone at room 100 °C (top) and 20 °C (bottom)

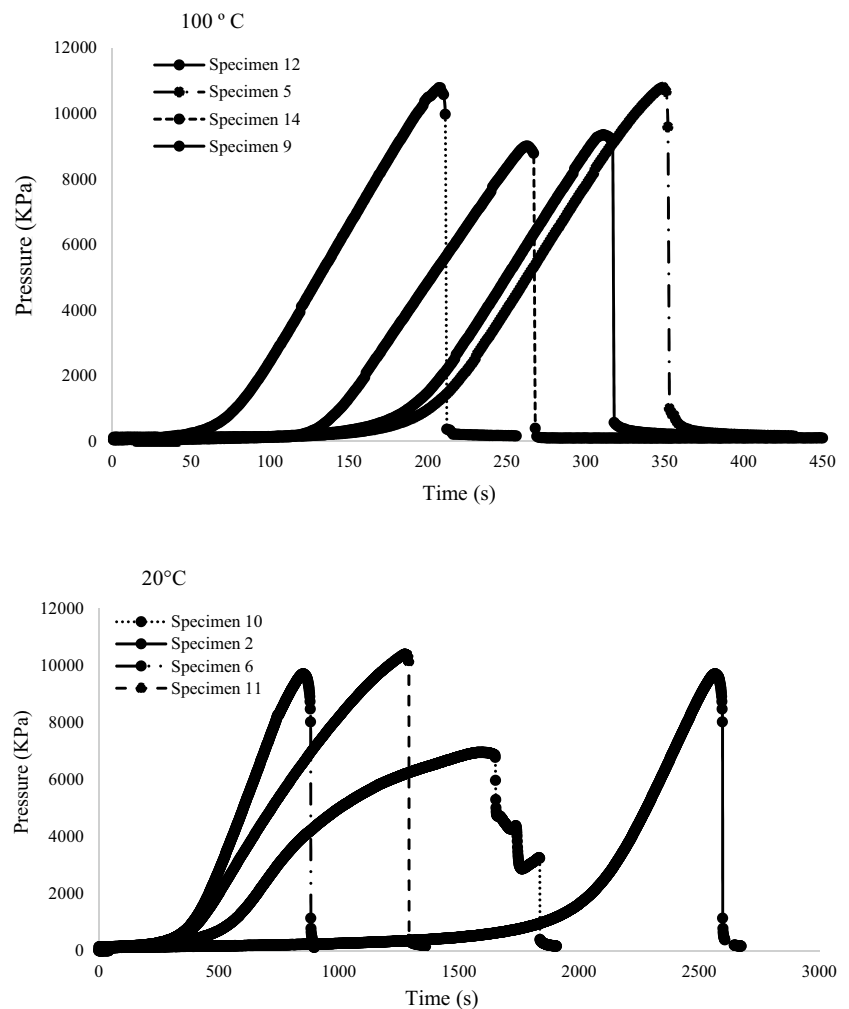


Table 4 Data for limestone at two temperatures

Quantity of samples	Temperature of specimen (°C)	Young Modulus (GPa)	Poisson's ratio (ν)	Permeability (m^2)	Connected porosity	Fracture energy (J/m^2)
4	20	24.98	0.29	4.5×10^{-18}	0.30	213.5
4	100	–	–	6.5×10^{-18}	–	258.7

of mortar and limestone have been measured prior to running the fracture tests.

- The fracture energy is estimated on the basis of conservation of energy. The energy supplied by the hydraulic pump turns out to be equal to the energy dissipated during fracture. In the set-up, dissipation due to fluid viscosity is negligible. Such an estimate, is directly obtained from the hydraulic fracturing test data without any specific mechanical model.
- The fracture energy estimate, applied to the present laboratory set-up, provides fracture energies of mortar at

ambient temperature that are consistent with the literature data on similar materials. Temperature is found to have an influence on the fracture energy as it increases for both limestone and mortar of 20–30%.

By looking at the variation of the fracture energy with temperature, we may speculate that in a geothermal reservoir the fractures generated will be directed towards the coldest places. Of course, such a speculation does not account for heterogeneities of rock properties or of in situ stresses. These might be much more important than the gradient of

temperature and would allow for fracture propagation in hot spots of geothermal reservoirs.

Acknowledgements Partial financial supports from the hub “New-pores” under the Investissement d’Avenir French programme (ANR-16-IDEX-0002), from CONACYT (Mexican National Council of Science and Technology), Campus France México and from ANDERA (Association pour le Développement des Energies Renouvelables et Alternatives) are acknowledged. A very special thanks to the staff of CeMIE-Geo for their help, especially to Dr. José Manuel Romo Jones, Lic. Claudia Cardenas, Lic. Belinda Sandoval, M.C. Margarita Martínez, Dr. Rene Guzmán and M.C. Omar Pérez Valdovinos.

Author contributions Conceptualization: AVV, MHR; methodology: ORV, AVV, CLB, GP-C; formal analysis and investigation: ORV, AVV; writing—original draft preparation: ORV; writing—review and editing: AVV, CLB, GP-C, MHR; funding acquisition: AVV, GPC, MHR, supervision: AVV, CLB, GP-C, MHR.

References

- ASTM C 642–13 (2013), Standard test method for density, absorption, and voids in hardened concrete. ASTM International, West Conshohocken, PA, www.astm.org. Accessed Nov 2018
- Bazant ZP, Kazemi MT (1990) Determination of fracture energy, process zone length and brittleness number from size effect, with application to rock and concrete. *Int J Fract* 44:111–131
- Bazant ZP, Planas J (1998) Fracture and size effect in concrete and other quasi-brittle materials. CRC Press, p 640
- Bazant ZP, Prat PC (1988) Effect of temperature and humidity on fracture energy of concrete. *ACI Mater J* 85:262–271
- Chen W, Maurel O, Reess T, Sylvestre De Ferron A, La Borderie C, Pijaudier-Cabot G, Rey-Bethbeder F, Jacques A (2012) Experimental study on an alternative oil stimulation technique for tight gas reservoirs based on dynamic shock waves generated by pulsed arc electrohydraulic discharges. *J Pet Eng* 88–89:67–74
- Choinska M, Khelidj A, Chatzigeorgiou G, Pijaudier-Cabot G (2007) Effects and interactions of temperature and stress-level related damage on permeability of concrete. *Cem Concr Res* 37:79–88
- Friedman M, Handin J, Alani G (1972) Fracture-surface energy of rocks. *Int j Rock Mech Min Sci* 9:757–766
- Gell EM, Walley SM, Braithwaite CH (2019) Review of the Validity of the Use of Artificial Specimens for Characterizing the Mechanical Properties of Rocks. *Rock Mech Rock Eng* 52:2949–2961
- Goncalves da Silva B, Einstein H (2018) Physical processes involved in the laboratory hydraulic fracturing of granite: visual observations and interpretations. *Engng Fract Mech* 191:125–142
- Haidar K, Pijaudier-Cabot G, Dubé JF, Loukili A (2005) Correlation between the internal length, the fracture process zone and size effect in model materials. *Mater Struct* 38:201–210
- Halamickova P, Detwiler RJ, Bentz DP, Garboczi EJ (1995) Water permeability and chloride ion diffusion in Portland cement mortars: relationship to sand content and critical pore diameter. *Cem Concr Res* 25(4):790–802
- Kuruppu MD, Obara Y, Ayatollahi MR, Chong KP, Funatsu T (2013) The IRSM suggested methods for rock characterization, testing and monitoring. Springer, pp 107–114
- Li W, Jin Z, Cusatis G (2019) size effect analysis for the characterization of Marcellus shale Quasi-brittle fracture properties. *Rock Mech Rock Eng* 52:1–18
- Marinescu ID, Pruteanu M (2015) Deformation and fracture of ceramic materials. In: Doi T, Uhlmann E, Marinescu ID (eds) *Handbook of ceramics grinding and polishing*, 2nd edn. Elsevier Pubs, pp 50–66 (**Chapter 2**)
- Maurel O, Rees T, Matallah M, De Ferron A, Chen W, Laborderie C, Pijaudier-Cabot G, Jacques A, Rey-Bethbeder F (2010) Electrohydraulic shock wave generation as a mean to increase intrinsic permeability of mortar. *Cem Concr Res* 40:1631–1638
- Mei C, Fang Q, Luo H, Yin J, Fu X (2017) A synthetic material to simulate soft rocks and its applications for model studies of socketed piles. *Adv Mater Sci Eng* 2017, 1565438
- Menou A, Mounajed G, Carre PBH (2006) Residual Fracture Energy of Cement Paste, Mortar and Concrete Subject to High Temperature. *Theoret Appl Fract Mech* 45:64–71
- Ouchterlony F (1988) Suggested methods for determining the fracture toughness of rock. *ISRM Commission on Testing Methods. Int. j. Rock Mech Min Sci Geomech Abstr* 25:71–96 (**co-ordinator**)
- Pijaudier-Cabot G, Halimohammadi A, Nouailletas O, La Borderie C, Padin Peben A, Mathieu JP (2021) Experimental determination of the fracture energy of rocks from size effect tests on semi-circular notched specimens, submitted to *Rock Mechanics and Rock Engineering*
- Reid RC, Prausnitz JM, Poling BE (1987) *The properties of gases and liquids*. McGraw-Hill, New York, p 136
- Rilem (1990) Size effect method for determining fracture energy and process zone size of concrete. *Mater and Struct* 23:461–465
- Tester JW, Anderson B, Batchelor A, Blackwell D, DiPippo R, Drake E, Garnish J, Livesay B, Moore MC, Nichols K (2006) *The future of geothermal energy: Impact of enhanced geothermal systems (EGS) on the United States in the 21st century*. Massachusetts Institute of Technology
- Wanniarachchi WAM, Ranjith PG, Perera MSA, Rathnaweera TD, Zhang DC, Zhang C (2018) Investigation of effects of fracturing fluid on hydraulic fracturing and fracture permeability of reservoir rocks: an experimental study using water and foam fracturing. *Eng Fract Mech* 194:117–135
- Wei MD, Dai F, Xu NW, Zhao T, Liu Y (2017) An experimental and theoretical assessment of semi-circular bend specimens with chevron and straight-through notches for mode I fracture toughness testing of rocks. *Int j Rock Mech Min Sci* 99:28–38
- Yew CH, Weng X (2014) *Mechanics of hydraulic fracturing*. Gulf Professional Publishing, pp 1–2
- Zhou J, Chen M, Jin Y, Zhang G (2008) Analysis of fracture propagation behavior and fracture geometry using tri-axial fracturing system in naturally fractured reservoirs. *Int j Rock Mech Min Sci* 45:1143–1152

Publisher’s Note Springer Nature remains neutral with regard to jurisdictional claims in published maps and institutional affiliations.

École doctorale des Sciences Exactes et Leurs (ED 211)

LABORATOIRE DES FLUIDES COMPLEXES ET LEURS
RESERVOIRS (LFRC)

CONTACT

omar_rdzv@hotmail.com
omar.rodriguez-villarreal@univ-pau.fr